MAGNETIC DRUG TARGETING: DEVELOPMENT OF A NOVEL DRUG DELIVERY SYSTEM FOR PROSTATE CANCER THERAPY

by

MAHAM RAHIMI

Presented to the Faculty of the Graduate School of

The University of Texas at Arlington in Partial Fulfillment

of the Requirements

for the Degree of

DOCTOR OF PHILOSOPHY

THE UNIVERSITY OF TEXAS AT ARLINGTON

August 2008

ACKNOWLEDGEMENTS

I would like to sincerely thank various people who provided me with support and guidance. I would like to deeply thank my parents Mr. Mahmoud and Mrs. Faryal Rahimi for their continual support and encouragement. I also would like to thank my wife Nazanin Majdzadeh for her love, support, and understanding. I greatly appreciate my advisor, Professor Kytai T. Nguyen, for giving me this opportunity and for her endless guidance, which made it possible to accomplish this work. I gratefully acknowledge all of my thesis committee members (Dr. Robert Eberhart, Dr. Cheng-Jen Chuong, Dr. Jian Yang, Dr. Efstathios I. Meletis, and Dr. Yaowu Hao) who have given their time to read this manuscript and to offer valuable advice on my research project at the University of Texas at Arlington. Last but not the least; I would like to acknowledge the contribution of my coworkers and other students at the University of Texas at Arlington to the completion of this dissertation.

May 1, 2008

ABSTRACT

MAGNETIC DRUG TARGETING: DEVELOPMENT OF A NOVEL DRUG DELIVERY SYSTEM FOR PROSTATE CANCER THERAPY

Maham Rahimi, PhD.

The University of Texas at Arlington, 2008

Supervising Professor: Dr. Kytai T. Nguyen

Magnetic nanoparticles (MNPs) have been attracting a great amount of attention because of their numerous applications including contrast agents in magnetic resonance imaging (MRI), magnetic targeted drug carriers, and hyperthermia treatments for cancer. However, complications, including aggregation of MNPs, have limited their use in drug delivery applications. To overcome these limitations, several methods have been developed to coat magnetic particles. One method includes coating them with polymers to produce polymer/MNPs for increasing the MNP dispersion and stability. This method also increases the efficiency of loading and releasing drugs to specific locations for the treatment of various diseases including prostate cancer.

The major objective of this research project was to develop polymer magnetic nanoparticles (PMNPs) using a silane coupling agent and a novel thermo-sensitive polymer, N-isopropylacrylamide-acrylamide-allylamine (NIPA-AAm-AH). The temperature-sensitive polymers were chosen as a shell for the purpose of creating a controlled drug delivery system. In this system, the temperature induced by the magnetic core would be used to release therapeutic agents from the polymer shell at a specific location. The chemical and physical properties of these PMNPs were determined using Fourier transformed infrared spectroscopy, nuclear magnetic resonance, x-ray photoelectron spectroscopy, and a superconducting quantum interference device. Transmission electron microscopy indicated the size of our PMNPs were about 100 nm. These nanoparticles had a better biocompatibility in comparison to the original MNPs using cytotoxicity assays (e.g. MTS assays). Moreover, bovine serum albumin (BSA) and doxorubicin release profiles from the nanoparticles indicated that our PMNPs released drugs in response to changes in temperature. Finally, results from iron assays and parallel flow chamber systems, with external magnets used to assess the cellular uptake and *in vitro* localization of the synthesized nanoparticles, indicated that these nanoparticles would provide a means for magnet targeting capabilities.

TABLE OF CONTENTS

LIST OF ILLUSTRATIONS

LIST OF TABLES

Table Page

CHAPTER 1

INTRODUCTION

Recently, the investigation, manufacturing, and application of nanoparticles have increased rapidly. Nanoparticles are defined as submicron colloidal systems, in general (< 1 μm). The advanced technology in nanoparticles requires scientists to study colloidal science from many angles such as the investigation of chemical and physical properties of nanoparticles. In addition, new areas in science like nanotechnology and nanomedicine have emerged. Based on the NIH (National Institutes of Health) definition, nanomedicine, the subsidiary of nanotechnology, involves a highly specific medical intervention that creates and/or uses materials and devices at the levels of molecules and atoms to treat diseases or repair damaged tissues. In this chapter, we will give an overview, synthesis, and applications of nanoparticles. The emphasis will be on magnetic nanoparticles (MNPs) and polymer coated MNPs, which are commonly used in the area of biotechnology, especially in nanomedicine.

1.1 Magnetic nanoparticles

In addition to their use as contrast agents, there has been increased interest in recent years in developing MNPs as carriers for delivering therapeutic agents to specific locations in the body. MNPs such as iron oxide nanoparticles were first introduced as

MRI contrast agents in the mid-1980s. These nanoparticles are approved by the FDA for clinical use and utilized widely in the 21st century for imaging applications.[1] For drug delivery purposes, the concentration of MNPs used is higher when compared to the dose used in imaging. The reason for this is that larger numbers of nanoparticles are required for delivering a sufficient amount of therapeutic agents for an effective treatment. Consequently, complications such as cytotoxicity and aggregation of MNPs have limited their use in this area. Despite these limitations, MNPs have promising uniqueness compared to other nanoparticles. For example, MNPs as a drug delivery system can be localized in a specific region in the body using an external magnetic field. The particle and drug profiles can also be quantified and imaged non-invasively. Thus, several approaches have been developed to synthesize MNPs from various materials and to make these nanoparticles more biocompatible.

1.1.1 Materials

There are many types of materials used to synthesize MNPs. However, only nanoparticles made of iron oxide (magnetite Fe_3O_4 or magnemite Fe_2O_3) have been applied extensively in biotechnology applications, especially in nanomedicine.[2-5] These iron oxide nanoparticles have low cytotoxicity.[6, 7] They can be broken down into oxygen and iron, which are eventually used as key elements for metabolism and oxygen transport inside the human body.[6] Another advantage of these nanoparticles is their superparamagnetic behavior when they are approximately 10 nm in diameter.[7] The superparamagnetic property of these nanoparticles is defined as a magnetization that is

generated when a magnetic field is applied and disappears when the magnetic field is removed. This characteristic will lead to an easier dispersion of these nanoparticles and a less likelihood of them clumping when there is no magnetic field around. However, a major limitation of these nanoparticles is that they have low magnetic magnitude (less than 80 emu/g).[8] This factor makes them difficult to control remotely by an external magnetic field.[1] To overcome this weak magnetic responsiveness, implanting magnets to the target site has been used to maximize the magnetic field at that location. For example, in rabbit studies, polymer coated MNPs loaded with the chemotherapy agent doxorubin have accumulated in an implanted kidney with the Au-plated magnet.[1, 4, 9] The disadvantage of these nanoparticles is that the core (Au-Fe) cannot be broken down and metabolized.

Besides iron oxide, other types of materials such as Fe-Co, Fe-Ni, Fe-Pt, and Co-O have also been investigated. These MNPs contain a larger magnetic moment than iron oxide nanoparticles. This in turn will reduce the amount of used particles while producing the same magnetic effect when compared to that from iron oxide.[1] However, these nanoparticles contain heavy metals other than iron, which theoretically increases their toxicity. These nanoparticles are also ferromagnetic, which means that they will remain permanently magnetized whether or not an external magnetic field is removed. This high magnetic moment might make these nanoparticles more likely to clump (aggregate) and lead to the potential blocking of blood vessels inside the body. In order to take advantage of the high magnetic moment of these nanoparticles and to overcome

the aggregation problem, it is necessary to encapsulate them with suitable materials or coatings. A number of materials such as Au, Ag, peptide capping ligands, silica, carbon, gas-filled microbubbles, and oleic acid have been under investigated, and have shown some promising results.[1, 4, 9] Since our intention is to concentrate on nanomedicine, only the synthesis of iron oxide nanoparticles will be discussed in later sections.

1.1.2 Synthesis of magnetic nanoparticles

Co-precipitation. The major route to synthesize iron oxide nanoparticles is through the co-precipitation of Fe^{2+} or Fe^{3+} aqueous salt solutions by the addition of a base. Compared to other physical or chemical methods, the co-precipitation technique is simpler, more efficient, and easier to control size, composition, and shape of the formed nanoparticles. There are two common co-precipitation methods to produce ferrous oxide nanoparticles. In the first technique, MNPs are synthesized through partial oxidation of ferrous hydroxide.[10] One of the most used oxidizing agents to synthesize MNPs in this method is nitrate ions.[10] However, the disadvantage of this method is that it generates nanoparticles with mean diameters between 30 to 100 nm, exhibiting ferromagnetic behavior. Nanoparticles having superparamagnetic properties are usually in the size range of 10 nm in diameter or less.

Besides oxidation of ferrous hydroxide, monodispersed and small-sized magnetite can be obtained by precipitating magnetite at a low temperature in an oxygen

free environment.[6] The synthesized nanoparticles can later be separated into different sizes using centrifugation at different speeds and times. This method is often used to produce magnetite with a narrow size range (from 2 to 15 nm). In this size range, MNPs behave as superparamagnetics in biological environments.

The third method involves aging stoichiometric mixtures of ferrous and ferric salts in aqueous solutions at different pH levels.[6] The size of MNPs decreases as the pH and ionic strength in the medium increases.[11] Furthermore, the size of MNPs can be adjusted using different concentrations of surfactant: the higher the concentration of surfactant, the smaller the size of the nanoparticles.

Emulsion. Emulsions formed by mixing two immiscible liquids together have been used to produce MNPs. In this system, small droplets of one liquid, called "dispersed phase" (oil phase), are suspended with the other fluid, called "continuous phase" (water phase). For example, Gupta et al. have used water as the continuous phase and hexane as the dispersed phase to synthesized 10 nm MNPs.[5] A major disadvantage of this technique is that the formed particles are not stable after synthesis and aggregate to form larger particles. To stabilize MNPs, various surfactants have been used in the emulsion process. For example, ferrous dodecyl sulfate, $Fe(DS)_2$, has been added to the synthesis process to produce magnetite with average sizes of 4 to 12 nm.[12] Furthermore, Gupta et al. have used docusate sodium salt (AOT) as a surfactant to formulate MNPs from co-precipitating ferrous and ferric salts in the presence of a

base.[6] They found that this synthesis process created MNPs of a very small size (less than 15 nm) and a narrow size distribution.

Polyols. This method was first reported as a method to produce elemental metals and alloys,[13] where a high boiling alcohol was used for its reducing properties.[14] In the polyol process, the liquid polyol functions as the solvent, the reducing agent, and in some cases as a complexing agent for the metallic cations.[15] The solubility of metal in liquid polyol can be either highly or slightly soluble. Monodispersed nanoparticles are formed by controlling the kinetic parameters of the precipitation, i.e. separating the nucleation and growth steps. An example for this approach is the use of diols (e.g. 1,2-decanediol) or polyalcohols (e.g. polyethylene glycol) to synthesize iron oxide nanoparticles.[16]

High temperature decomposition. In this process, iron precursors are decomposed in the presence of hot organic surfactants in order to yield good size control, narrow size distribution, and crystallinity.[15] For instance, MNPs with a size range of 4 to 10 nm in diameter have been synthesized by injecting solution of $FeCup_3$ (Cup: N-nitrosophenylhydroxylamine) in octylamine at 250-300^{0}C.[17] Furthermore, 13-nm MNPs have been formed by adding iron pentacarbonyl ($Fe(CO)_5$) into a solution of surfactants and a mild oxidant (e.g. trimethylamine oxide).[18] Sun et al. have also produced approximately 20 nm MNPs using thermal decomposition by mixing 4 nm of pre-made MNPs with iron (III) acetylacetonate, $Fe(acac)_3$, in phenyl ether in the

presence of 1,2-hexadecanediol, oleic acid, and oleylamine. In general, this method can produce monodispersed MNPs with high control of the particle size.[17, 19]

Utilizing ferritin. In this approach, MNPs are created utilizing inherent host-guest properties of protein (ferritin) cage architectures.[20] The electrostatic nature of the interior surface of the protein cage allows for mineralization of MNPs.[20] Aggregation in the interior of the protein cage is enough to change the redox potential of Fe (II) and acts as a nucleation site by clustering Fe (II/III) cations. This in turn would act as a catalytic site for more oxidative hydrolysis.[21] MNPs are produced by oxidation of ferritin loaded with different amounts of iron (II) ions and trimethylamino-N-oxide.[22] Small molecules of iron are able to pass through the pores on the protein cage for reactions. Consequently, the size of MNPs is determined by the size of the inner volume of the protein cage.[20]

Electrochemical synthesis. Electrochemical synthesis has been used to synthesize maghemite (γ-Fe_2O_3) with average size varying from 3 to 8 nm in organic medium.[23] Size of nanoparticles could be controlled by an imposed current density, and particles would be stabilized by an organic medium or by adsorption of cationic surfactants.

Spray pyrolysis. MNPs can also be produced by spraying a solution into a series of reactors where solvents of aerosol droplets undergo evaporation. A solute condense is followed by the precipitation of nanoparticles at a higher temperature.[24]

Laser pyrolysis. In laser pyrolysis, a mixture of gas is heated with a laser that initiates and sustains a chemical reaction inside a reaction zone.[25] The reaction is designed in such a way that it provides an ideal environment for the nucleation of particles. The homogenous nucleation of particles is achieved above a certain pressure and laser power. In this process, nanoparticles can be produced with narrow size distribution and less aggregates. Pure samples of γ-Fe_2O_3 with a narrow size range of 3.5 and 5 nm have been produced using this method.[26] Others have used this method in the production of iron oxide nanoparticles using iron pentacarbonyl as starting material and laser radiation to oxidize iron in the presence of air.

1.1.3 Properties of magnetic nanoparticles

There are several properties of MNPs that affect their use in biotechnology including: particle dispersion, size, shape, and superparamagnetism behavior.[27] For biotechnology applications that will be discussed later in this chapter, it is necessary to produce single domain MNPs with good dispersion and narrow size distribution. However, most of the synthetic methods produce MNPs with large aggregates, wide distribution in size, and variation in shape. It has been reported that magnetization,

coercivity, and the Curie temperature of magnetic systems are sensitive to the mentioned parameters (dispersion, size, size distribution, and shape).[28]

The ideal magnetic nanoparticle for biological application is also based on the theory of superparamagnetism. This theory presumes MNPs are a single domain with atomic magnetic moments. It also presumes that by rotating coherently the magnetization of the particle corresponds to a single magnetization vector with a large magnitude.[29] The time that it takes to reverse the magnetization of the particle from one equilibrium magnetization state to the other is denoted by relaxation time; which depends on a constant anisotropy and volume of the particles. Furthermore, the magnetization magnitude of a single domain magnetic nanoparticle depends on its size and shape. The magnetization properties of single domain nanoparticles have been studied using micromagnetic modeling or Monte Carlo simulations; which have shown the strong influence of size and surface effects on magnetic properties.[30, 31] These studies have also demonstrated that conventional methods such as sol-gel and sputtering may not produce MNPs with well separated magnetic single domains. It was suggested that self assembly of MNPs by biomolecules might be the best alternative.

1.1.4 Encapsulation of magnetic nanoparticles

Materials. The limitations of MNPs in biotechnology are their cytotoxicity and aggregation. These limitations can be improved by encapsulating MNPs with suitable materials such as polymers, non-polymer materials, and inorganic molecules.

Encapsulation of MNPs also renders them to be more soluble in aqueous or biological media and provides various functional groups on the surfaces for the conjugation of biomolecules. However, surface coatings of magnetic particles may result in the decreased saturation magnetization values of the particles, as shown by various studies.[1, 4, 9] Thus, encapsulation of MNPs needs to be designed with optimization between these two factors: aggregation and magnetization. An interesting strategy is to encapsulate MNPs with materials incorporating electrostatic or electrosteric repulsion.[1, 4, 9] These materials prevent particle aggregation by an electrical repulsion. This leads to producing thinner layers of coating and decreases reduction of magnetic properties for the encapsulated MNPs.

To produce the polymer MNPs, a great variety of polymers have been used. These include natural polymers such as albumin, cellulose, pullulan, and chitosan. Additionally they include synthetic polymers like polystyrene, polyethylene glycol (PEG), poly acrylamide, and poly (L-lactic-co-glycolic) acid (PLGA).[9, 32-34] Furthermore, dextran or liposomes are well-known for their use in coating MNPs for drug or gene therapy delivery applications.[3, 35-40] In the following section, only temperature sensitive polymers will be discussed.

Temperature sensitive polymers used to coat MNPs include poly N-isopropylacrylamide (PNIPA) and its copolymers. The main advantage of these materials is that they are temperature sensitive. PNIPA undergoes a reversible volume

phase transition at a lower critical solution temperature (LCST) of 32°C. It is at this LCST that the hydrogel hydrophobically collapses, expelling water in an entropically favored fashion. These reversible swelling and shrinking events have been used as a means to control uptake and release of various therapeutic agents. The LCST can also be increased to slightly higher than a body temperature of 37°C when using its copolymer, poly(N-isoprolylacrylamide-co-acrylamide).[7, 41, 42] These nanoparticles are referred to nanogels due to their size and physical properties.[43]

Nanogels are usually made from two major groups of hydrogels: physical and chemical gels. Physical gels, known as pseudo-gels or "reversible gels," contain chains that are bound by weak bonds such as electrostatic forces, hydrogen bonds, hydrophobic interactions, or chain entanglements. The interaction of two oppositely charged polyelectrolytes also leads to the formation of physical hydrogels known as 'ionotropic' hydrogels. A major limitation of physical gels is that these gels are not permanent. The interactions to form physical gels are reversible and can be disrupted by changes of physical conditions including ionic strength, concentrations, pH, and temperature. Unlike physical gels, chemical gels known as true-gels are permanent. In these gels, chains are linked together by covalent bonding. Chemical gels can be prepared by various methods such as crosslinking or copolymerizing combined with crosslinking.[44-47]

One special type of nanogels is "smart" or stimulated-responsive hydrogels, which tend to swell or shrink rapidly in response to the external environmental stimuli, such as change in pH, temperature, ionic strength, and electro stimulus. This volume transition phase makes hydrogels of great interest, especially in the drug delivery system.[48-50] For instance, temperature sensitive hydrogels made from N-isopropylacrylamide (NIPA) and its copolymers are in their swollen state at temperatures below a LCST, where the transition phase takes place. As the temperature is increased above the LCST, the hydrogen bonds begin to break and the hydrophobic state becomes more desirable, causing the nanoparticles to collapse, shrink, and release the materials embedded inside of them. This is a major advantage of these "smart" nanogels since drugs can be loaded in these nanogels at low temperatures. These nanogels will then be delivered to specific locations and drugs will be released when the temperature is increased above the LCST. The LCSTs can be altered by copolymerization with other monomers. In general, the addition of hydrophilic monomer induces the LCST due to the increase of the hydrogen bonds, which in turn requires higher temperatures for bond breaking. In contrast, the addition of hydrophobic monomers have reverse effects.[48, 49, 51]

The transition phase of hydrogels can be studied using various techniques, such as ultraviolet visible spectroscopy (UV/VIS), nuclear magnetic resonance (NMR) spectroscopy, turbidity, calorimetry, viscosimetry, fluorescence, and attenuated total reflection (ATR)/ Fourier transform infrared (FTIR) spectroscopy. Specifically, the

LCSTs of hydrogels are being found by measuring the swelling ratio as a function of temperature. However, this measurement consumes a lot of time, and it is very difficult to reproduce precise results. In addition, LCSTs can also be determined by measuring the cloudiness of the nanogels while heating it. The cloudiness indicates that nanoparticles are shrinking in size, therefore the solution is getting denser.[52]

Techniques. Several methods have been applied to encapsulate magnetic nanogels or generate polymer MNPs. These techniques include traditional coating, emulsion polymerization, miniemulsion polymerization, in situ polymerization, and photochemical polymerization.[48, 53] Some of these methods involve complex processes, excessive processing time, and expensive costs. Other methods incorporate polymers onto MNPs without a strong bond. Thus, MNPs often diffuse out of the polymer matrix. This results in biocompatibility problems and defeats the purpose of having magnetic based nanoparticles.[48] To overcome this issue, one strategy is to incorporate MNPs with a bi-functional group of intermediate materials and polymerize the polymers on the other end of these intermediates. This method has been shown to successfully produce magnetite nanoparticles conjugated with copolymers of PNIPA and 2-carboxyisopropylacrylamide (CIPAAm).[54] The nanoparticles were shown to have a sensitive and reversible hydrophobic-hydrophilic change in response to temperature, and the shell thickness around the magnetic nanoparticle core was approximately 10 to 20 nm. The polymerization of the monomers is based on free radical polymerization.[55] In this process the reaction is initiated via free-radical

initiator. The free radicals can be created by photosensitive (e.g. bromine), temperature sensitive (e.g. potassium persulfate), or oxidization-reduction system (e.g. ammonium persulfate). These free radical molecules are unstable and easily break down to initiate polymerization. The radicalized molecules undergo a rapid reaction with monomers in the solution to propagate and polymerize in order to create a repeating chain. After formation of the polymer, the reaction terminates by coupling two radical species together or chain disproportionation, two radical chains exchange a proton in the solution.[55]

Another interesting incorporating technique to produce polymer MNPs is emulsion polymerization. For instance, Poly (methyl methacrylate) (PMMA) MNPs were synthesized using a soapless emulsion polymerization by Young et al.[56] In this method, nanoparticles with uniformly small sizes in the range of 100 ± 50 nm were produced. Extensive coagulation of MNPs also took place during polymerization in the monomer rich condition. The particle coagulation would occur more rapidly when magnetic nanoparticle concentration is high. This consequently resulted in a decrease of the polymerization rate.

One of the extensively used methods to functionalize the surface of MNPs is by utilizing an alkoxysilane coupling agent. MNPs coated with 3-aminopropyl triethoxysilane (APTS) was prepared by Ma et al.[8] MNPs were coated via acid catalyst hydrolysis followed by electrophilic substitution of silane on the surface of the MNPs.

APTS-coated MNPs were approximately 7.5 nm in diameter. Results from enzyme linked assays indicated that APTS-coated MNPs significantly improved the protein immobilization.

1.2 Applications of magnetic nanogels

1.2.1 Drug / Gene Delivery

MNPs have brought about a paradigm shift in the field of targeted drug/gene delivery as they offer several advantages compared to conventional drug delivery methods. The most important advantage of MNPs is that drug-loaded MNPs can be locally recruited to the target site by an external magnetic field, and thus the drug side effects can be reduced.[4, 57] The direct application of the drug at the target site also requires smaller amounts of the administered drug, thereby reduces the drug toxicity and side effects. These advantages make MNPs a major candidate to deliver drugs for treatment of various diseases. One such disease is cancer as these targeted carriers could reduce the side effects caused by the chemotherapeutic agents on the healthy tissue. This would allow treatment to be more effective and less painful for the patient; thereby ensuring continuation of the treatment until satisfactory regression of the tumor is observed.

Indeed, MNPs have shown promise as carriers for chemotherapy to treat various cancers. Magnetic carriers to deliver doxorubicin were first tested on sarcoma tumors in rat tails showing complete remission of the tumors compared to no remission in the

control group that had ten times the dosage.[58] Similar results have also been observed in various animal models.[59-64] Furthermore, phase I clinical trials have been carried out by Lübbe et al. where epirubicin was conjugated to the magnetic carriers.[65] Results from these trials found that organ toxicity did not increase. However, further improvements are necessary to make these magnetic carriers more effective. In addition, FeRx Inc. has been granted approval to proceed with phase I and II clinical trials to test their magnetic carrier systems for treatment of hepatocellular carcinomas.[66]

Besides drug delivery, delivery of radionuclides is an exciting application of MNPs. MNPs can be used to locally deliver the radionuclides at the targeted tumor site and allow the radiation to only affect the tumor tissue. Work has been done by Häfeli et al. using Yttrium-90 coupled to magnetic carriers in both *in vitro* and *in vivo* models.[67-70] The coupling of Yttrium-90 with magnetic carriers was found to concentrate the radioactivity better at the desired site compared to treatment without these carriers. The *in vivo* rat model showed that the amount of radioactivity actually delivered to the tumor increased from 6% as observed without carriers to 73% with magnetic carriers. Developing localized therapeutic methods for early stage treatment of cancer has been attracting much attention in the past decade. For instance, prostate cancer therapy with radioactive ^{125}I or ^{103}Pd seeds has introduced low and intermediate risks for prostate cancer patients.[71] However, even though these therapeutic methods have been adopted in clinics, there are several complications associated with them. For instance, complications such as erectile dysfunction,[72] urinary retention,[73] severe radiation

induced bowel injury,[74] and failure to eradicate localized therapy has resulted in poor post effect and local recurrence.[75] Delivery of the therapeutic drugs via nanoparticles which allows for a controlled and targeted delivery directly to cancer cells would reduce the above complications.

Another interesting application of MNPs is in the field of gene therapy. Gene transfection using MNPs, called magnetofection, was first carried out in C12S cells (*in vitro)* and in mice (*in vivo)* using an adeno-associated virus coupled to MNPs.[5] Magnetofection follows a principle similar to using MNPs for drug delivery. The procedure involves the coupling of DNA materials to the MNPs and introducing these particles in the cell culture. Placement of magnets below the culture enhances the settlement of the genetic materials in direct contact with the cells. The transfection is increased by a constant attractive force on the nanoparticles towards the magnet. This technique allows the use of low doses of genetic materials and very short incubation times to give satisfactory responses as compared to higher doses and longer incubation times of standard DNA delivery methods.[76-78] In addition, Krötz et al. have successfully applied magnetofection in delivering antisense oligonucleotides to human umbilical vein endothelial cells (*in vitro)* and in mice models with transfection levels up to 84%.[79] Oscillating magnet arrays can be used to further improve the transfection efficiency. By the addition of the oscillation motion of the MNPs, initial studies showed that it could increase the transfection ten fold in comparison to the static fields.[5]

1.2.2 Hyperthermia

MNPs, in the presence of an alternating magnetic field, generate heat which is used to kill cancer cells and eliminate tumors. Cancer tumors have been shown to be sensitized and more responsive to anti-cancer treatments when the tumors are exposed to prolonged heat at temperatures between 40-46^{o}C.[80-82] The prolonged heating of the tissue in the range of 40-46^{o}C is known as hyperthermia, and it has been used for treatments of various cancer diseases. Different mechanisms such as protein coagulation membrane fluidity and nucleic acid modifications might be responsible for the cancer killing seen in hyperthermia.[83, 84] Although several methods such as radio-wave, microwave, ultrasound, and infrared radiations have been used to cause hyperthermia, these techniques lack specificity as they are not able to guide the drug carriers to the cancerous tissue.

The use of MNPs is an excellent alternative for inducing hyperthermia and overcoming the specific limitation of other techniques mentioned above. Typically the nanoparticles will be injected intravenously and guided by the external magnetic gradient to the target tumor site. Exposure to the alternating magnetic field results in the oscillation of the magnetic moment inside the particles to release energy in the form of heat, which is transferred to the surrounding tissue. Since the MNPs can be guided to the specific tumor site, the risk of injuring the surrounding healthy tissue is minimized. However, it remains to be seen how the model can be scaled up for human as it might be unsafe to use high alternating fields required to produce sufficient heat for

hyperthermia treatments.[66] Another limitation is that the magnetic-inducing hyperthermia can only be applied to the organs or tissue (e.g. skin) that is easily accessed with the magnetic field.

1.2.3 Imaging

Another exciting application of MNPs can be found in the field of *in vivo* imaging as these nanoparticles are used as contrast enhancers for MRI. For example, MNPs have been used for the imaging of various tissues in a number of studies. Harisinghani et al. showed that even unmodified iron oxide nanoparticles improved the detection of lymph node metastasis in patients with prostate cancer from 34.5% to 90.5%.[85, 86] In addition, since the MNPs are taken up easily by the reticuloendothelial system (RES), it becomes easier to visualize the liver, spleen, and bone marrow in the MRI when using these nanoparticles.[87, 88] Superparamagnetic iron oxide nanoparticles are also commercially available for imaging of the gastrointestinal tract[81, 89, 90] and tumors of the liver [91, 92] and spleen.[2, 93] Furthermore, ultra small iron oxide nanoparticles (size < 50nm) (USPIO) have a longer circulating time in the body and their applications include imaging of tumor angiogenesis,[94] brain, heart,[95] and kidneys.[96] Additionally, these nanoparticles are under clinical evaluation for detection of cancer metastasis using MR lymphography (Sinorem®).[2, 97-99] Sinorem® nanoparticles are used for the detection of brain tumors and also permit an accurate delineation of the tumor margin.[57, 100] Another interesting field of imaging is using iron oxide nanoparticles in the monitoring of gene expression following gene therapy. USPIO incorporated with

proteins such as transferrin receptors have been shown useful for mapping the topography of transfected genes.[80, 81, 101]

1.3 Nanoparticle toxicity

The toxicity of magnetic nanoparticles made of iron and their derivatives has been studied. Only a small amount of iron oxide magnetic nanoparticles are used as contrast agents for MRI diagnostic imaging (50 to 200 mg Fe) compared to the body's normal iron storage (3000-4000 mg Fe).[2, 83, 98] The human body contains iron or iron oxides in the form of haemosiderin, ferritin, and transferrin.[2] Iron oxide magnetic nanoparticles can be broken down into these forms. The normal liver contains approximately 0.2 mg Fe/gram, and the chronic iron toxicity in liver occurs when this concentration exceeds 4mg Fe/mg.[91] Since there is only a small dose of iron oxide magnetic nanoparticles used in clinical imaging applications, the aspect of iron overload or iron toxicity is unlikely. Although the toxicity of magnetic nanoparticles is low due to the small dosage, the major harmful effect of magnetic particles is due to their aggregation, which can block the blood flow in blood vessels. Encapsulation of magnetic nanoparticles with polymers including N-isopropylacrylamide has been used to reduce this effect.[8, 42, 54, 87]

Although there is no standard protocol to measure the cytotoxicity of nanoparticles, several assays have been developed to analyze the cytotoxicity effects of nanoparticles before their use in human. For instance, MTT (3-(4,5-dimethylthiazol-2-

yl)-2,5-diphenyltetrazolium bromide) assay is a quantitative and rapid colorimetric method to assess the cell viability based on the change of MTT, a yellow tetrazolium salt, to insoluble purple formazan crystals by the mitochondrial dehydrogenase in viable cells.[102] Thus the number of viable cells can be determined by spectrophotometrically measurement of the cell solution. Furthermore, cell membrane damage due to nanoparticle internalization can be determined by measuring the activity of lactate dehydrogenase (LDH) from the dead cells leaked into the culture media.[103]

1.4 Prostate cancer

1.4.1 Overview of prostate cancer

In the male reproductive systems the prostate is responsible for making and storing seminal fluid. It is located in the pelvis below the urinary bladder. Due to its location, any prostate disease affects the organs surrounding it, e.g. bladder, urinary track, and rectum. In prostate cancer the cells responsible for making seminal fluid are mutated into cancerous cells, and begin to grow and multiply disorderly. Prostate cancer (PCa) or carcinoma of prostate (CaP) is a disease developed in the prostate gland. It is one of the prominent cancers affecting the male population around the world. PCa occurs most frequently in the African American population and is lowest in the Asian population according to the American Cancer Society. Genetics,[104] dietary habits,[105] and lifestyle[106] are important factors in PCa development. After a certain stage of cancer, the cells metastasize from the primary site (prostate) to secondary sites (e.g. bone marrow, lymph nodes, and lungs). At this stage the treatment of PCa becomes difficult.

According to the American Caner Society, the predicted new cases of prostate cancer in the year 2008 are approximately 186,320 patients. It is also estimated that the mortality will be approximately 28,660 of these patients. Finally, prostate cancer is the second leading cause of death in men (lung cancer is number one). Therefore, developing localized therapeutic methods of prostate cancer has been attracting much attention in the past decade.

1.4.2 Current treatment and their limitations

The current treatment options for prostate cancer are surgery (e.g. radical prostatectomy, transurethral resection of the prostate, and cryosrugery) radiation therapy (e.g. external beam radiation therapy, ^{125}I or ^{103}Pd seeds), hormone therapy (e.g. anti-androgens, luteinizing hormone-releasing (LHRH) analogs, and LHRH antagonists), and chemotherapy (e.g. doxorubicin, mitoxantrone, and paclitaxel). Out of all the treatment options mentioned above, radioactive therapy with ^{125}I or ^{103}Pd seeds has introduced low and intermediate risks for prostate cancer patients.[71] Even though all of these therapeutic methods have been adopted in clinics, there are several complications associated with these therapies. For instance, complications such as erectile dysfunction,[72] urinary retention,[73] severe radiation induced bowel injury,[74] and failure to eradicate localized therapy has resulted in poor post effects and local recurrence.[75] Delivery of the therapeutic drug via nanoparticles that allow for a controlled and targeted delivery directly to cancer cells would reduce the above complications.

1.5 Overview of research project

1.5.1 Goals/objectives

As shown in previous sections, temperature sensitive coated MNPs may play a potential role in drug delivery and imaging applications. However, the use of temperature sensitive coated MNPs in drug delivery is limited due to their low lower critical solution temperature (LCST) and absence of functional groups for bioconjugation. Therefore, the **overall objective** of this project was to develop a controlled and targeted drug delivery system using magnetic-based nanoparticles for prostate cancer treatments. Polymer coated MNPs were chosen for this purpose. To overcome the limitations in synthesis of the polymer coated MNPs mentioned earlier, a novel manufacturing method was investigated. In this method, MNPs were covalently attached to the polymer coat via a silane coupling agent. Furthermore, in order to adjust the characteristics of the polymer coat for the controlled and targeted drug delivery system, the NIPA-AAm-AH was introduced to provide drug release in a controlled fashion and for bioconjugation. Acrylamide (AAm) was copolymerized with NIPA in order to increase the lower critical solution temperature (i.e. temperature at which the physical state of the thermo-sensitive polymer changes) above body temperature. Allylamine (AH) was also copolymerized with NIPA-AAm in order to incorporate molecules such as antibodies onto the nanoparticle surfaces to enhance their targeting capabilities. Figure 1.1 displays the proposed nanoparticle and Figure 1.2 represents the principle of the novel drug delivery system.

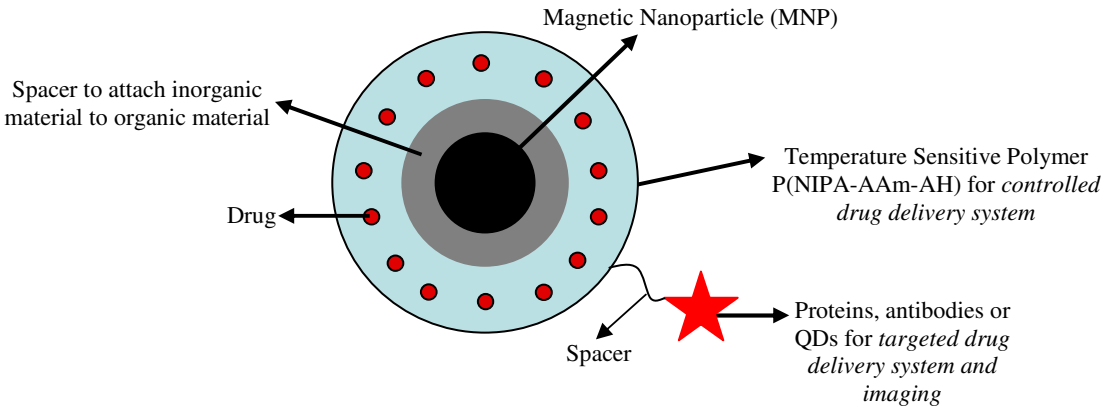

Figure 1.1 Proposed nanoparticle as a drug delivery system for prostate cancer treatment

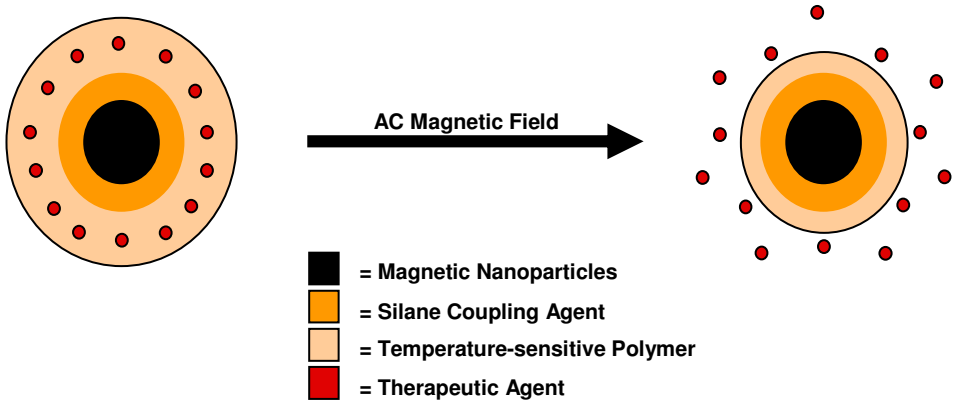

Figure 1.2 The principle of the novel drug delivery system. In order to release drugs, the AC magnetic field generator will be used to induce heat via MNPs causing the polymer shell (NIPA-AAm-AH coat around the MNPs) to collapse upon itself and squeeze the drugs out.

1.5.2 Specific aims

In order to achieve our goal, three specific aims, listed below, will be pursued.

- Aim 1 – Synthesize temperature sensitive nanogels, and characterize their chemical composition, size, morphology, bioconjugation and drug release.

- Aim 2 – Synthesize polymer coated MNPs, and characterize their chemical composition, size, morphology, drug release, cytotoxicity, and cellular uptake.
- Aim 3 – Investigate the targeting capability of the designed magnetic nanogels in dynamic simulation using parallel flow chamber systems.

1.5.3 Innovative aspects

There are several novel steps created in the manufacturing of the system presented in Figure 1.1. The first novel aspect is the synthesis of the new NIPA-AAm-AH nanogel which has a LCST above body temperature and amine functional groups for bioconjugation. The second novel aspect of the system is the conjugation of polyethylene glycol (PEG) and quantum dots (QDs) on the surface of the novel nanogel. The third innovative aspect of the design was utilizing a silane coupling reagent to manufacture new polymer coated MNPs. These novel temperature-sensitive MNPs would provide an effective strategy for controlled and targeted drug delivery. Furthermore, they could serve as an addition to imaging applications.

1.5.4 Successful outcome of the project

A successful outcome for this project would be to provide a method for a controlled and targeted drug delivery system for prostate cancer. Nanoparticles based on this project could be used to treat superficial solid cancers.

CHAPTER 2

EXPERIMENTAL

2.1 Materials

Ferric chloride hexahydrate and ferrous chloride tetrahydrate were purchased from Fluka. Bovine serum albumin (BSA), sodium hydroxide, sodium dodecyl sulfate (SDS), docusate sodium salt (AOT), potassium persulfate (KPS), methylene-bis-acrylamide (BIS), vinyltrimethoxysilane (VTMS), acrylamide (AAm), allylamine hydrochloric acid (AH), ammonium persulfate (APS), *N,N,N',N'*-tetramethyl ethylene diamine (TEMED), N-(3-dimethylaminopropyl)-N'-ethylcarbodiimide hydrochloride (EDC), 2-(N-Morpholino)ethanesulfonic acid sodium salt (MES) buffer, acetic acid, doxorubicin hydrochloride (DOX), ethanol, and iron stain kit (prussian blue) were obtained from Aldrich and used as received. Fluor-PEG-SCM (FPS) was purchased from Lysan Bio, Inc. with a molecular weight of 3400. Quantum dots (QDs) were kindly donated by Dr. Wei Chen from the Physics Department at the University of Texas at Arlington (UTA). Phosphotungstic acid (PTA) with a concentration of 0.01 wt% were kindly donated from the Molecular and Cellular Imaging Facility at the UT Southwestern Medical Center. Prostate cancer cells (JHU-31 and PC-3) and fibroblast cells (3T3) were purchased from American Type Culture Collection (ATCC). Cell culture media, serum, supplements, and buffers, including Dulbecco's Modified Eagle's

Medium (DMEM), 1X trypsin-EDTA, penicillin-streptomycin, and phosphate buffered saline (PBS) were purchased from Invitrogen Corp. (Carlsbad, CA).

2.2 Methods

2.2.1 Nanogel synthesis

Synthesis of poly (NIPA) nanoparticles. N-isopropylacrylamide nanoparticles were synthesized by an emulsion polymerization reaction. Briefly, 1.54 g of NIPA monomer was dissolved in 90 ml de-ionized (DI) water. Cross-linker, BIS (26.2 mg), was then added along with surfactant, SDS (43.8 mg) to the reaction flask while continuous stirring. The solution was then purged with argon gas for 30 minutes at room temperature. Initiator solution was prepared by dissolving 62.4 mg of KPS in 10 ml DI water. KPS solution was then added to the reaction flask, and the reaction was occurred at a temperature of 70°C. After 4 hours of reaction, nanoparticles were dialyzed (molecular weight cutoff (MWCO) of 6000-8000 Dalton) against DI water for 5 days in order to remove surfactants and unreacted monomers. Dialyzed nanoparticles were lyophilized before analysis and use.

Synthesis of poly (NIPA-AAm) nanoparticles. Poly N-isopropylacrylamide-acrylamide (NIPA-AAm) nanoparticles were synthesized using the same method as described above for NIPA nanoparticles. The difference was the components and concentration of these components. 1.3644 g of NIPA monomer and 0.1756 g of AAm monomer were used for poly (NIPA-AAm) nanoparticles.

Synthesis of NIPA-AAm-AH nanoparticles. The polymerization of poly (N-isopropylacrylamide-co-acrylamide-co-allylamine) was carried out in de-ionized water at room temperature using BIS as the cross-linking agent, SDS as the surfactant, and APS and TEMED as a pair of redox initiators.[107] In brief, 1.108 g of NIPA, 0.143 g of AAm, 378 µL of AH, and 0.0262 g of BIS were dissolved in 100 ml of de-ionized water. SDS was added to the solution at various concentrations (1.53, 0.298, 0.198, and 0.0243 mM) under continuous stirring. The solution was purged with argon for 30 minutes. Then, 0.078 g of APS and 101 µL of TEMED were added to the solution and the reaction was carried out at room temperature under Argon for 2 hours. After the reaction was completed, the nanoparticles were dialyzed against de-ionized water using 10 kDa MWCO for 3 days to remove surfactants and un-reacted.

2.2.2 Characterization of nanogels

Particle Size and Particle Size Distribution. The size and size distribution of nanoparticles were measured in de-ionized water by the dynamic light scattering technology (Nanotrac. 150, Microtrac. Inc.). The size measurement was performed at room temperature (25^0C).

Transmission Electron Microscopy (TEM). TEM (JEOL 1200 EX) was used to determine the size and shape of the synthesized nanoparticles. In general, samples were prepared by drop casting an aqueous dispersion of nanoparticles onto a carbon coated copper grid. The grid was then dried at room temperature before viewing under the

microscope. The nanoparticles were stained with phosphotungstic acid (PTA) with a concentration of 0.01 wt% before observation.

Fourier Transform Infrared Spectroscopy (FTIR). Dried samples were dissolved in dichloromethane and a drop of this solution was placed on NaCl discs. FTIR spectra were recorded in the transmission mode using a Thermo FT-IR Nicolet-6700. The spectrum was taken from 4000 to 400 cm^{-1}.

^{1}H NMR and ^{13}C NMR Studies. ^{1}H NMR and ^{13}C NMR spectra were recorded at 25°C on JEOL 300 and 500 MHz spectrometers, respectively. Chemical shifts were measured relative to residual non-deuterated solvent resonances. The spectrum of the NIPA-AAm-AH was recorded in deuterated dimethyl sulfoxide (DMSO) solution.

LCST Determination. Optical transmittance of the aqueous nanoparticle solution (2 mg/ml) at various temperatures (25-45^{0}C with 1^{0}C intervals) was measured at 650 nm with a UV-Vis spectrophotometer (Cary 50 UV-Vis spectrophotometer coupled with PCB-150 circulating water bath).

Conjugation. In order to test our nanoparticles for future bioconjugation, either green fluorescent poly ethylene glycol with carboxylic activated group (PEG), CdTe quantum dots (QDs) coated with mercaptopropionic acid, or IgG conjugated to Texas Red was used as a conjugated biomolecule model. In order to conjugate PEG onto

nanoparticles, 0.01 g of NIPA-AAm-AH nanoparticle was dissolved in 0.5 ml of MES (0.1 M) buffer solution and 0.01 g of EDC was added. The reaction was mixed for 10 minutes at room temperature. 0.2 mg of Fluor-PEG-SCM (FPS) was added to the above solution and the reaction was stirred vigorously for 24 hours at room temperature under dark conditions. The solution was dialyzed (MWCO 100 kDa) under dark conditions against DI-H_2O for 1 week to remove unreacted FPS. The sample was lyophilized and resuspended in 50% glycerol in water before imaging.

CdTe nanoparticles coated with mercaptopropionic acid (MPA) were used in order to attach onto NIPA-AAm-AH nanoparticles. MPA coating of QDs would allow the attachment of QDs to the amine group of NIPA-AAm-AH via the carbodiimide chemistry. In brief, 0.005 g of NIPA-AAm-AH nanoparticles was dissolved in 0.3 ml of MES buffer solution, and solution was stirred for 20 minutes. In order to avoid cross linking reaction between nanoparticles, 0.002 g of SDS was added to the above solution and it was stirred for 40 minutes. Then, 0.7 ml of QDs (0.5 mM) solution was added, and the mixture was stirred for 15 minutes. Finally, 0.07 g of NHS and 0.07 g of EDC was added, and the conjugation reaction was occurred under stirring. After 24 hours, nanoparticle suspension was dialyzed (MWCO 100 kDa) before visualization under fluorescence enhanced optical microscope (cytoviva).

In order to test the conjugation capability of the NIPA-AAm-AH nanoparticles, Texas Red IgG-TR (bovine anti-rabbit IgG-Texas Red) was also used. In brief, 0.01 g

of NIPA-AAm-AH nanoparticles was dissolved in 0.5 ml of MES (0.1 M) buffer solution and 0.01 g of EDC was added. The reaction was mixed well for 10 minutes at room temperature. 0.2 mg of IgG-TR was added to the above solution and the reaction was stirred vigorously for 2 hours at room temperature under dark conditions. The solution was dialyzed (MWCO 100 kDa) under dark conditions against DI-H_2O for 1 week to remove unreacted IgG-TR. The sample was lyophilized and resuspended in 50% glycerol in water before imaging by an enhanced optical fluorescent microscope (Cytoviva).

Cellular cytotoxicity. Cytotoxicity studies were carried out on 3T3 fibroblast cells (3T3, NIH) for 1 and 2 days using (3-(4,5-dimethylthiazol-2-yl)-5-(3-carboxymethoxyphenyl)-2-(4-sulfophenyl)-2H-tetrazolium (MTS) assays (following manufacturer (Promega)'s instructions). This assay is based on the competence of the live cells to reduce the MTS into formazan.[102] The nanoparticle dispersion in tissue culture media treated with the MTS solution alone was used as a baseline in order to make sure that the nanoparticles themselves did not give a positive result. The cytotoxicity results were presented as the percentage of viable cells in each sample in comparison to controls (cells not treated with the nanoparticles).

2.2.3 Magnetic nanoparticle synthesis

MNPs were prepared by a conventional co-precipitation method. In brief, ferric chloride hexahydrate and ferrous chloride tetrahydrate (2:1) were dissolved in 600 ml of

de-ionized (DI) water. After purging the solution with argon gas, 0.36 g AOT in 16 ml hexane was added as a surfactant, and the solution was heated to 85°C. At this temperature, 7.1 M NaOH was added. After a 2 hour reaction period, particles were washed extensively with ethanol and then centrifuged at 25000 rpm for 45 minutes. The magnetic nanoparticle was dried in a vacuum oven.

2.2.4 Polymer magnetic nanoparticles (PMNPs)

Preparation of VTMS–coated magnetic nanoparticles. The MNPs were coated with VTMS via acid catalyst hydrolysis, followed by an electrophilic substitution of ferrous oxide on the MNPs surface as shown in Figure 2.1 (a). In brief, 0.49 ml VTMS was hydrolyzed using 3 ml acetic acid in the presence of water and ethanol (1:100). MNPs were then dispersed by sonication at 100 W for 30 minutes in this solution; the product was then obtained after 24 hrs of vigorous mechanical stirring at room temperature. The product was excessively washed with a mixture of water/ethanol (1:100), and the particles were dispersed in water before the next step.

Immobilization of NIPA on surface of magnetic nanoparticles. VTMS–coated MNPs were used as a template to polymerize NIPA in an aqueous micellar solution as shown in Figure 2.1 (b). SDS and BIS were used as a surfactant and cross linking agent, respectively, as previously described. In brief, 0.028 g VTMS-coated MNPs, 0.0147 g NIPA, 0.0131 g BIS, and 0.041 g SDS were sonicated in 100 ml of DI water for 30 minutes. Then, the mixture was heated to 70°C and 0.069 g potassium persulfate

was added. The solution was stirred under Argon for 4 hours. The product was purified several times with DI water by using a magnet to collect only NIPA coated MNPs.

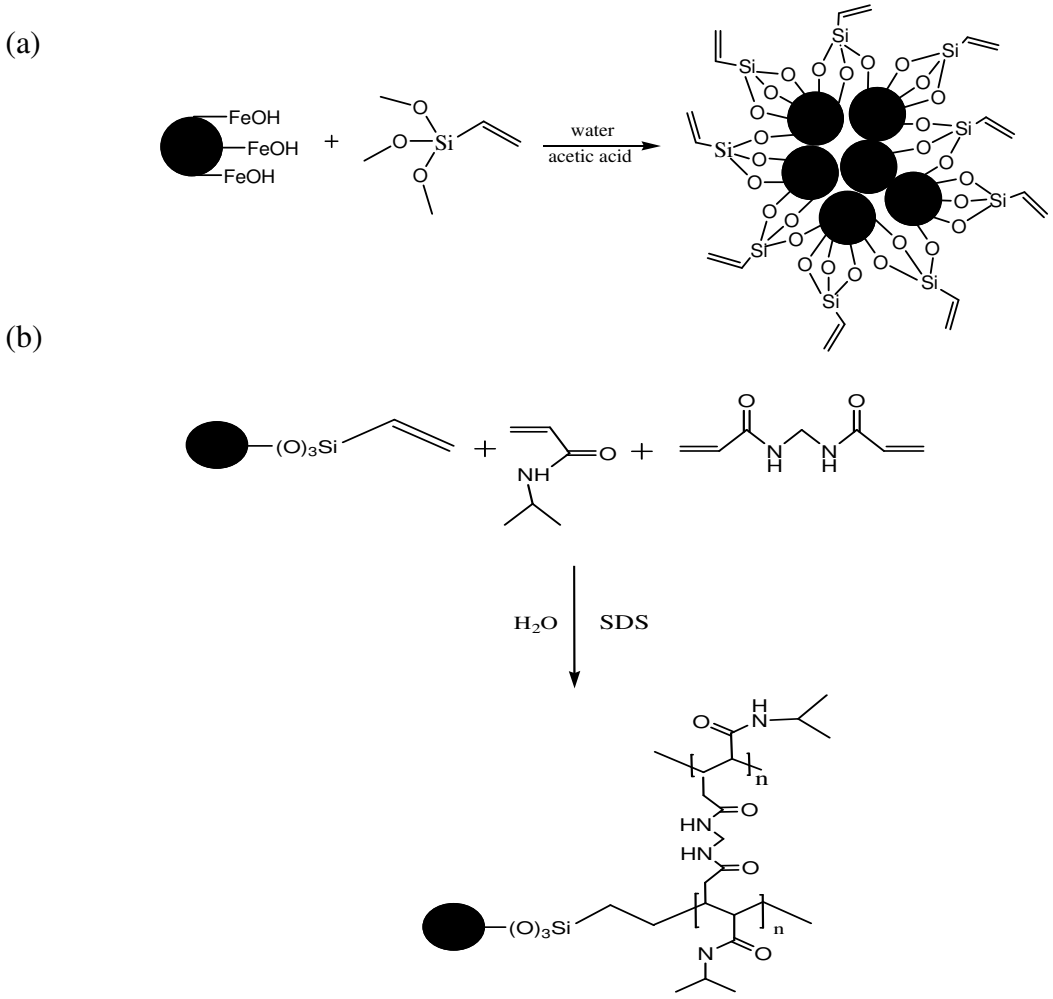

Figure 2.1 Preparation procedures of (a) coated MNPs with VTMS and (b) immobilization of NIPA on magnetic nanoparticle surface.

Immobilization of NIPA-AAm on surface of magnetic nanoparticles. VTMS–coated MNPs were used for polymerization of NIPA-AAm. For this immobilization, 0.028 g VTMS-coated MNPs, 0.124 g NIPA, 0.0159 g AAm, 0.0131 g BIS, and 0.041 g

SDS were used, and the reaction was performed similar to that of NIPA (section 2.2.4, page 30).

Immobilization of NIPA-AAm-AH on surface of magnetic nanoparticles. VTMS–coated MNPs were used as template to polymerize NIPA, AAm, and AH. In brief, 0.028 g VTMS-coated MNPs, 0.1 g NIPA, 0.0129g AAm, 0.0345 ml AH, 0.0131 g BIS, and 0.041 g SDS were sonicated in 100 ml cold water for 30 minutes. 0.078 g of APS and 101 µL of TEMED were added to the solution and the reaction was carried out at room temperature under Argon for 4 hours. The product was washed several times with DI water and purified using a magnet to collect only NIPA-AAm-AH coated MNPs.

2.2.5 Characterization of PMNPs

TEM and FTIR were performed similar to those of nanogels (section 2.2.2, page 25 and 26)

XPS *studies.* XPS measurements were carried out on the synthesized particles on a Perkin-Elmer PHI560 ESCA/SAM system using an Al *Kα* 1486.6 eV X-ray source. The resolution of the analyzer was 0.5 eV. Deconvolution was carried out with Gaussian functions. Chemical states of various elements were obtained using binding energies from the literatures. The atomic percentage of the elements present in the particles was calculated from the ratio of the net intensities of corresponding peaks, corrected using the instrument's sensitivity factors.

SQUID measurements. A magnetic property measurement system with a SQUID-based magnetometer (Quantum Design) was used to obtain room temperature magnetic hysteresis loops for MNPs, silane-coated MNPs, and magnetic nanogels. Pre-weighed samples were placed in a gelatin capsule and the capsule, with sample, was mounted in a transparent drinking straw wherein the measurement was obtained.

2.2.6 Drug release

BSA Loading. For drug loading and release studies, bovine serum albumin (BSA) was used as a model protein. In brief, 0.06 g of lyophilized nanoparticles and 0.005 g/ml of BSA were dispersed in 20 ml of DI water. The solution was stirred at 4^0C for 3 days. The BSA encapsulated nanoparticle was separated from solution via an external magnet. The solution was then analyzed using a BCA protein assay kit (PIERCE) following the manufacturer's instructions to determine the amount of BSA in the dialysate. This value was then compared with the total amount of BSA used in the nanoparticle formulation protocol to determine the BSA loading efficiency of the particles. Loading efficiency was calculated according to the following formula:

$$\% \text{ Loading Efficiency} = \frac{\text{total [BSA] used in nanoparticle formulation - [BSA] present in solution}}{\text{total [BSA] used}} \text{ x } 100\%$$

Doxorubicin Loading. In addition to BSA, doxorubicin (anti-tumor drug) was used in order to assess the drug release profile of synthesized nanoparticles. In brief, 10 mg of NIPA-AAm-AH coated MNPs and 5 mg of DOX were dispersed in phosphate buffer solution (PBS). The solution was stirred at 4^0C for 3 days. The DOX

encapsulated NIPA-AAm-AH coated MNPs were separated from the solution via an external magnet. The solution was then analyzed using an Infinite M200 plate reader (Tecan) in order to determine the amount of un-encapsulated DOX (λ_{ex} 470 nm and λ_{em} 585 nm). This value was then compared with the total amount of added DOX to determine the DOX loading efficiency of the nanoparticles. Loading efficiency was calculated according to the following formula:

$$\% \text{ Loading Efficiency} = \frac{\text{total [DOX] used - [DOX] present in dialysate}}{\text{total [DOX] used}} \text{ x } 100\%$$

In vitro Drug Release Kinetics. In order to study the BSA release profile of the synthesized nanoparticles, 2 ml of drug loaded nanoparticle solution described earlier was placed inside dialysis bags with MWCO of 100,000. Samples were dialyzed against de-ionized water at different temperatures. At designated time intervals, 1 ml of dialysate was removed from each sample and stored at -20^{0}C for later analysis. Dialysate volume was reconstituted by adding 1 ml of fresh de-ionized water to each sample. Dialysate samples were analyzed using the BCA protein assay kit to determine the amount of BSA released into the dialysate following the manufacture's instructions. The DOX release studies were similar to the BSA release studies, except that dialysis bags with MWCO of 10,000 Da were used and that the dialysate samples were read at λ_{ex} 470 nm and λ_{em} 585 nm.

2.2.7 Cellular cytotoxicity

In order to assess the biocompatibility of NIPA-AAm-AH-MNPs, the cytotoxicity was tested by measuring lactate dehydrogenase (LDH) released from 3T3 fibroblast cells after exposure to these nanoparticles. Nanoparticles were incubated in wells with 3T3 fibroblasts cells for 6 and 24 hours at various concentrations (0, 15.6, 31.2, 62.5, 125, 250, and 500 μg/mL). Two types of nanoparticles were used for this study, the original MNPs and the NIPA-AAm-AH coated MNPs. LDH released in the media from the damaged cells was analyzed using an LDH Assay (Promega Corporation), following the manufacturer's instructions.

2.2.8 Cellular uptake

In order to characterize *in vitro* behavior of our nanoparticles, cellular uptake studies were performed. Prostate cancer cells (JHU31, American Type Culture Collection (ATCC)) were cultured using DMEM (Invitrogen) supplemented with 10% fetal bovine serum (Hyclone) and 1% penicillin-streptomycin (complete DMEM). Cells were seeded at a density of approximately 10,000 cells/well in 24-well plates and allowed for cell adhesion and growth for 24 hours at 37°C. To investigate the effects of nanoparticle optimal dosage and incubation time, NIPA-AAm-AH coated MNPs were added at various concentrations (0, 125, 250, 300, 500, 800, and 1000 μg/mL) in the cell sample and incubated for 6 and 24 hours. After incubation, cells were lysed with 1% Triton in PBS. Similarly, to test for the optimal incubation time, 500 μg/mL of NIPA-AAm-AH coated MNPs were added to a 24-well plate and incubated for varying

durations (0, 0.5, 1, 2, 4, 6, and 8 hours). At predetermined times, the cells were lysed with 1% Triton in PBS.

To determine the amount of iron (Fe) uptake, we performed an iron content assay as previously described.[108] In brief, 500 µl cell lysate was incubated in 30% v/v HCL at 55°C for 2 hours and then 0.050 mg ammonium persulfate was added. After shaking for 15 minutes, 50 µl solution of potassium thiocyanate (0.1 M) was added, and the samples were shaken for another 15 minutes before being read using UV-Visible spectrophotometer at 478 nm. The remaining cell lysate was tested for DNA content using a Picogreen DNA Assay (Invitrogen Corporation, California) following the manufacture's instructions, and this data was used to normalize the iron content. In order to visualize the uptake of NIPA-AAm-AH coated MNPs, Texas Red (bovine anti-rabbit IgG-Texas Red) was conjugated to NIPA-AAm-AH coated magnetic nanoparticle as described in section 2.2.2 (page 28). Cells were incubated with TR-conjugated nanoparticles (500 µg/ml) for 4 hours. Zeiss LSM 510 META laser scanning microscope (LSM) with Chameleon XR NIR laser was then used to visualize the fluorescence nanoparticles within the cells.

2.2.9 Pharmacological activity of DOX loaded NIPA-AAm-AH coated MNPs

In order to investigate the pharmacological activity of DOX released from our nanoparticles, cancer cell viability was conducted using MTS assays (Promega Corporation). Prostate cancer cells (JHU31) were incubated with nanoparticles, DOX-

loaded nanoparticles, and free DOX. The same concentration of empty nanoparticles and DOX-loaded nanoparticles (500 μg/ml) was used in this study. We selected this nanoparticle concentration according to drug release results. The prostate cancer cells exposed to each group were incubated at either 37^0C, 41^0C, or temperature cycles between 37^0C and 41^0C (one hour cycle) for 24 hours. The cells exposed to media served as a control.

2.2.10 In vitro localization of magnetic nanogels

Flow chambers were used to study nanoparticle retention onto glass slides in the presence of an external magnetic field under physiological flow conditions. The flow chambers were consisted of a polycarbonate slab, silicon gasket, and glass slide (on top of the gasket) as shown in Figure 2.2. The system was held together using a vacuum pump (Gast Manufacturing, Inc., Benton Harbor, MI), and shear stress was generated using a syringe pump (KD Scientific, Holliston, MA). Wall shear stress (τ) for the flow chamber was calculated according to the following equation:

$$Q = \frac{\tau b h^2}{6\mu}$$

τ = shear stress (1 dyn/cm^2, 13 dyn/cm^2, 21 dyn/cm^2)
Q = flow rate (1 ml/min, 12 ml/min, 18 ml/min)
μ = Viscosity (0.01 dyn.sec/cm^2)
h = channel height (0.022 cm)
b = slit width (1.8 cm)

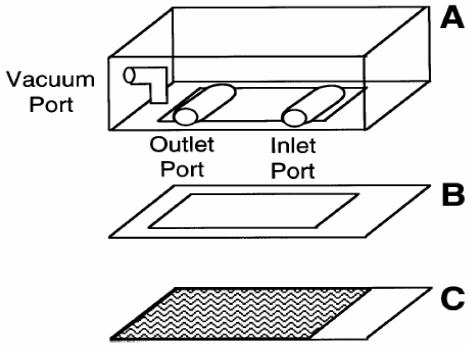

Figure 2.2. Schematic of a Parallel Flow Chamber. The chamber consists of (A) a polycarbonate slab, (B) a silicone gasket, and (C) a glass coverslip held together by a vacuum. A vacuum pump was connected to the vacuum port and a syringe pump was connected to the inlet port in order to generate shear stress. The glass cover slip was seeded with different types of cells.

For the flow studies, cells were seeded on glass slides as previously described.[109] In brief, cells were seeded on glass slides at a density of 10^5 cells/cm^2 and allowed to attach and grow for 2 days. Before conducting the experiments NIPA-AAm-AH coated MNPs (0.265 mg/ml) were dispersed into culture media via an ultra-sonicator. Glass slides containing cells (either endothelial cells, smooth muscle cells, or prostate cancer cells) were assembled into the flow system, and the particle suspension was perfused through them with or without an external magnetic field (3200 gauss). Three different values of shear stress (τ = 1 dyn/cm^2, 13 dyn/cm^2, and 21 dyn/cm^2) were studied by adjusting the flow rate of the flow system (Q = 1 ml/min, 12 ml/min, and 18 ml/min). The percentage retention of NIPA-AAm-AH coated MNPs was determined via measuring concentration of iron from input and output of the flow system. The iron

content of cell lysis samples from the glass slides were also measured after the experiments.

CHAPTER 3

RESULTS

In this research work we have manufactured controlled and targeted polymer MNPs. In order to manufacture these nanoparticles, two simplified interdependent routes were designed. First, the polymer nanoparticles (Nanogel) were synthesized and characterized. Second, polymer coated MNPs were formed and studied. By this way, we were able to fully characterize the polymer coat before the system become complex via introduction of a magnetic core. In addition, one of the most powerful instruments for polymer characterization, nuclear magnetic resonance (NMR), cannot be used when magnetic core is introduced.

N-isopropylacrylamide (NIPA) was chosen as the material for a polymer coat because NIPA is a temperature sensitive polymer and enables a controlled drug delivery system. Since the temperature sensitivity of NIPA is not in the range of body temperature, we have copolymerized NIPA with acrylamide (AAm) in order to bring the temperature sensitivity above body temperature. To enhance the targeting capability, the NIPA-AAm was copolymerized with allylamine which contains an amine groups for conjugation of other molecules such as antibodies. In the following

sections the characterization of the nanogels and polymer coated MNPs will be discussed.

3.1 Characterization of nanogels

In this section the synthesis and characterization of NIPA, NIPA-AAm, and NIPA-AAm-AH nanoparticles will be discussed.

3.1.1 Particle size and particle size distribution

The average sizes of the synthesized nanoparticles were analyzed using TEM. Due to the properties of nanoparticles, we coated the nanoparticles with phosphotungstic acid at a concentration of 0.01 wt% before TEM analysis. The black background around the nanoparticles is the negative stain that was used to define the particle outer edge (Figure 3.1). The TEM results revealed that the preparation procedure gave spherical nanoparticles with approximately 100 nm diameter.

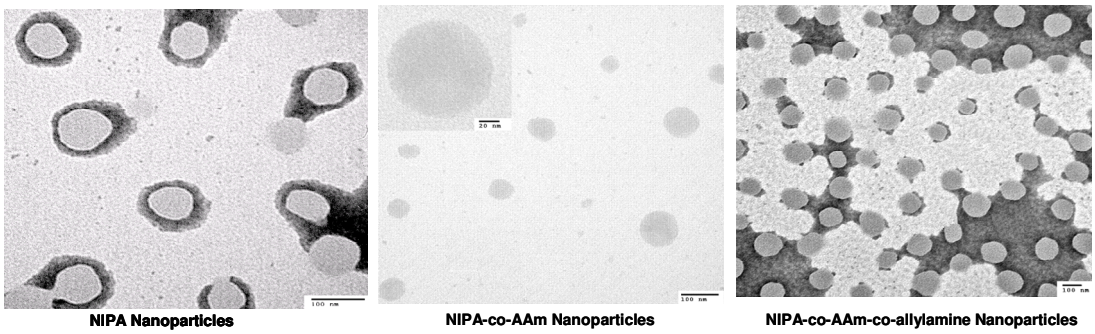

Figure 3.1. Transmission electron microscopy of synthesized nanogels

The size and size distribution of NIPA-AAm-AH nanoparticles were also analyzed using dynamic light scattering technology (Nanotrac). As shown in Figure 3.2, the size of nanoparticles were approximately 100 nm in diameter, and the size distribution was narrow.

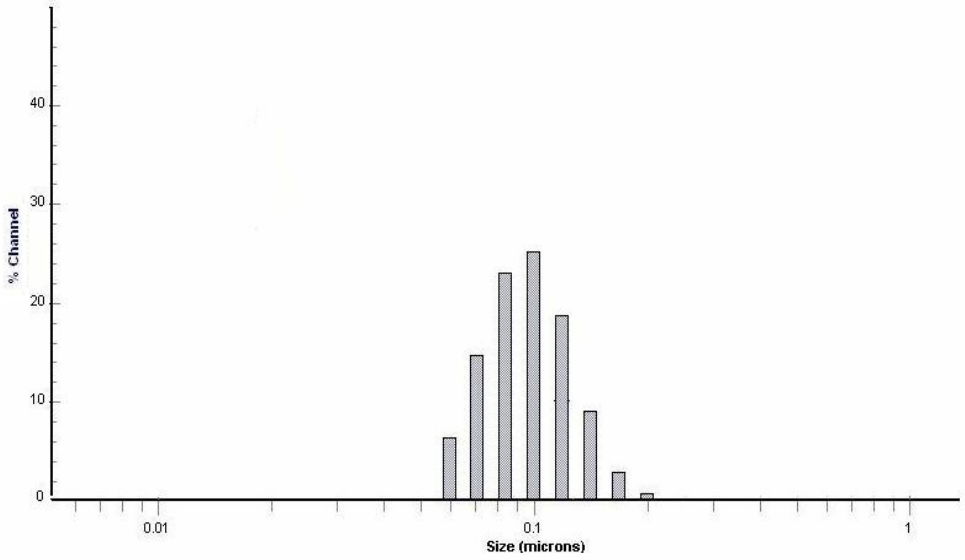

Figure 3.2. Particle size distribution of nanoparticles prepared with 0.198 mM SDS concentration.

In order to characterize the effect of surfactant SDS on the particle size, various SDS concentrations were used. The size of the nanoparticles increases as the concentration of SDS decreases as shown in Figure 3.3. It is evident that the size of the nanoparticles is inversely proportional to the concentration of SDS. This type of relationship between the surfactant and nanoparticle size is consistent with previous observations.[48] However, the relationship was found to be nonlinear at SDS concentrations higher than 0.298 mM.

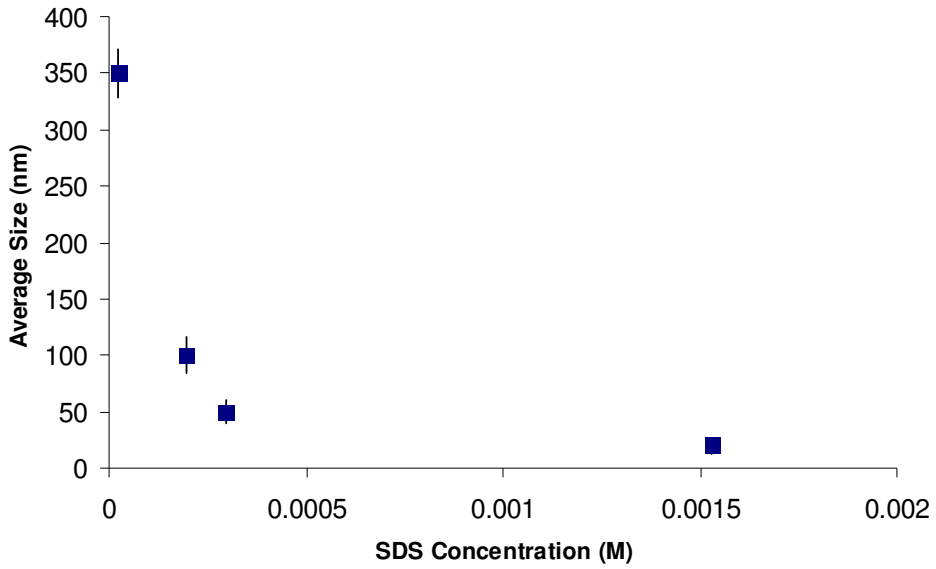

Figure 3.3. Effects of SDS concentrations on the mean size of nanoparticles (the result is represented as mean ± S.D., n=3) measured by dynamic light scattering.

3.1.2 Fourier transform infrared spectroscopy (FTIR)

The chemical compositions of the synthesized nanoparticles were analyzed using FTIR. The structures of NIPA, NIPA-AAm, and NIPA-AAm-AH are shown in Figure 3.4. The stretching vibration appearing in the range of 2900-3100 cm^{-1} corresponds to C-H bands in each of the three formulations (Figure 3.5). IR peak at 3423.6 cm^{-1} corresponds to the stretching vibration of the primary amine group in the NIPA-AAm-AH. The peak from the secondary amine group of NIPA is observed around 3308.7 cm^{-1}. Furthermore, the carbonyl group of NIPA and AAm is observed at 1655 cm^{-1}. These peaks indicate that the nanoparticles consist of functional groups corresponding to their constituent monomers.

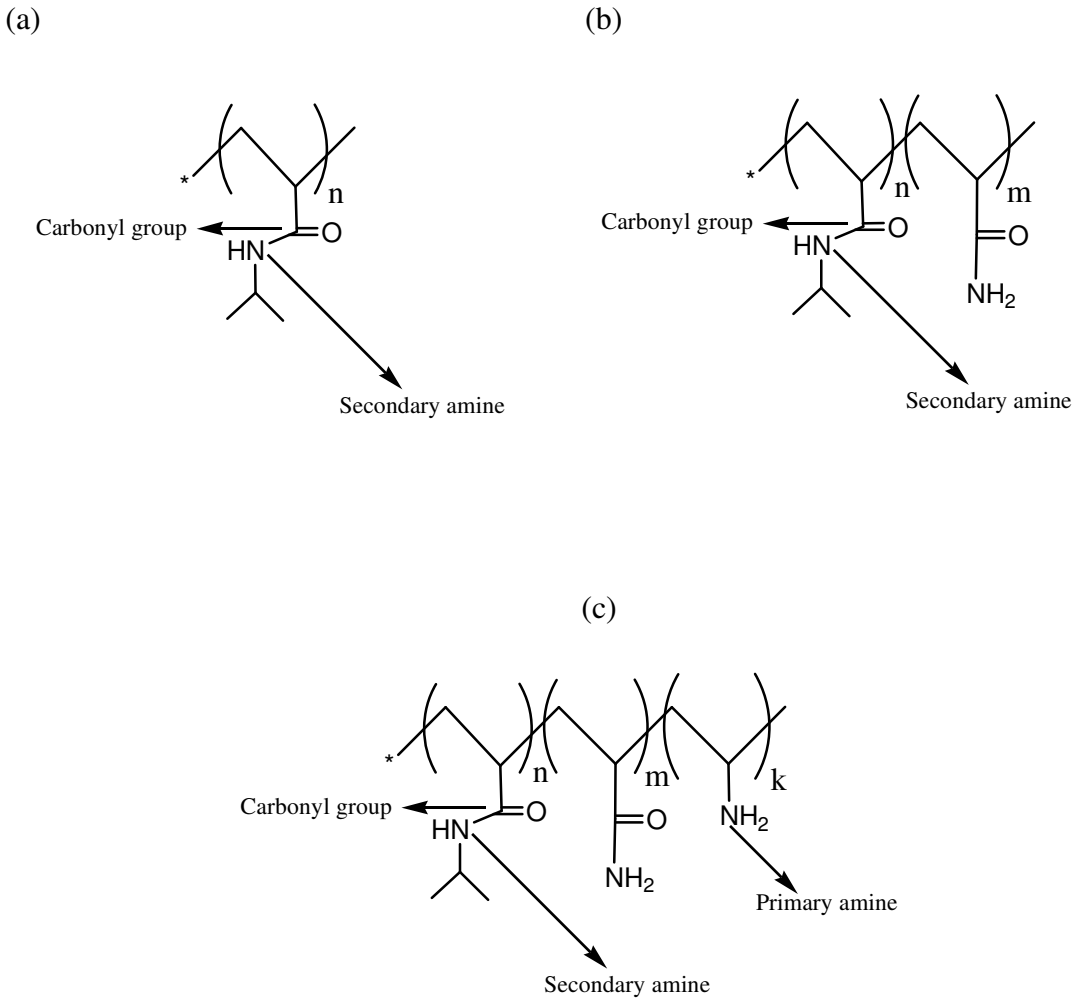

Figure 3.4. Chemical structure of (a) NIPA, (b) NIPA-AAm, and (c) NIPA-AAm-AH.

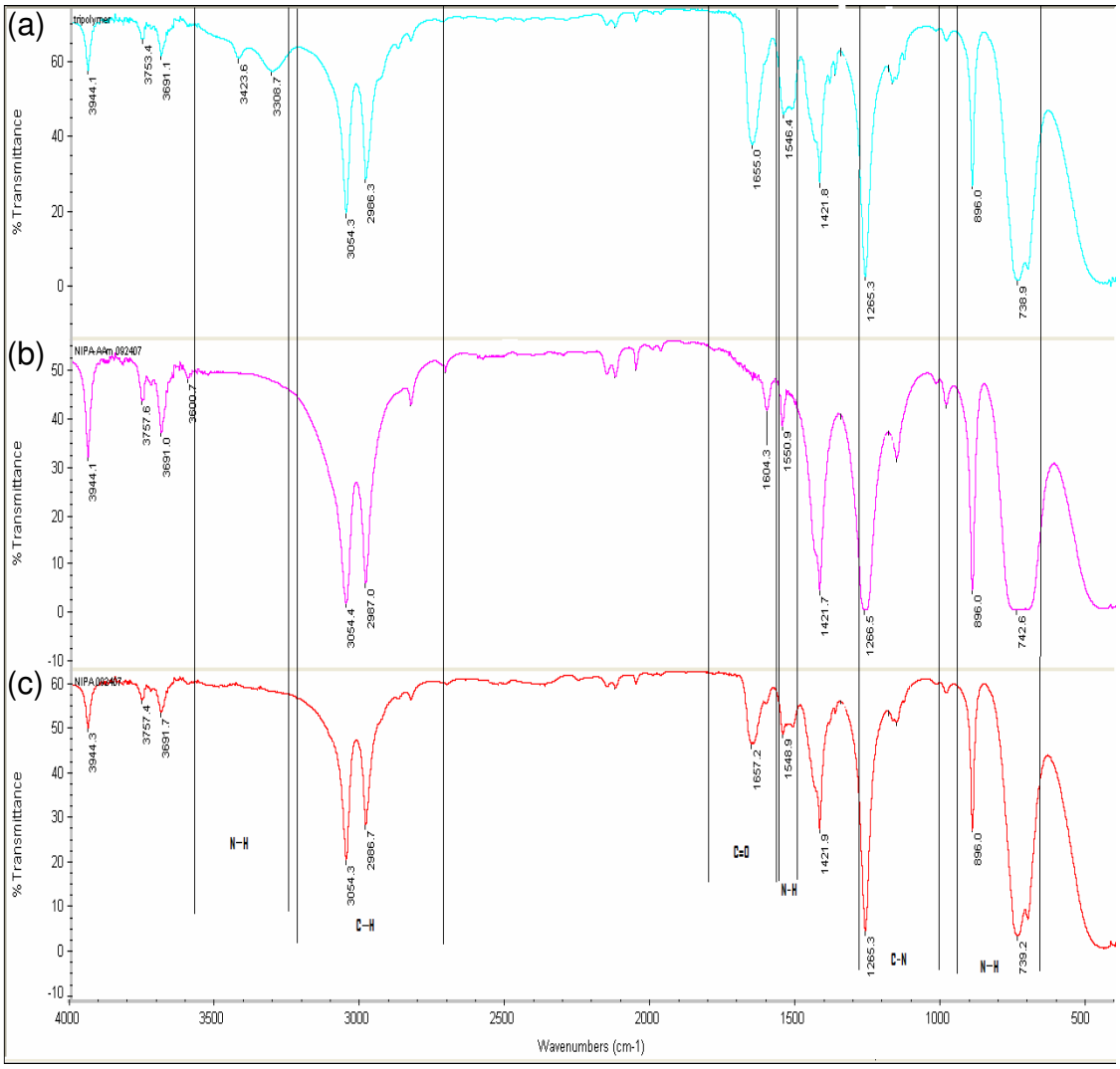

Figure 3.5. FTIR spectrum of (a) NIPA, (b) NIPA-AAm, and (c) NIPA-AAm-AH nanoparticles at room temperature (25^0C).

3.1.3 ^{1}H NMR and ^{13}C NMR studies

To chemically analyze the formation of the nanoparticles, we used both ^{1}H NMR and ^{13}C NMR. In ^{1}H NMR (Figure 3.6 a), we observed the backbone hydrogen of the nanoparticles at 1.89 (c, broad, 1 H) and 1.46 (b, broad, 2 H). The hydrogen attached to the isopropyl of NIPA was observed at 3.78 (d, multiplet, 1 H), and the

hydrogen of methyl groups in NIPA was observed at 1.02 (a, multiplet, 6 H). The broad peak at 7.40 to 7.80 ppm is from the hydrogen in the amide groups. The proton NMR of the nanoparticles did not show significant difference at first. However, only after we treated the NIPA-AAm-AH nanoparticles with hydrochloric acid did the peak from the amine group of allylamine disappear, which indicated the presence of the primary amine group in the nanoparticles (Figure 3.6 b). This was an additional indication of the allylamine copolymerization with NIPA-AAm.

(a)

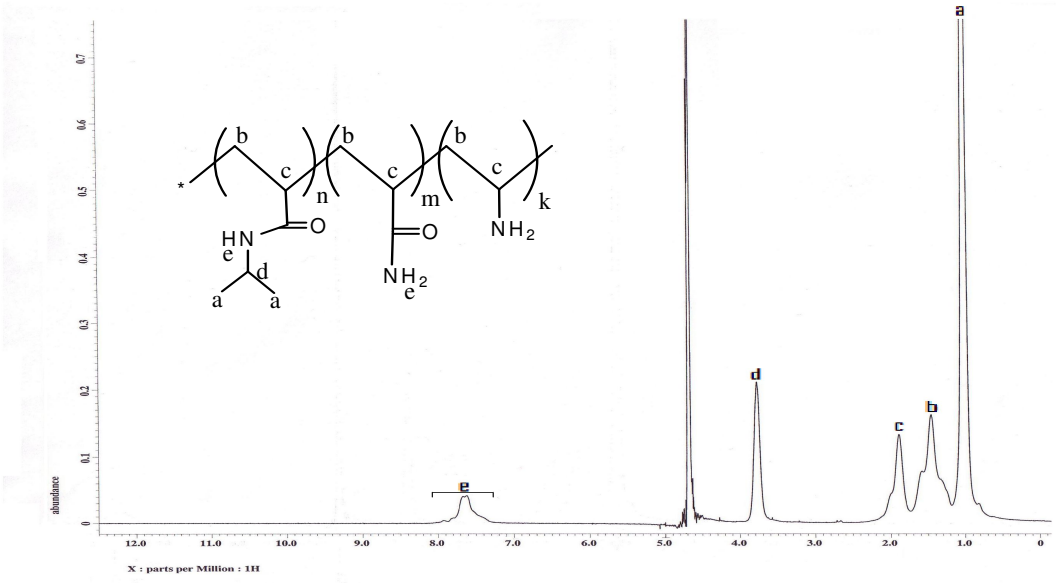

(b)

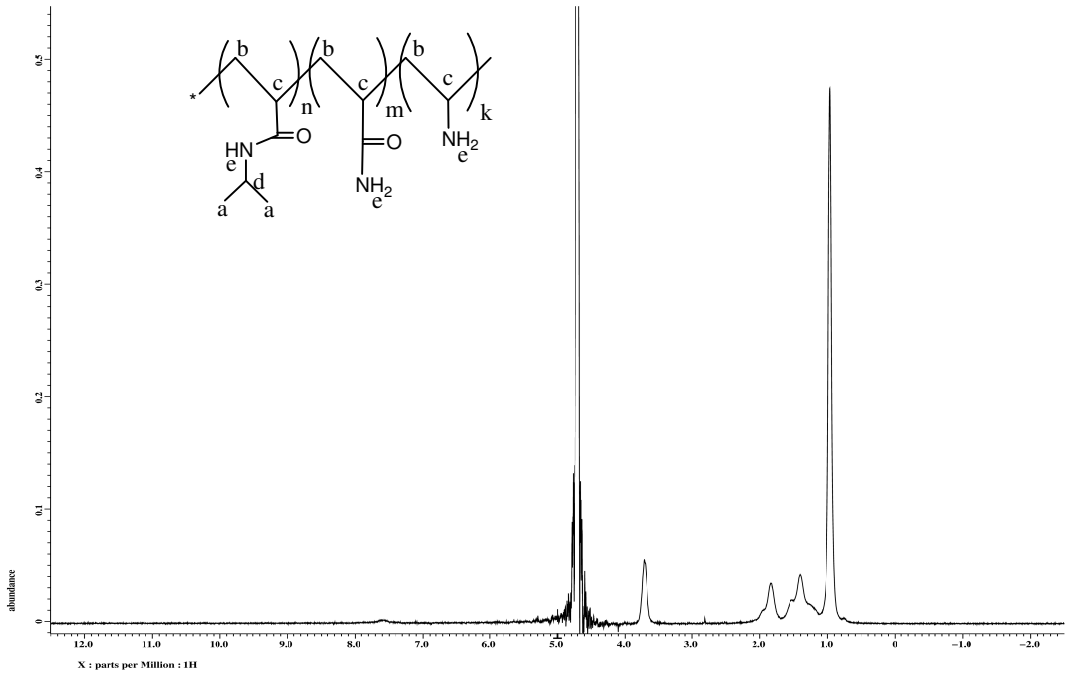

Figure 3.6. The proton NMR of the NIPA-AAm-AH nanoparticles (a) before and (b) after adding hydrochloric acid.

In the ^{13}C NMR of NIPA (Figure 3.7) we observed the backbone carbons at 35.90 (b) and a multiplet between 39 to 40.8 ppm (c). The isopropyl carbon in NIPA was observed at 42 (d), and the carbon of methyl groups in NIPA was observed at 22.80 (a). The peak at 173.79 ppm (e) is from the carbonyl group.

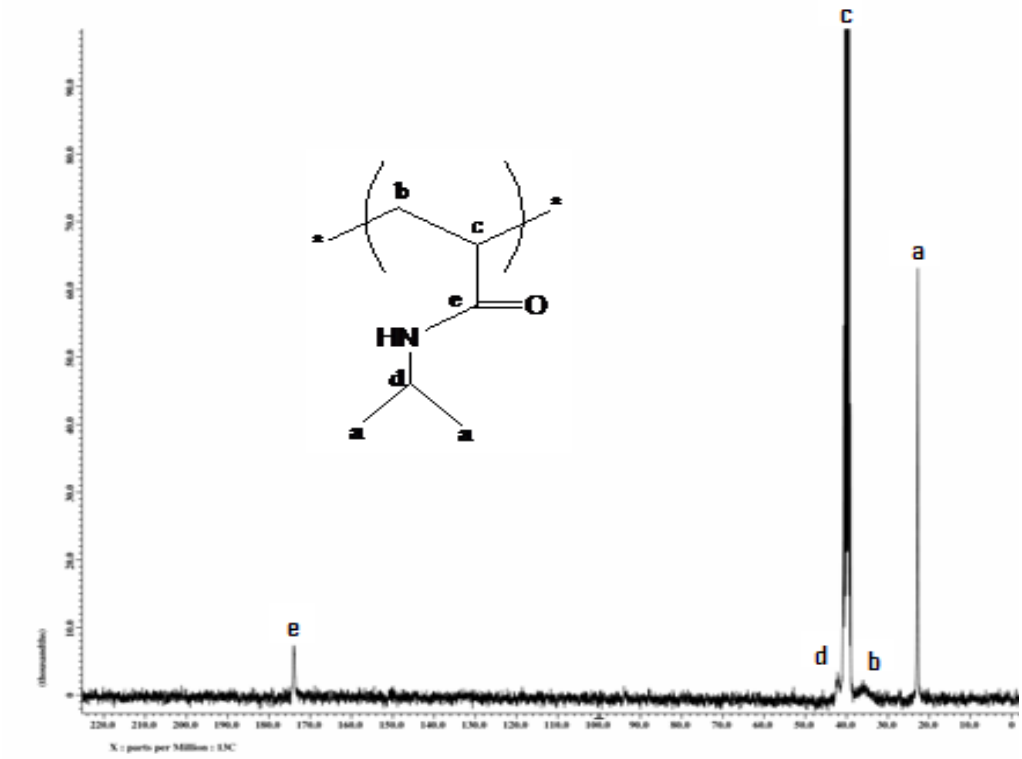

Figure 3.7. ^{13}C NMR of N-isopropylacrylamide (NIPA).

In the ^{13}C NMR of NIPA-AAm (Figure 3.8) we observed the backbone carbons at 35.90 (b) and a multiplet between 39 to 40.8 ppm (c). The isopropyl carbon in NIPA was shown at 42.21 (d), and the carbon of methyl groups in NIPA was observed at 22.85 (a). The peaks at 173.95 and 177 ppm are from the carbonyl groups of NIPA and AAm, respectively. As shown in Table 1, the composition of the copolymer

approximately followed those compounds in the feed, implying that polymerization was occurring as expected.

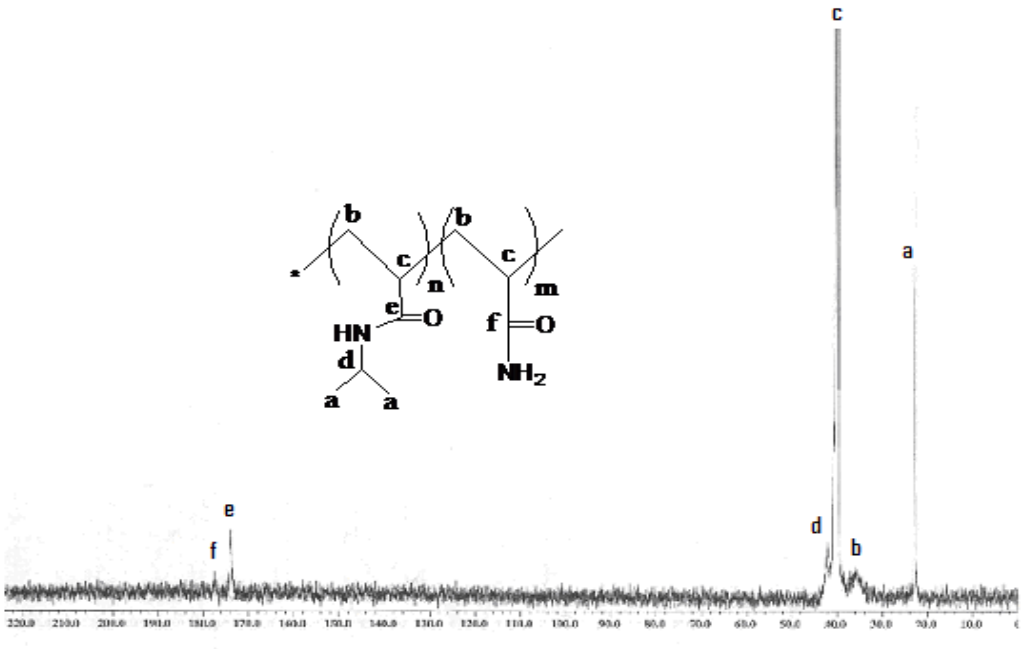

Figure 3.8. ^{13}C NMR of N-isopropylacrylamide-co-acrylamide (NIPA-AAm)

Table 3.1. Monomer ratio in the feed and in the copolymer predicted by NMR.

	In the feed	**In the copolymer**
	x 10^{-3} mole (% mole)	% mole
NIPA	12.06 (83 %)	82.7 %
AAm	2.47 (17 %)	17.3 %

The ^{13}C NMR of NIPA-AAm-AH nanoparticles (Figure 3.9) identified the carbonyl group of AAm at 177.98 ppm and the carbonyl group of NIPA at 173.96 ppm. The composition of the NIPA-AAm-AH was also determined by using ^{13}C NMR and titration. As shown in Table 2, the composition of the NIPA-AAm-AH was close to the compound molar percentage in the feed. This implies that polymerization was as expected.

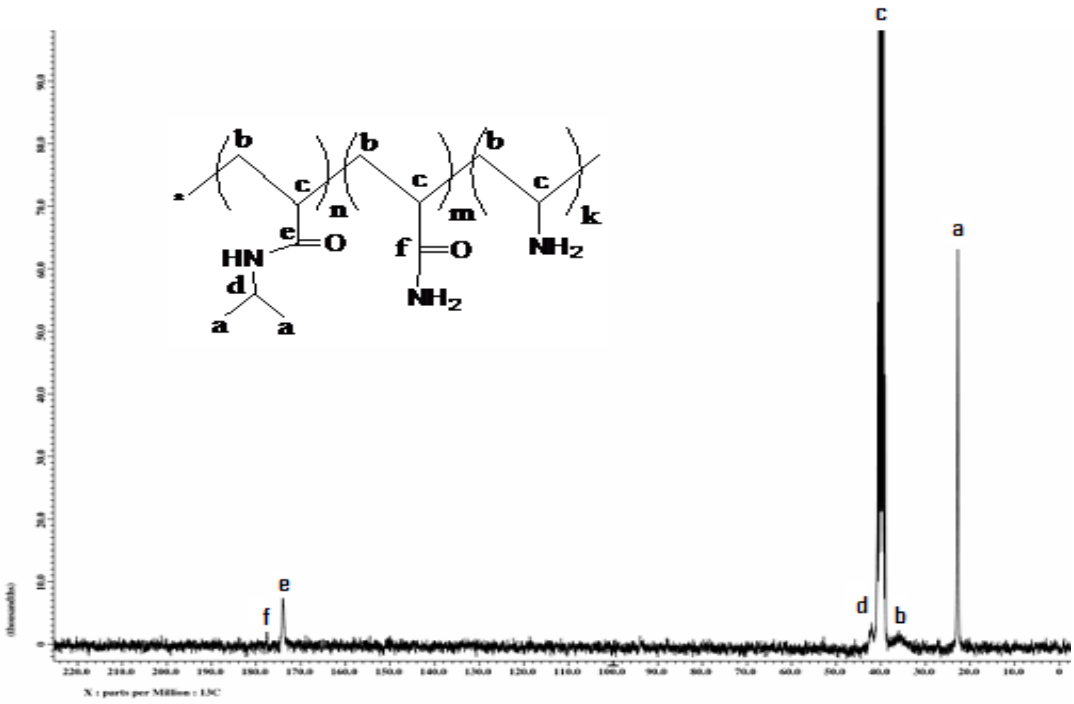

Figure 3.9. ^{13}C NMR of N-isopropylacrylamide-acrylamide-allylamine (NIPA-AAm-AH)

Table 3.2. Monomer ratio in the feed and in the NIPA-AAm-AH predicted by NMR and titration.

	In the feed	**In the NIPA-AAm-AH**
	x 10^{-3} mole (% mole)	% mole
NIPA	9.79 (58 %)	61.9 %
AAm	2.0 (11.9 %)	9.8 %
AH	5.05 (30 %)	28.3 %

3.1.4 LCST determination

To determine the temperature at which the phase transition occurs in the nanoparticles, UV-Vis spectrophotometer was used. As shown in Figure 3.10, the LCST of NIPA nanoparticles was 34°C. The rate at which the transition occurs slowly changes around 32°C, and then the intensity sharply decreases at 34°C. On the other hand, the phase transition of NIPA-AAm and NIPA-AAm-AH nanoparticles occurs sharply at 39°C and 40°C, respectively. In addition to the LCST measurements, the phase transition of the nanoparticles can easily be seen when the solution goes from clear to cloudy at each specific LCST, as shown in Figure 3.11.

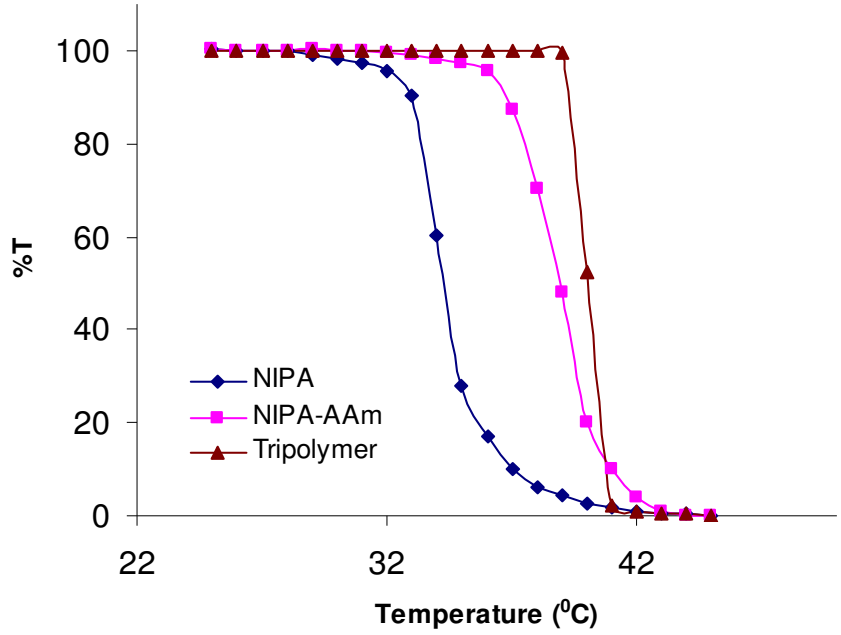

Figure 3.10. LCST of nanoparticles measured by UV-Vis. spectrophotometer. The rising temperature ratio is 1^0C/min.

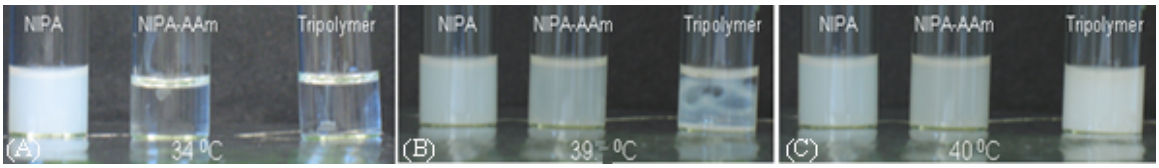

Figure 3.11. Photographs of NIPA, NIPA-AAm, and NIPA-AAm-AH nanoparticles at different temperatures. The nanoparticles were placed (A) at 34^0C (B) at 39^0C, and (C) at 40^0C. A color change was observed when the phase transition occurred.

3.1.5 Conjugation

In order to increase the circulation half life of the synthesized nanoparticles, fluorescent PEG was utilized to conjugate this stability element on the nanoparticle surface. Fluorescent PEG was conjugated to nanoparticles using carbodiimide chemistry, as shown in Figure 3.12 a. An enhanced optical fluorescence microscope

was used to assess the attachment of fluorescent PEG to nanoparticles. As Figure 3.12b indicates, bright green color was observed in our NIPA-AAm-AH nanoparticles, whereas this fluorescence was not seen in nanoparticles where the coupling agent was not used. These results indicate that our NIPA-AAm-AH nanoparticles have the capability for conjugation with other biomolecules such as PEG.

(a)

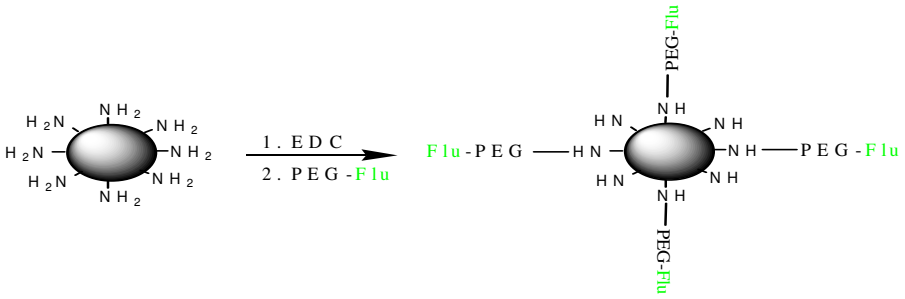

(b)

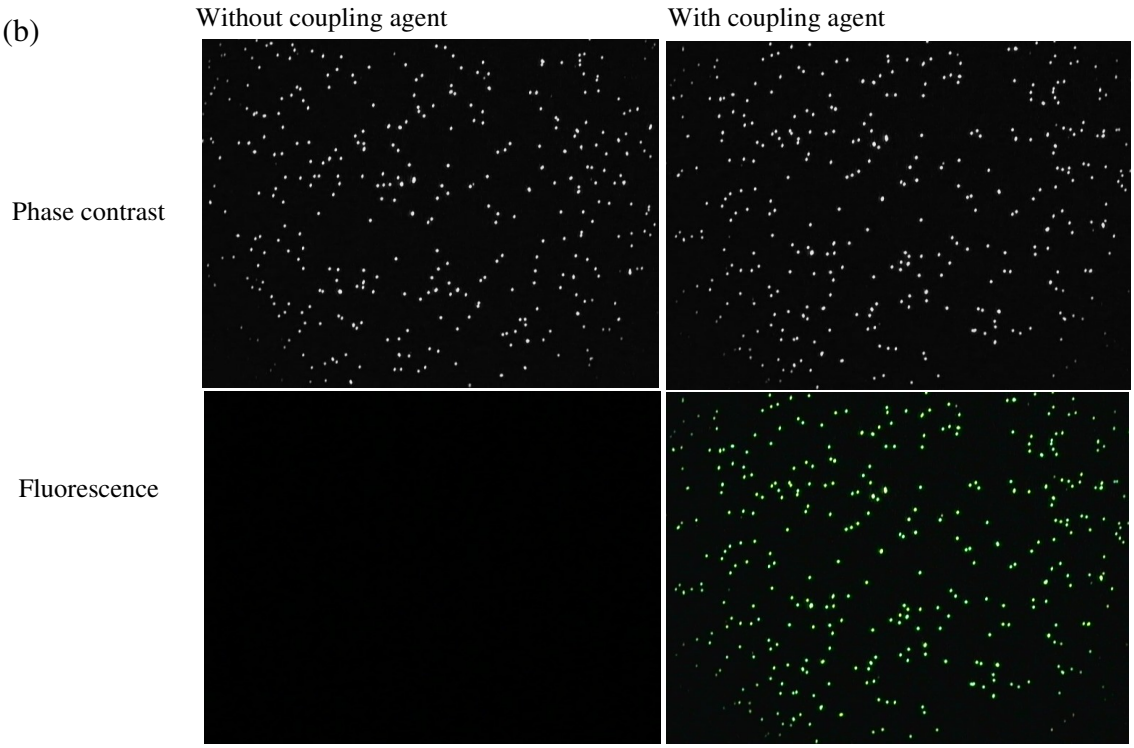

Figure 3.12. Conjugation of nanoparticles to fluorescent PEG. (a) Schematic diagram of the conjugation reaction of nanoparticles with Fluor-PEG. (b) Fluorescent and phase contrast microscopy (cytoviva) image of nanoparticles treated without and with coupling agent.

In order to assess the capability of our NIPA-AAm-AH nanoparticle for other bioconjugation, IgG-TR was utilized as a conjugate for the nanoparticles. IgG-TR was conjugated to nanoparticles again using the carbodiimide chemistry, as shown in Figure 3.13a. As Figure 3.13b indicates, a bright red color was observed in our NIPA-AAm-AH nanoparticles, whereas this fluorescence was not seen in NIPA-AAm nanoparticles (control). These results indicate that our NIPA-AAm-AH nanoparticles have amine functional groups available which can be utilized for conjugation of various biomolecules including antibodies.

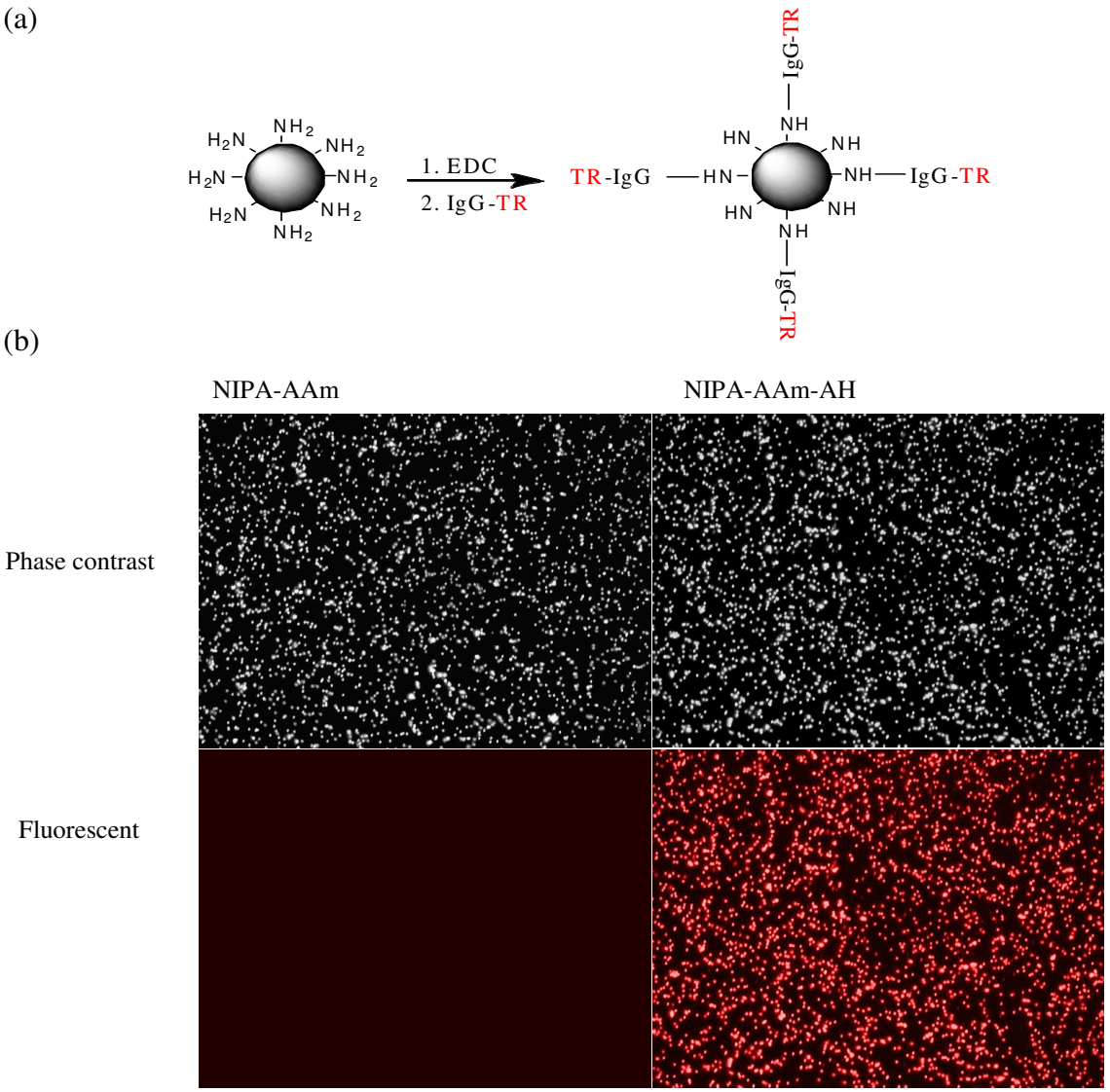

Figure 3.13. Conjugation of nanoparticles to IgG-TR (bovine anti-rabbit IgG-Texas Red). (a) Schematic diagram of the conjugation reaction of NIPA-AAm-AH nanoparticles with IgG-TR. (b) Fluorescent and phase contrast microscopy (cytoviva) image of NIPA-AAm and NIPA-AAm-AH nanoparticles reacted with fluorescent IgG.

In order to further image the nanoparticles *in vivo* (for future animal studies), NIPA-AAm-AH nanoparticles were conjugated to QDs. To assess the attachment of QDs, two methods, TEM and enhanced optical imaging, were used. Transmission

electron microscopy (TEM) was used in order to observe the QDs conjugated to the NIPA-AAm-AH nanoparticles. As shown in Figure 3.14, the black dots which represent the QDs are on the gray background (NIPA-AAm-AH nanoparticles), and the average size of the nanoparticles is approximately 100 nm. Nanoparticles with smaller sizes are also visible here which the overall size is consistent with the size distribution indicated in Figure 3.2.

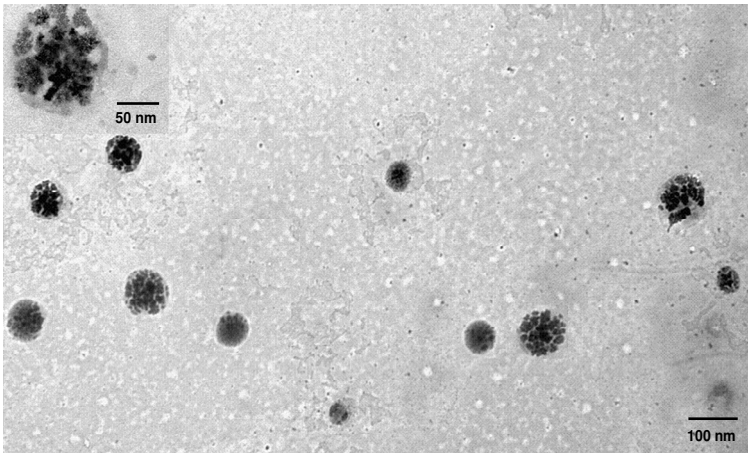

Figure 3.14. TEM image of QDs attached to NIPA-AAm-AH nanoparticles.

Using a color enhanced optical microscope, the color of the QDs is yellow at the absence of coupling agents or NIPA-AAm-AH (Figure 3.15). However, the color turns to blue with the presence of both coupling agents and NIPA-AAm-AH. These results indicate that the conjugation has occurred and the energy level of the QDs has changed due to their attachment onto NIPA-AAm-AH nanoparticles.

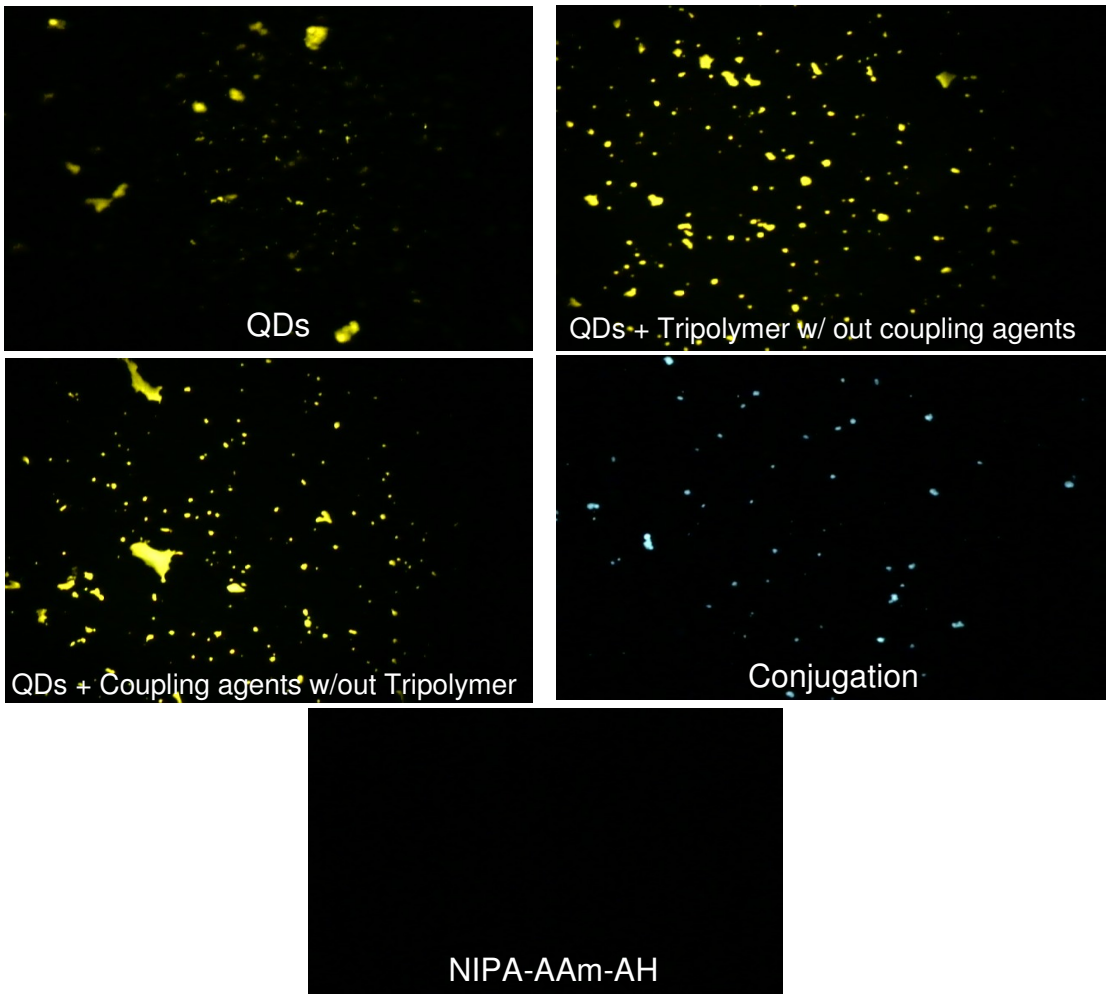

Figure 3.15. Quantum Dot conjugation to NIPA-AAm-AH. Fluorescence image of the conjugation in the presence and absence of the coupling agent and NIPA-AAm-AH.

3.1.6 Nanoparticle cytotoxicity

In order to begin investigation of the biocompatibility of our NIPA-AAm-AH temperature-sensitive nanoparticles, the cell viability of 3T3 fibroblast cells was studied when these cells were incubated with synthesized nanoparticles at various concentrations (16, 31, 62, 125, 250, and 500 µg/ml). The cell viability was determined

using MTS assays at different time points (24 and 48 hours). As shown in Figure 3.16, there is no significant difference in the cell viability between control cells and cells exposed to nanoparticles, especially at concentrations less than 250 µg/ml. For all concentrations, the loss of cell viability is less than 15% at both time points. This indicates that the synthesized nanoparticles exhibit low cytotoxicity, partially satisfying one of the major criteria required for a new drug delivery system.

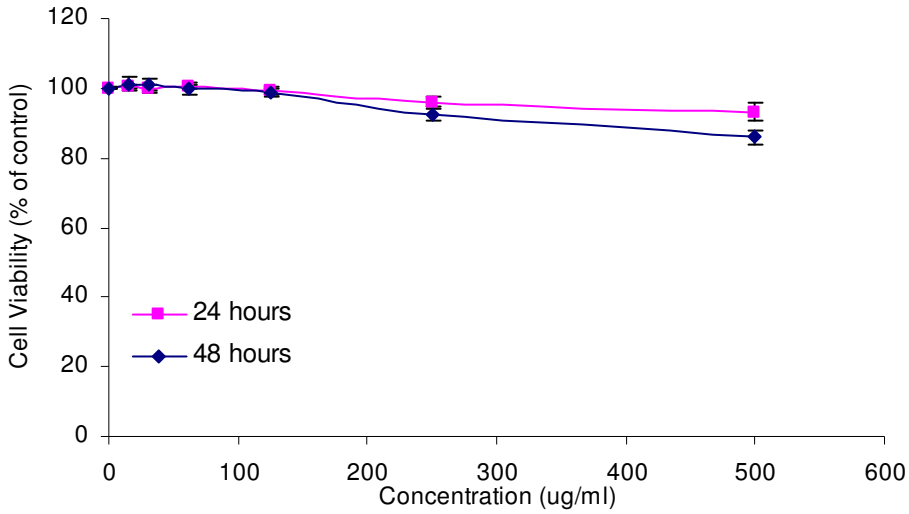

Figure 3.16. Cell viability of 3T3 fibroblast cells after 24 and 48 hours incubation with NIPA-AAm-AH nanoparticles at various concentrations. The cell viability was assessed using MTS assays. Cells without exposure to nanoparticles served as controls.

3.1.7 Drug release

The loading efficiency of BSA was determined according to the formula described earlier in the methods section. Protein assays indicated that approximately 78% of the incubated BSA was loaded into the NIPA-AAm-AH nanoparticles. There was a significant difference in the early release rate (Figure 3.17a) that continued

throughout the measurement period (Figure 3.17b). The cumulative percent release of BSA at 41°C was significantly higher than at 4°C. This indicates that the NIPA-AAm-AH nanoparticles exhibit temperature sensitivity, whereby the nanoparticles collapse upon themselves and squeeze the drug out at the LCST. After 4 hours, the cumulative percent release of BSA is only 2% at 4°C whereas at 41°C it is 7% (Figure 3.17a). Furthermore, after 300 hours, 50% of the encapsulated BSA was released at 41°C whereas at 4°C approximately 30% was released (Figure 3.17b). While higher release in the early period is desirable, it is evident from the graph that the slope is much higher at 41°C compared to 4°C, suggesting that over longer periods of time, even more BSA would be released. In addition, the low BSA release may be due to the fact that BSA interacts with the polymer itself, hindering its release, as shown in previous studies by Wu and coworkers.[110]

(a)

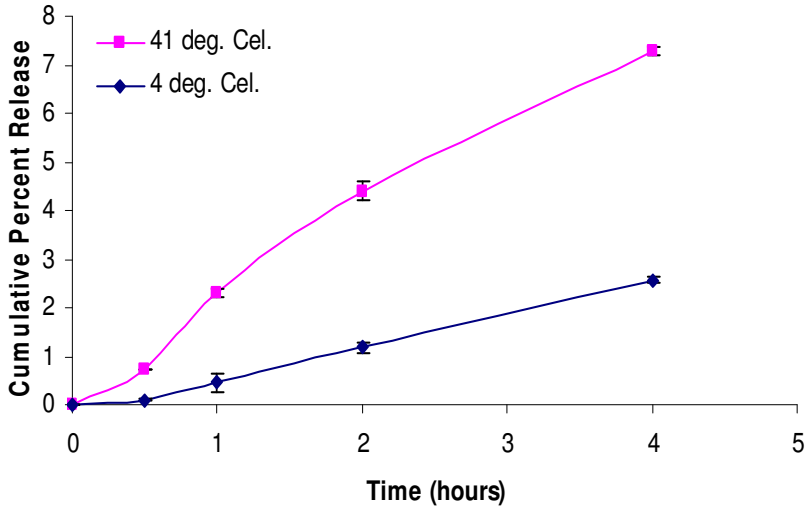

(b)

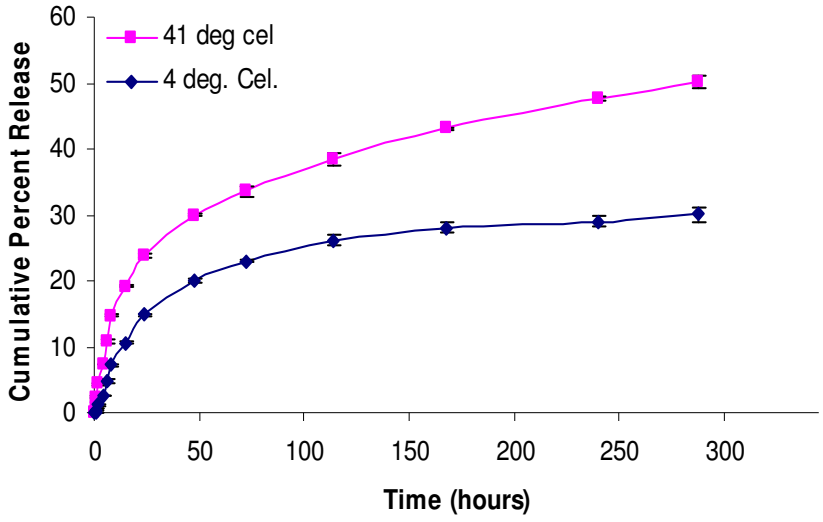

Figure 3.17. In vitro release profile of BSA at (◆) 4^0C and (■) 41^0C. (a) Cumulative percent release of BSA over the first 4 hours. (b) Cumulative percent release of BSA over 300 hours.

Results from the DOX release studies indicated that approximately 66% of the incubated DOX was loaded into the NIPA-AAm-AH nanoparticles. In addition, the cumulative percent release of DOX at 41^0C was significantly higher than that at 37°C and at 4°C (Figure 3.18). This further supports the evidence that the NIPA-AAm-AH nanoparticles are temperature sensitive, as the nanoparticles collapse upon themselves and squeeze the drug out at its LCST. After 72 hours, 84% of the encapsulated DOX was released at 41°C, whereas at 37°C and 4°C approximately 31% and 38%, respectively, were released. The release profile of the DOX over the first 30 minutes is also shown as an insert in Figure 3.18. After 30 minutes, the cumulative percent release of DOX is only 0.045% and 0.27% at 4°C and 37°C, respectively, whereas at 41°C it is 2.5%. The observed burst release of drugs at this short period of time is useful for applications such as cancer treatment where aggressive drug release needed to treat the disease.

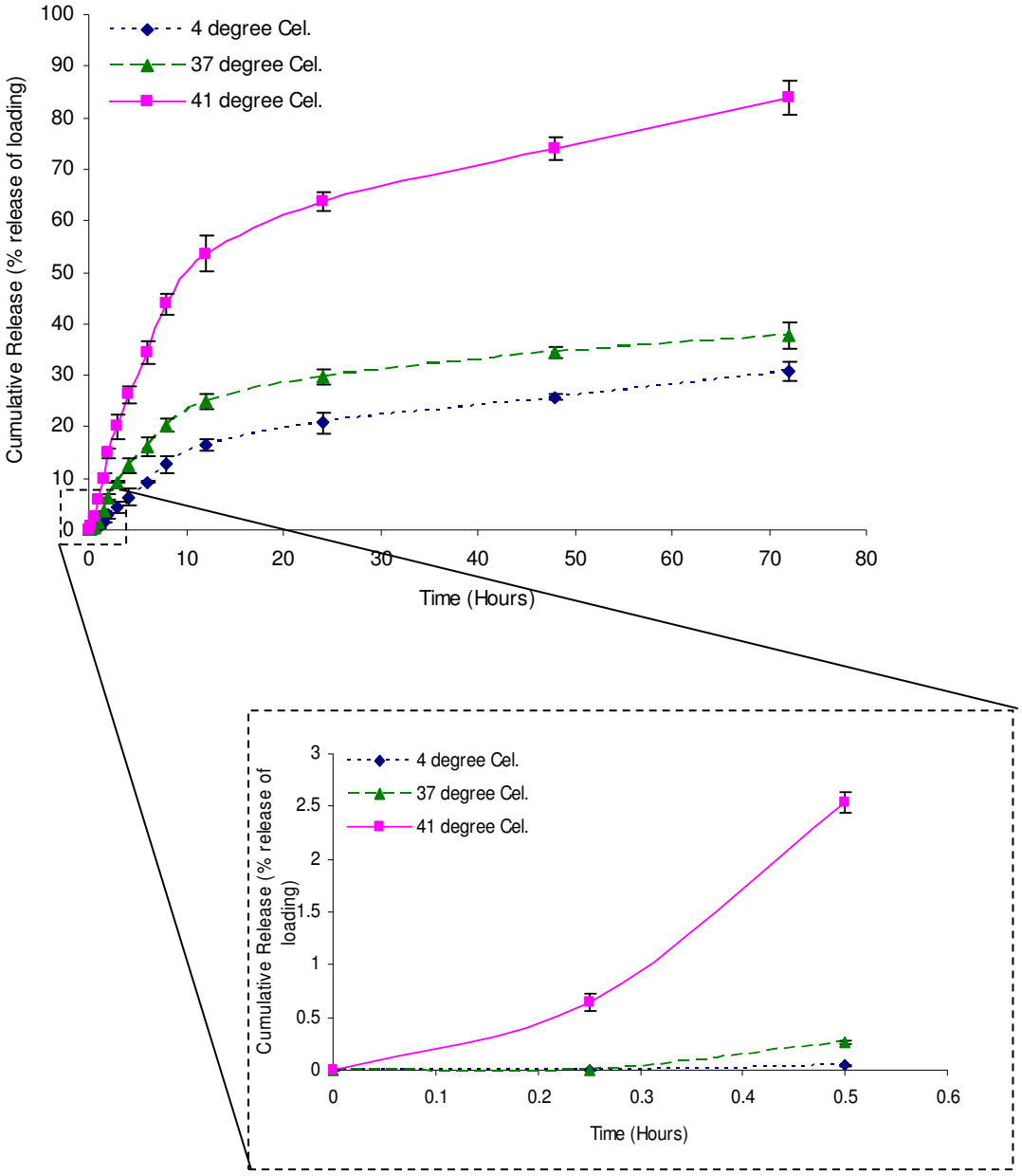

Figure 3.18. In vitro release profile of DOX at (◆) 4^0C, (▲) 37^0C, and (■) 41^0C . Cumulative percent release of DOX over 72 hours. The insert is the cumulative percent release of BSA over 30 minutes.

3.2 Characterization of magnetic nanogels

After designing and characterizing the optimum coating for the MNPs, a synthetic method was chosen in order to attach the nanogels onto the surface of MNPs which were described in the method section. In the following sections the characterization of these polymer coated MNPs will be discussed.

3.2.1 Transmission electron microscopy (TEM)

The average size of the NIPA coated MNPs and their derivatives were analyzed using TEM and SEM. The size of the MNPs was in the range of 10 nm in diameter as shown in Figures 3.19a. The electron diffraction pattern in Figure 3.19 (a) consists of continuous rings consistent with the small size and large number of the MNPs. The first four diffraction rings had d-spacings of 4.771, 2.943, 2.511, 2.062 Å and were indexed to correspond to the (111), (220), (311), and (400) planes, respectively, of the Fe_2O_3 structure. The average size of MNPs coated with the silane coupling agent, as determined by TEM, was around 40 nm, Figure 3.19b. The larger size of the silane-coated particles is attributed to agglomeration of a few MNPs during the encapsulation process. Single crystal nanoparticles of that scale usually exhibit crystallographic facets to reduce their surface energy. It is possible that facets of the same orientation were merged together to produce a larger size particle. In that case, the electron diffraction pattern, Figure 3.19 (b), which was taken from a couple of silane-coated particles, consists of several spots of the same crystal structure as that of Figure 3.19a**.** This is consistent with the argument that the larger, silane-enclosed particles are composed of a

merged 10 nm MNPs. NIPA silane-coated MNPs were about 100 nm in size, as shown in Figures 3.19c. Furthermore, Figure 3.19c clearly indicates the formation of silane-coated MNPs with uniform shells. A close examination of the TEM image, inset in Figure 3.19c, shows that each dark core magnetic nanoparticle was surrounded by a thin (~2 nm), lighter shell from silane and a thicker, uniform NIPA shell. It is important to note that the NIPA shell formed around the individual large silane-coated particle rather than around an aggregation of silane-coated particles. This is markedly different than the results observed with other encapsulation methods such as miniemulsion.[53] This provides evidence that each individual silane-coated magnetic nanoparticle serves as a template site for polymerization of NIPA onto MNPs. SEM analysis also confirmed the results for the shapes and sizes of the synthesized nanoparticles (data is not shown).

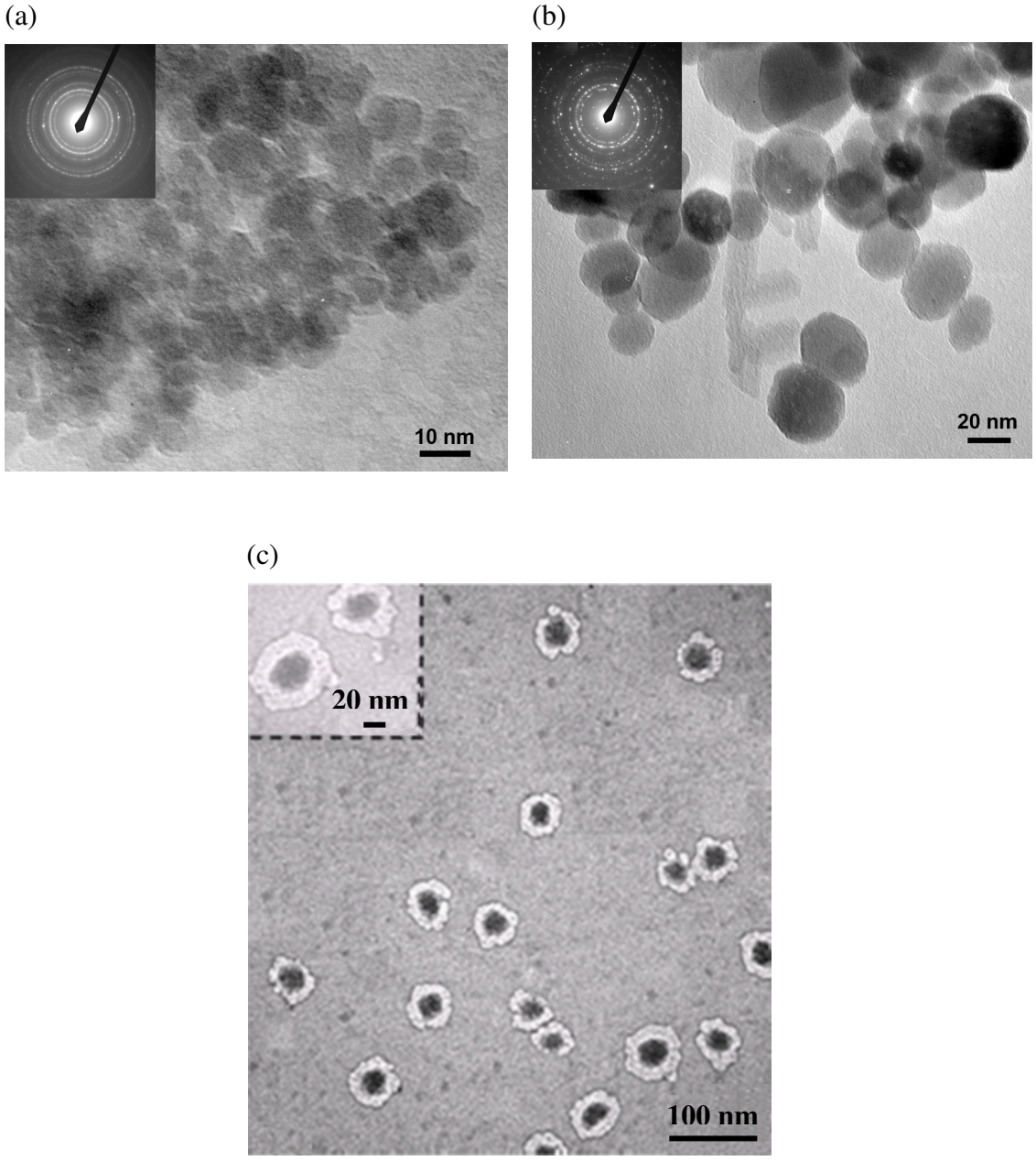

Figure 3.19. Transmission electron micrograph of coated and uncoated magnetites: (a) as-synthesized MNPs (inset is the diffraction pattern); (b) Silane-coated MNPs (inset is the diffraction pattern); (c) NIPA-coated MNPs (inset is a higher magnification image).

The same method was used in order to coat MNPs with NIPA-AAm-AH. The synthesized NIPA-AAm-AH coated MNPs are approximately 100 nm in diameter, as

shown in Figure 3.20. A closer examination of the TEM image (inset in figure 3.20) shows that there is one MNP (approximately 10 nm) in the center with NIPA-AAm-AH coat surrounding it. In comparison to NIPA coated MNPs, there was less number of MNPs in the core. It is possible that use of a mechanical stirrer, with higher mixing capability, instead of a magnetic stirrer caused less aggregation of MNPs in NIPA-AAm-AH coated MNPs. This might also be due to the electrostatic charge repulsion from the amine group of allylamine in the NIPA-AAm-AH coat. In any event, encapsulation of MNPs with NIPA-AAm-AH not only provides functional groups on the nanoparticles for bioconjugation but also prevents the aggregation of the nanoparticles.

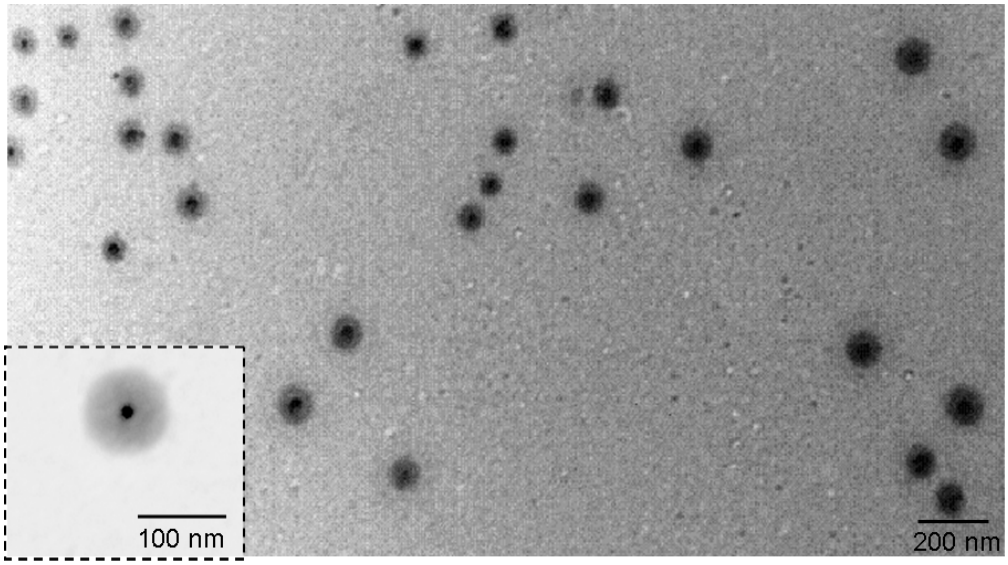

Figure 3.20. Transmission electron micrograph of NIPA-AAm-AH coated MNPs (inset is a higher magnification image).

3.2.2 Fourier transform infrared spectroscopy (FTIR)

Our FTIR analysis indicated Fe-O of the NIPA-AAm-AH coated MNPs at 590.3 cm^{-1} and 636.2 cm^{-1}, Figure 3.21. The stretching vibration appearing in the range of 2900-3100 cm^{-1} corresponds to C-H bands. In addition, the IR peak at 3423 cm^{-1} corresponds to a stretching vibration of primary amine group in the NIPA-AAm-AH coated MNPs. The peak from the secondary amine group is also observed around 3308.4 cm^{-1}. Furthermore, the carbonyl groups of NIPA and AAm are observed at 1655 cm^{-1}. These peaks indicate that the NIPA-AAm-AH coated MNPs consist of functional groups corresponding to their constituent monomers as shown in Figure 3.21.

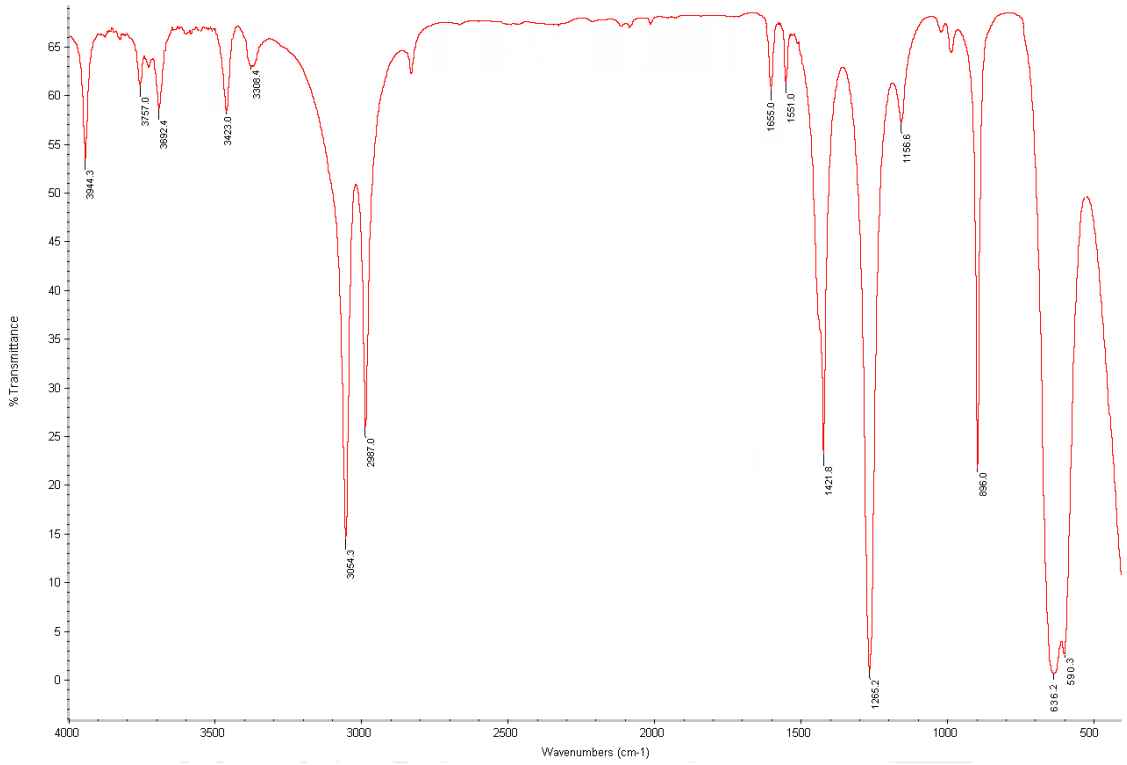

Figure 3.21. Chemical composition analysis of the NIPA-AAm-AH coated magnetic nanoparticle. FTIR spectrum of NIPA-AAm-AH coated magnetic nanoparticle at room temperature (25^0C).

3.2.3 XPS studies

XPS was used to determine the composition and bonding structures of the synthesized nanoparticles. Figure 3.22 presents the general XPS spectra of the (a) Fe_2O_3 particles, (b) silane-coated Fe_2O_3 particles, and (c) NIPA-coated Fe_2O_3 particles, respectively. As shown, strong O 1*s* and Fe 2*p* peaks at 530 eV and 711.5 eV, respectively, are present in the Fe_2O_3 particle spectrum. In addition, a weak C 1s peak at 285.9 eV can also be seen. The intensity of this peak was significantly reduced by increasing sputtering time, indicating that this peak may originate from contamination. Three peaks corresponding to C 1s, O 1s, and Fe 2p electrons can be seen in the spectrum for the silane-coated Fe_2O_3 particles. The intensity of the C 1s peak is slightly higher and that of the Fe 2p peak lower in the spectrum for the silane-coated Fe_2O_3 particles as compared with the spectrum for the Fe_2O_3 particles. This implies that the Fe_2O_3 particles are coated with a silane layer. At the same time, a very weak Si 2p peak at a binding energy of 101.86 eV could be distinguished from the background, indicating the existence of Si in the coating. In the spectrum of NIPA-coated Fe_2O_3 particles, two strong C 1s and O 1s peaks appear. After careful inspection, three weak peaks originating from Si 2p, N 1s, and Fe 2p could be distinguished. The calculated composition of the elements in the NIPA-coated magnetic particles is 4.6% for Si, 21.1% for O, 70.9% for C, 3% for Fe, and 0.1% for N. The low content of the Si and Fe in this sample indicates that the Fe_2O_3 particles might be completely covered with a relatively thick NIPA layer.

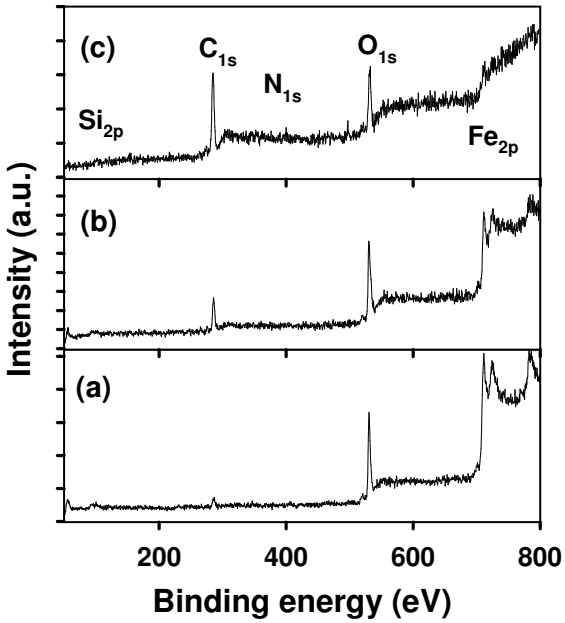

Figure 3.22. XPS spectra from the (a) Fe_2O_3 particles, (b) silane coated Fe_2O_3 particles, and (c) NIPA-coated Fe_2O_3 particles.

In order to obtain detailed information about the chemical bonds for the NIPA coated particles, high resolution scans were performed for the various elements involved. Figure 3.23 (a) exhibits the N 1s spectrum of the NIPA-coated particles. Due to the low intensity, the N 1s spectrum of the Fe_2O_3 particles is also included in the figure as a reference. The results clearly show the presence of nitrogen in the NIPA-coated particles. This peak can be deconvolved with a Gaussian peak at 400.33 eV, which is close to the binding energy of N 1s in imine- or aromatic-type N=C bonding, 400.6 eV.[111, 112] This indicates that the N 1s peak in the spectrum originates from NIPA.

Figure 3.23 (b) depicts the Si 2p high resolution spectrum obtained from the NIPA-coated particles. The Si 2p peak is at about 102 eV, which is lower than the binding energy of Si 2p in the Si-O bond (103.3eV), but higher than that in the Si-C bond (101.2 eV). This indicates the existence of both Si-C and Si-O bonds in the particles. In a previous study about the oxidation behavior of SiC, Jernigan et al also found that the Si 2p peak shifts to a higher binding energy due to the formation of Si-O bonds.[113] The Si 2p peak could be deconvolved using the two chemical states of Si at 101.2 and 103.3 eV. The relative intensity ratio for the two peaks is about 1, indicating that each Si atom in the particles is bonded with both O and C and suggesting that only a Si atom monolayer covers the Fe_2O_3 particles.

Figure 3.23 (c) shows the Fe 2p1/2 high resolution spectrum from the NIPA-coated particles. The peak can be deconvoluted with one Gaussian peak at 711.7 eV, which is close to the binding energy of Fe 2p1/2 in Fe(OOH) (711.3 eV) and Fe_2O_3 (710.9eV). The peak is broad, implying the existence of both Fe(OOH) and Fe_2O_3 phases in the synthesized Fe_2O_3 particles.

Due to the existence of Fe-O, C=O, and Si-O bonding, the O 1s spectrum should be fitted with three peaks corresponding to 529.6, 531.9, and 532.9 eV[114] as shown in Figure 3.23 (d). The relatively content of the Fe-O, C=O, and Si-O bonds is calculated to be 24.5%, 27.9%, and 47.6%, respectively.

On the basis of the above analysis, there should exist C-Si, C-N, and C=O bonds in the NIPA coated magnetic particles. According to the chemical molecular formula of NIPA, there should also be CH_n/C-C bonds. Therefore, the C 1s spectrum should be fitted with 3 peaks at 282.7, 284.8, 286, 288.4 eV, corresponding to the C-Si, CH_n/C-C, C-N, and C=O bonds, respectively, as shown in Figure 3.23(e). The relatively content for different bonding is calculated to be 3.4%, 90.8%, 2.0%, and 3.8%, respectively. The high content of the CH_n/C-C bond indicates that 90% of C in the spectra originates from NIPA.

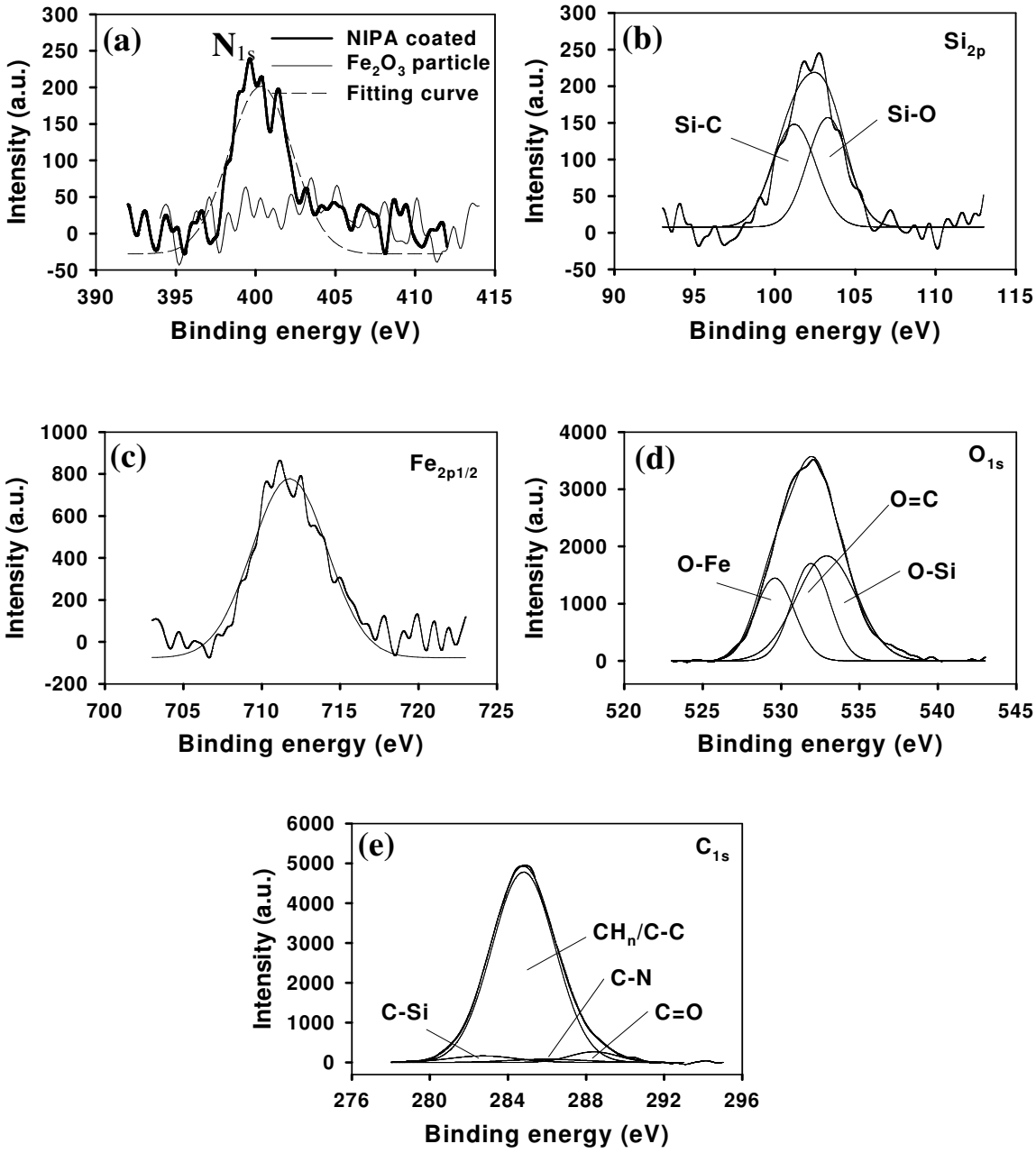

Figure 3.23. High resolution deconvoluted spectra from (a) N 1*s*, (b)Si 2*p*, (c) Fe $2p_{1/2}$, (d) O 1*s*, and (e) C 1*s* of the NIPA-coated particles.

High resolution scans of the NIPA-AAm-AH coated MNPs were performed for the various elements involved in order to obtain detailed information of the chemical bonds. Figure 3.24(a) shows the N 1s spectrum of the NIPA-AAm-AH coated MNPs. The result clearly indicates the presence of different amine functional groups in the NIPA-AAm-AH coated MNPs. The peak at 399.6 eV was deconvolved with a Gaussian peak for amine, C-N, and amide bond at 399.33, 399.52, and 399.7 eV, respectively, which is close to the binding energy reported earlier.[115-117] These results indicate that N 1s mostly present as C-N. Table 3.3 provides the various percentage of the three chemical states.

The Si 2p high resolution spectrum obtained from the NIPA-AAm-AH coated nanoparticles is shown in Figure 3.24(b). The Si 2p peak clearly shows two peaks, and it is composed of Si-O bond (100.4 eV) and Si-C bond (101.8 eV). This indicates the existence of both Si-C and Si-O bonds in the nanoparticle. Similar results were obtained in our previous study of the oxidation behavior of SiC.[118] The percentages of Si-O and Si-C are 74.8% and 25.2% (ratio of 3:1), indicating that each Si atom in the particles is bonded with three O and one C atoms.

Due to the thick coating of the NIPA-AAm-AH, the binding energy of Fe 2p1/2 was not observed (Figure 3.24 c). The absence of the Fe peak in coated MNPs has also been reported by Cao et al.[119]

Due to the existence of Fe-O, C=O, and Si-O bonding, the O 1s spectrum should be fitted with three peaks corresponding to 530.37, 532, and 532.18 eV as shown in Figure 3.24(d). These results are close to the binding energies reported earlier.[120-122] In comparison to O 1s spectrum of empty shell of NIPA-AAm-AH, the spectrum of our core-shell nanoparticles has shifted from 531.95 to 531.32 eV, respectively. This shift is due to presence of Fe-O and Si-O present in the NIPA-AAm-AH shell.

The C 1s high resolution spectrum obtained from the NIPA-AAm-AH coated nanoparticles shows a binding energy of 285.01 eV, Figure 3.24(e). The C 1s spectrum was fitted with four peaks at 284.7, 282.9, 286.04, 287.98 eV, corresponding to CH_n/C-C, C-Si, C-N, and C=O bonds, respectively, as shown in Figure 3.24(e). The relative content for the different C bonding states was calculated to be 69.93%, 2.76%, 18.5%, and 8.81%, respectively. The high content of the CH_n/C-C bond indicates that the majority of the C in the spectra originates from the polymer shell. Table 3.3 illustrates the detail bonding energy, peak area, and percent composition for each group.

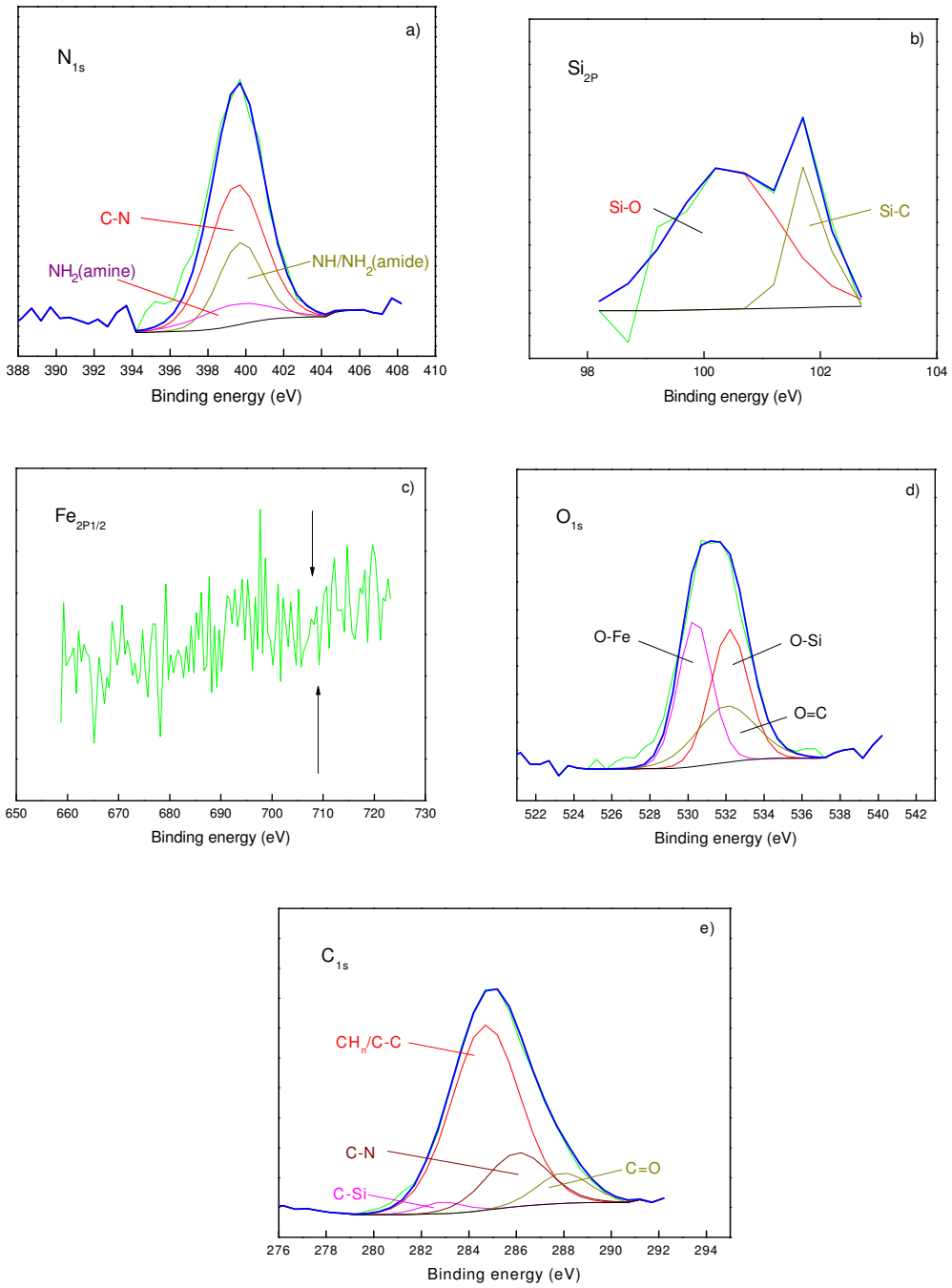

Figure 3.24. High resolution deconvoluted spectra from a) N 1s, b) Si 2p, c) Fe $2p_{1/2}$, d) O 1s, and e) C 1s of the NIPA-AAm-AH coated MNPs .

Table 3.3. The peak area in XPS spectra of NIPA-AAm-AH coated MNPs.

Element	Chemical State	Binding Energy (eV)	Peak Area	% Composition
	C-C/CHn	284.7	22727.9	69.9
C_{1s}	C-Si	282.9	896.5	2.8
	C-N	286.04	6014.4	18.5
	C=O	287.98	2863.8	8.8
	O-Fe	530.37	5900.4	37.4
O_{1s}	O=C	532	3997.8	25.3
	O-Si	532.18	5893.1	37.3
	NH_2 (amine)	399.33	1019	11.9
N_{1s}	C-N	399.52	5126.7	60
	NH/NH_2 (amide)	399.7	2398	28.1
Si2p	Si-C	101.8	49.1	25.2
	Si-O	100.2	145.8	74.8

3.2.4 SQUID measurements

Room temperature magnetization measurements of MNPs, silane coated MNPs and NIPA coated MNPs were determined using a SQUID-based magnetic property measurement system (Figure 3.25). The MNPs and the two layers can be classified as

soft ferromagnetic substances. These types of substances are classified by their low coercive force ($<10^2$ Oe), small remanent magnetic induction, and long and narrow hysteresis loop.[123] The measured values of magnetic properties of each type of nanoparticle are also shown in Table 3.4.

The saturation magnetization of the MNPs in this study (70.86 emu/g) was lower than that of bulk iron oxide (87.25 emu/g) but in good agreement with previous studies of iron oxide nanoparticles.[34] Similar effects have been well documented in the literature and attributed to non-linear spin configuration on the surface, resulting from the incomplete or different surroundings of the surface atoms.[124, 125] The saturation magnetization of MNPs was decreased by 43.2% after coating with silane and by 58.1% after coating with NIPA. Decreasing saturation magnetization was also noticeable when MNPs were placed in an external magnetic field where their respond time increased. This increase in response time has both advantages and disadvantages. By decreasing the saturation magnetization and increasing the response time, the aggregation of magnetic based nanoparticles (e.g. polymer MNPs) decreases; however, at the expense of having to use a higher external magnetic field to remotely control the nanoparticles. Similar to our results, the decrease in saturation magnetization has also been reported when MNPs were encapsulated with different polymers such as polystyrene via mini-emulsion processes.[126]

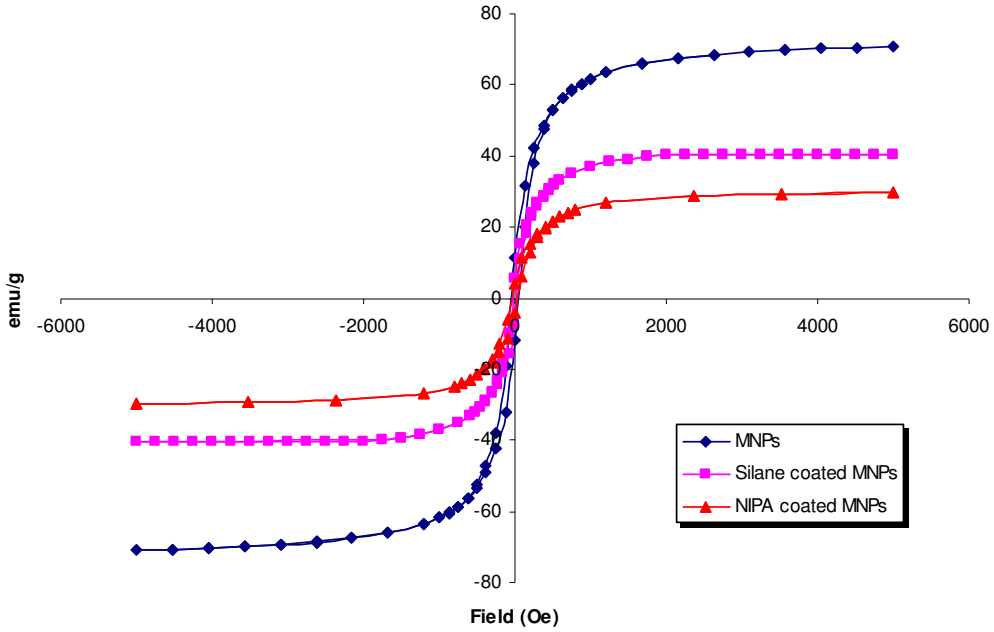

Figure 3.25. Magnetic hysteresis curves of MNPs, silane coated, and NIPA coated MNPs at room temperature.

Table 3.4. Magnetic properties of nanoparticles.

Sample	Saturation Magnetization (M_s) emu/g	Remanence (M_r/M_s)	Coercivity (H_c) Oe
MNPs	70.861	11.42	9.53
Silane coated MNPs	40.217	5.53	26.69
NIPA coated MNPs	29.714	4.28	42.42

The magnetic properties of the NIPA-AAm and NIPA-AAm-AH coated MNPs were also analyzed using a SQUID-based magnetic property measurement system. Our results indicated the saturation magnetization was approximately 29.02 emu/g, whereas the remanence and coercivity were 4.18 and 42.05 Oe, respectively (Figure 3.26). The saturation magnetization of MNPs was decreased by 59.8% after coating with NIPA-AAm-AH (Figure 3.26). The decrease in saturation magnetizations is possibly due to a "dead" surface layer on MNPs caused by the presence on the surface of various particles.[126, 127] This decrease was also observed when the NIPA-AAm-AH coated MNPs were placed in an external magnetic field where an increase in their response time was noticeable. Furthermore, the coercivity was increased where the MNPs were coated with silane, and NIPA-AAm-AH, which is due to size effects and an increase in separation distance of nanoparticles as a result of coating. As Figure 3.26 illustrates there are no significant differences in magnetization saturation of NIPA, NIPA-AAm, and NIPA-AAm-AH coated MNPs.

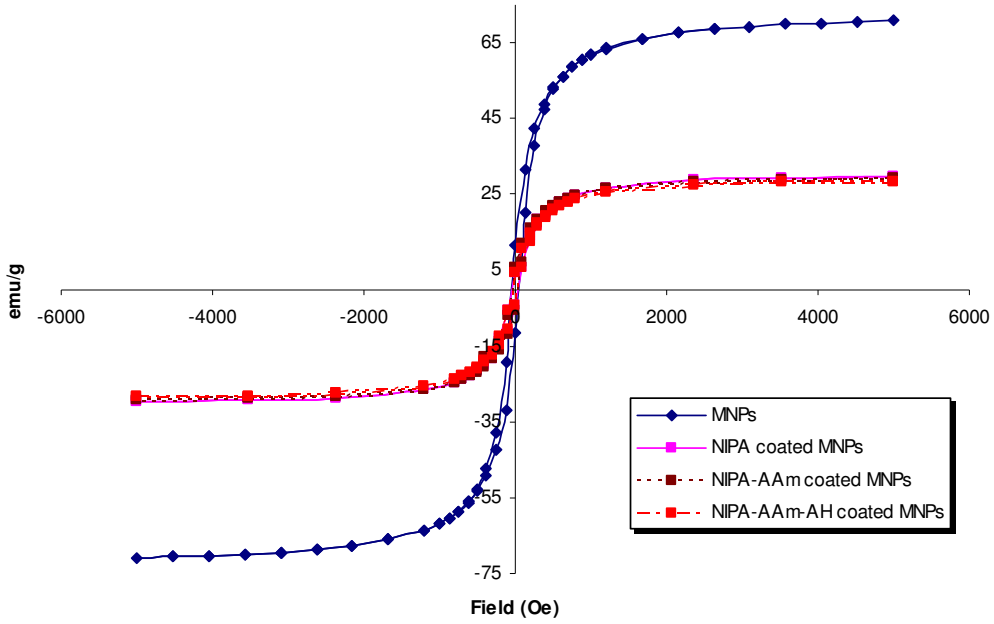

Figure 3.26. Magnetic hysteresis curves of NIPA-AAm and NIPA-AAm-AH coated MNPs at room temperature.

3.2.5 Drug release

The loading efficiency of BSA encapsulated NIPA-AAm-AH coated MNPs was determined according to the formula illustrated earlier in the methods section. Protein assay indicated that approximately 73% of the incubated BSA was loaded into the NIPA-AAm-AH coated MNPs. The release behavior of the nanoparticles was studied for approximately 300 hours in PBS (0.1 M, pH 7.4) at 4°C and 41°C. After 4 hours, the cumulative percent release of BSA is only 0.3% at 4°C whereas at 41°C is 6% as shown in Figure 3.27a. The percent cumulative release of BSA at 41°C was significantly higher than at 4°C (Figure 3.27b). This indicates that the NIPA-AAm-AH nanoparticle is a temperature sensitive polymer whereby, at its LCST, the nanoparticle collapses upon itself and "squeezes" the drug out. After 300 hours, 45% of the encapsulated BSA

was released at 41°C whereas at 4°C approximately 11% was released. The low BSA release may be due to BSA interaction with the polymer and itself as described earlier.[110]

(a)

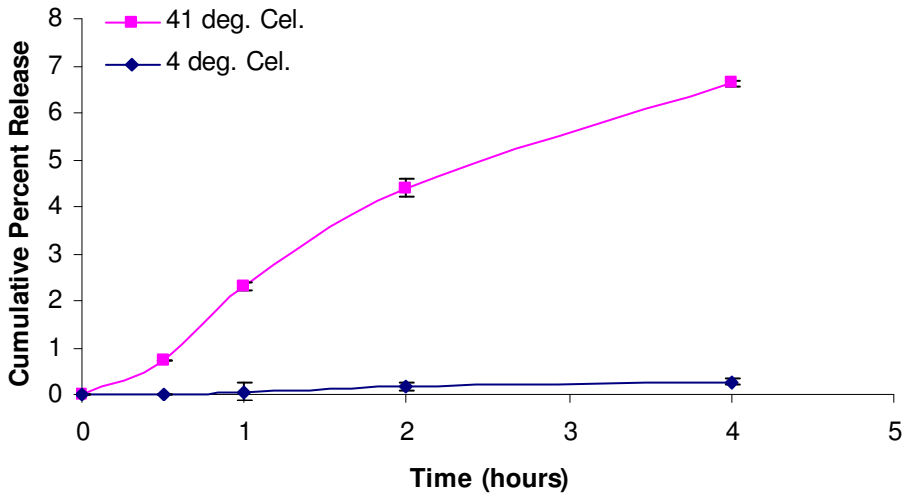

(b)

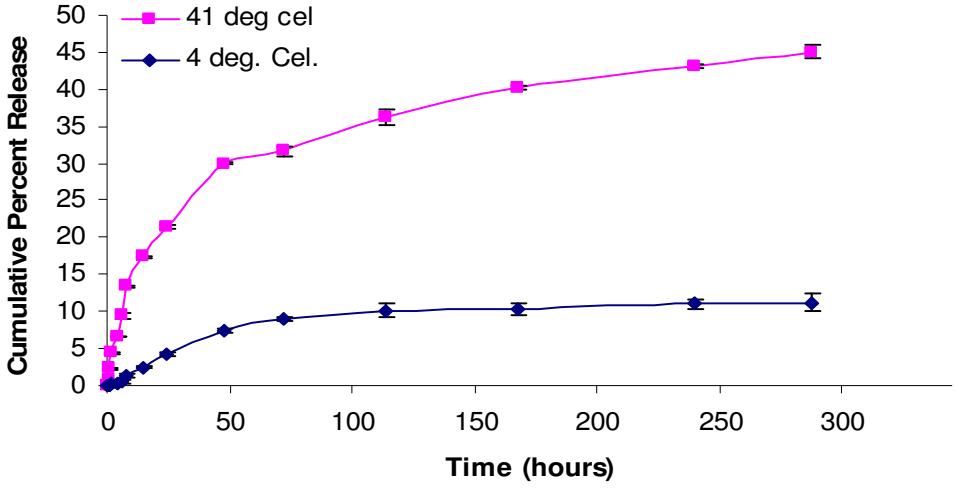

Figure 3.27. In vitro release profiles of BSA at (◆) 4^0C and (■) 41^0C . (a) Cumulative percent release of BSA over 4 hours. (b) Cumulative percent release of BSA over 300 hours.

After studying the release profile of a model protein, the release of the antitumor drug (i.e. doxorubicin) was investigated. The loading efficiency of DOX in NIPA-AAm-AH coated MNPs was approximately 72%. The release behavior of the nanoparticles was studied for approximately 72 hours in PBS (0.1 M, pH 7.4) at 4°C, 37°C and 41°C. The percent cumulative release of DOX at 41°C was significantly higher than at 4°C and 37°C (Figure 3.28). The drug release profiles at various temperatures indicate that the NIPA-AAm-AH coated MNPs could be used to load and release drugs in response to changes in temperatures. After 72 hours, 78% of the encapsulated DOX was released at 41°C whereas at 4°C and 37^0C approximately 26% and 43%, respectively, was released. The release profile of the DOX over first 30 minutes is also shown in Figure 3.28 (the insert). After 30 minutes, the cumulative percent release of DOX is only 0% and 0.046% at 4°C and 37°C, respectively, whereas at 41°C is 2.4%. The observed burst release of drug in this short period of time is useful for applications such as cancer treatment where aggressive measures need to be taken to treat the disease.

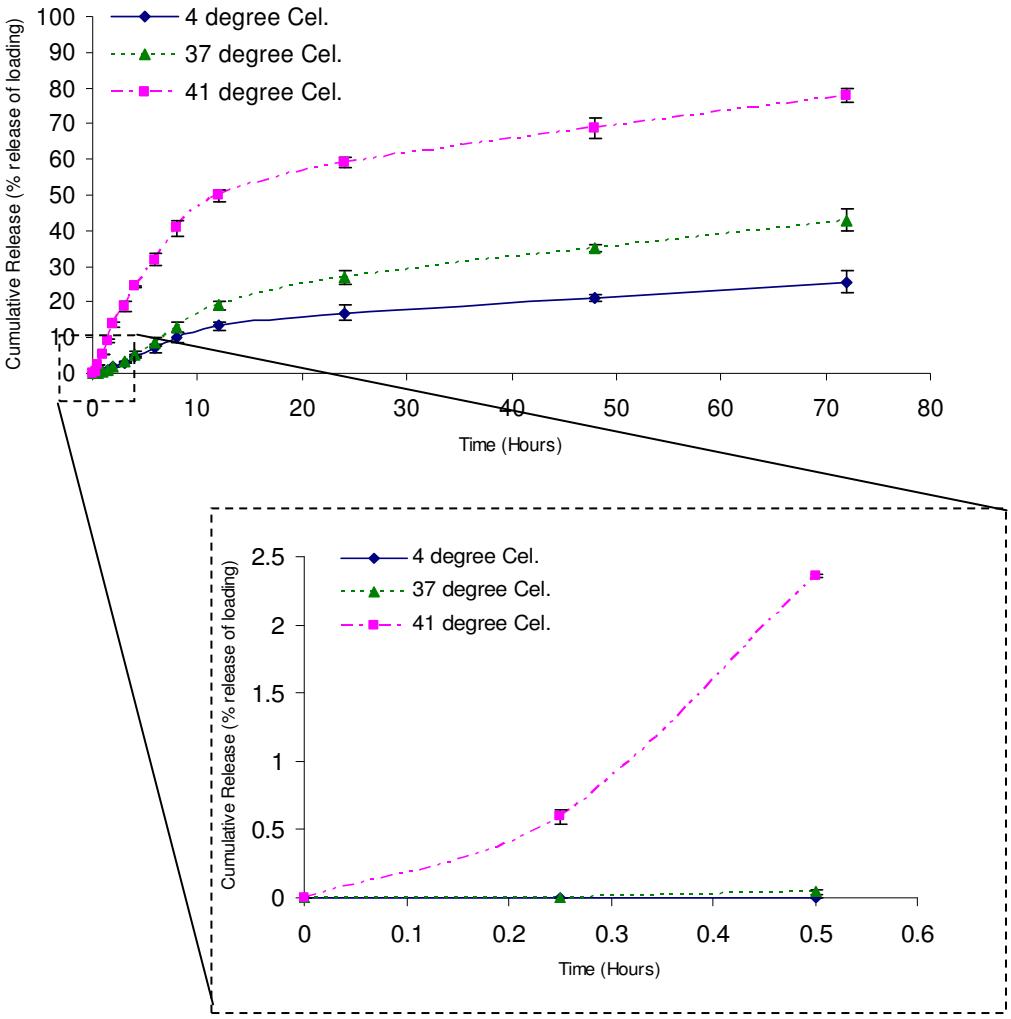

Figure 3.28. *In vitro* release profiles of DOX at (◆) 4^0C, (▲) 37^0C, and (■) 41^0C . Cumulative percent release of DOX over 72 hours. The insert is the cumulative percent release of DOX over 30 minutes.

3.2.6 Cellular cytotoxicity

LDH assays were used in order to investigate the biocompatibility of MNPs and NIPA-AAm-AH coated MNPs by qualifying the LDH released from the damaged 3T3

fibroblasts. Results from LDH Assays after 6 hours showed that the presence of MNPs at the concentration range of 16 to 31 µg/ml reduces the normal cells' viability by less than 20% (Figure 3.29). However, higher concentrations after 6 hours showed significant cytotoxicity as high as 62%. The presence of MNPs after 24 hours at a concentration of 31 µg/ml and higher showed significantly higher cytotoxicity (> 20%) compared to 6 hours incubation time. The cytotoxicity of MNPs after 24 hours was 68% at 500 µg/mL.

The NIPA-AAm-AH coated MNPs proved to be much less cytotoxic (Figure 3.29). The highest cytotoxicity observed at 500 µg/mL of NIPA-AAm-AH coated MNPs after 24 hours was less than 20%. This illustrates that NIPA-AAm-AH coated MNPs are much more compatible compared to MNPs, especially when nanoparticles are used at high concentrations.

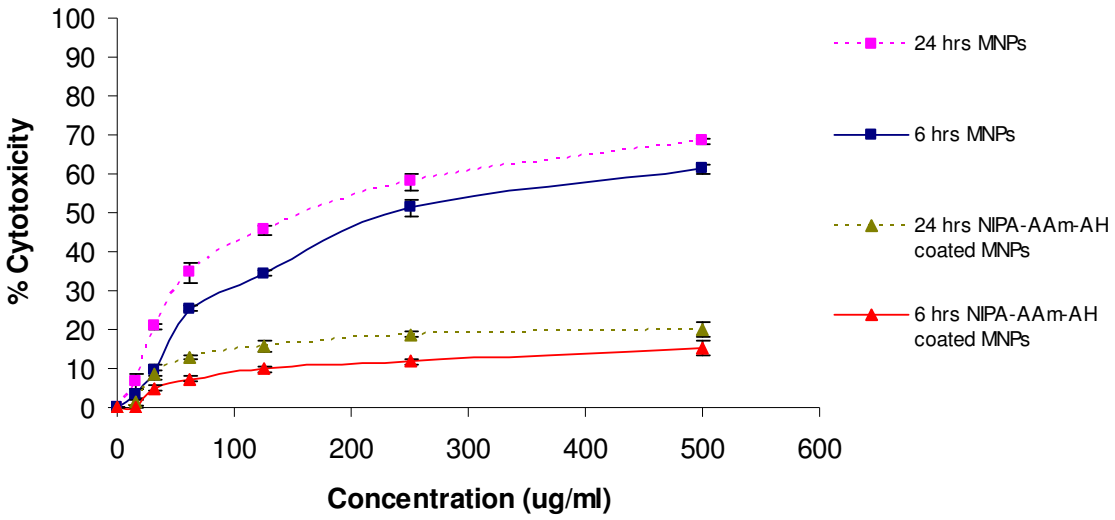

Figure 3.29. Cytotoxicity study of MNPs and NIPA-AAm-AH coated MNPs.

3.2.7 Cellular uptake

In order to determine the optimal concentration of nanoparticles and the optimal incubation time required for an effective treatment, the cellular uptake of NIPA, NIPA-AAm, and NIPA-AAm-AH coated MNPs by the prostate cancer cell line JHU31 (ATCC) was investigated. As shown in Figure 3.30, JHU31 cells took up polymer coated MNPs in a concentration- and incubation time-dependent manner. The highest cellular uptake was observed when the cells were treated with NIPA-AAm and NIPA-AAm-AH coated MNPs. The lowest uptake was observed when cells were treated with NIPA coated MNPs. The low uptake of NIPA coated MNPs might be due to the low LCST of NIPA coated MNPs (32°C), which results in aggregation of the nanoparticles due to hydrophobic attraction and hindrance of their cellular uptake. Laser scattering particle sizer (Nanotrac. measurements) indicated that aggregation of NIPA coated MNPs at 37°C caused an increase in size by eight fold, whereas NIPA-AAm and NIPA-AAm-AH coated MNPs remain in an original size range. The cellular uptake of NIPA coated MNPs formed a plateau at 300 µg/ml, whereas the cellular uptake of NIPA-AAm and NIPA-AAm-AH coated MNPs formed a plateau at 500 µg/ml (Figure 3.30 a). The incubation time studies indicated that uptake of the polymer coated MNPs by prostate cancer cell reached a plateau after four hours (Figure 3.30 b).

(a)

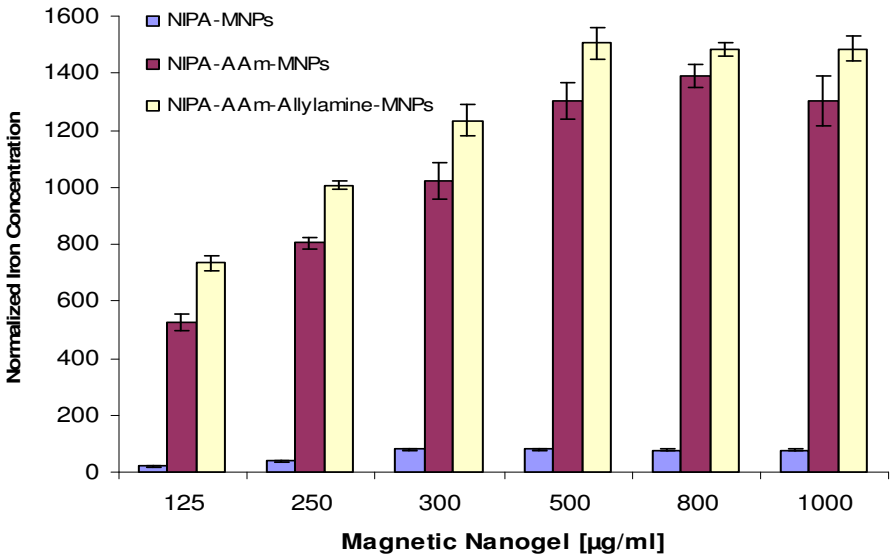

(b)

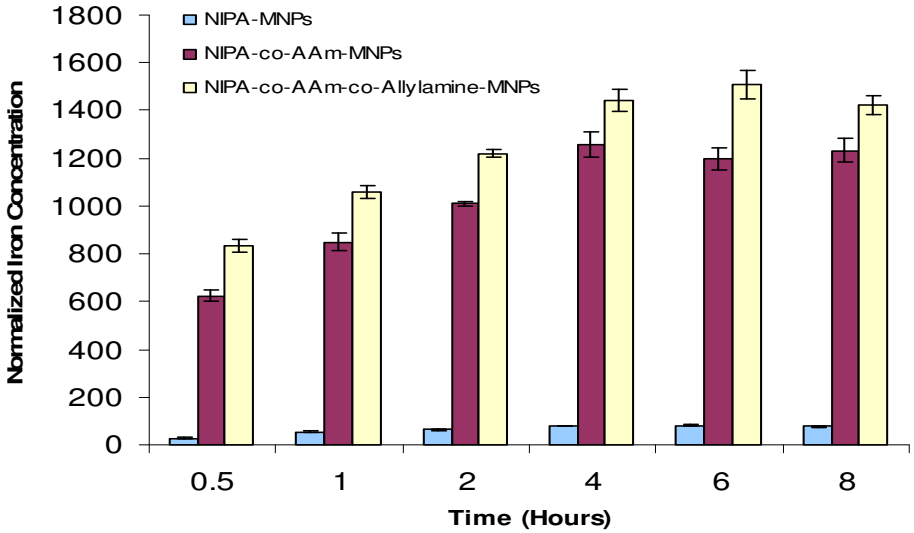

Figure 3.30. Cellular uptake studies. (a) Effect of concentration on cellular uptake. (b) Effect of time on cellular uptake.

In order to image the cellular uptake of NIPA-AAm-AH coated MNPs, Texas Red was conjugated to nanoparticles, and they were incubated with prostate cancer cells for one hour. The results indicated that nanoparticles were internalized by prostate

cancer cells and were accumulated in the cytoplasm (Figure 3.31). As a control sample, Texas Red was incubated with cancer cells, and an insignificant amount of Texas Red detected inside the cells (Figure 3.32). These results indicated that our NIPA-AAm-AH coated MNPs would provide active groups for bioconjugation.

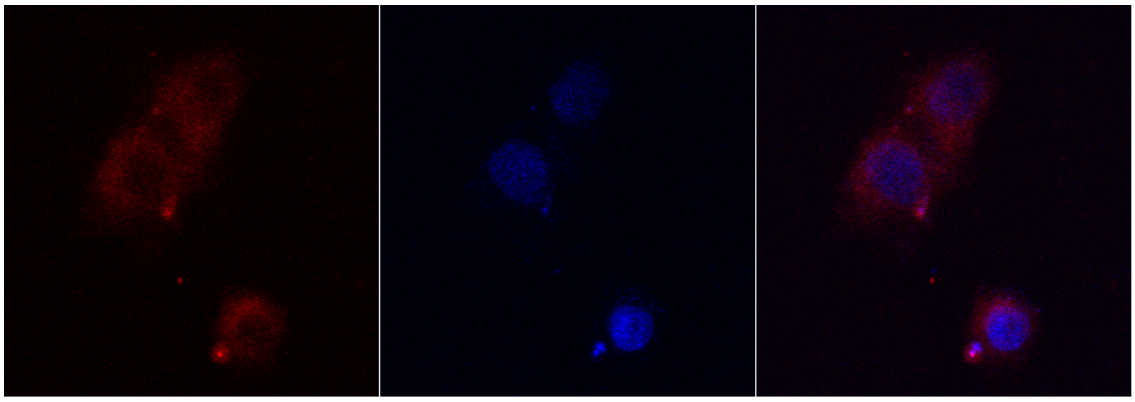

Figure 3.31. Uptake of nanoparticles by JHU31 prostate cancer cell. (a) Detection of Texas Red conjugated nanoparticles, (b) detection of nucleus (DAPI), and (c) superimposed of these two images.

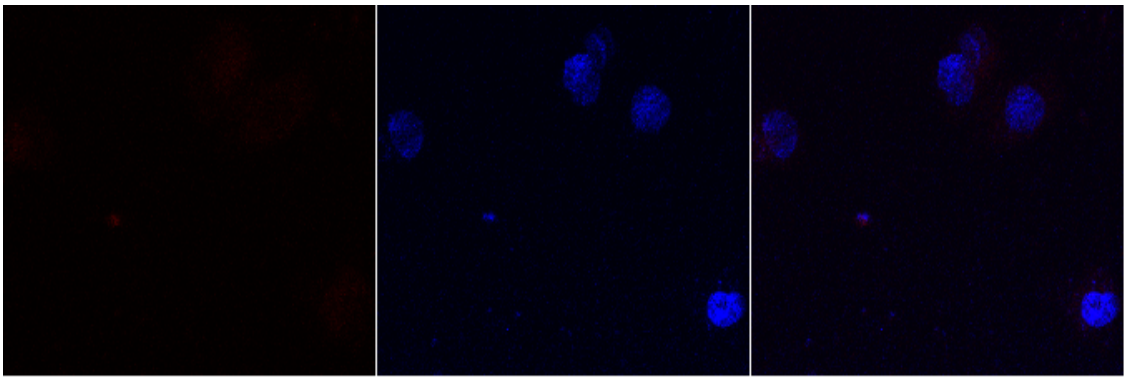

Figure 3.32. Confocal images of uptake of Texas Red (control) by JHU31 prostate cancer cells. (a) Detection of Texas Red, (b) detection of nucleus (DAPI), and (c) superimposed of these two images.

Prussian blue staining was also used to detect cells that contained NIPA-AAm-AH coated MNPs. This assay stains the iron content of the nanoparticles as blue. As shown in Figure 3.33 (a), the blue color detected within the cells indicates the presence of NIPA-AAm-AH coated MNPs inside the cells. Furthermore, the cells were counter stained with pararosaniline in order to image the membrane of the cells (the outer boundary). As shown in Figure 3.33 (b), the blue color is clearly observed inside the cells.

(a)

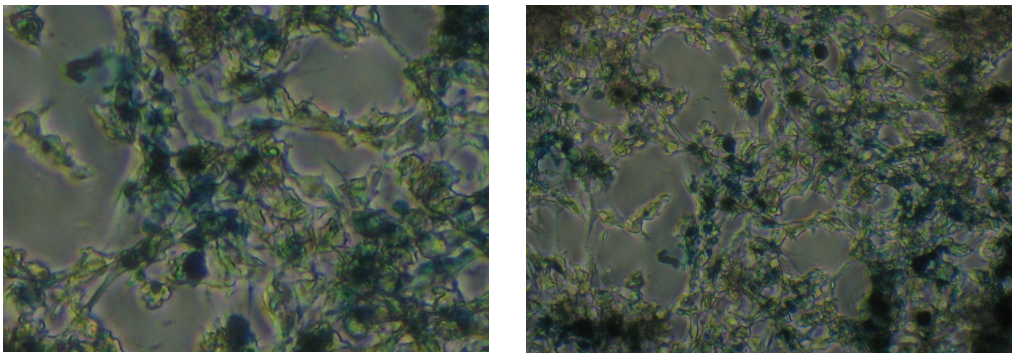

(b)

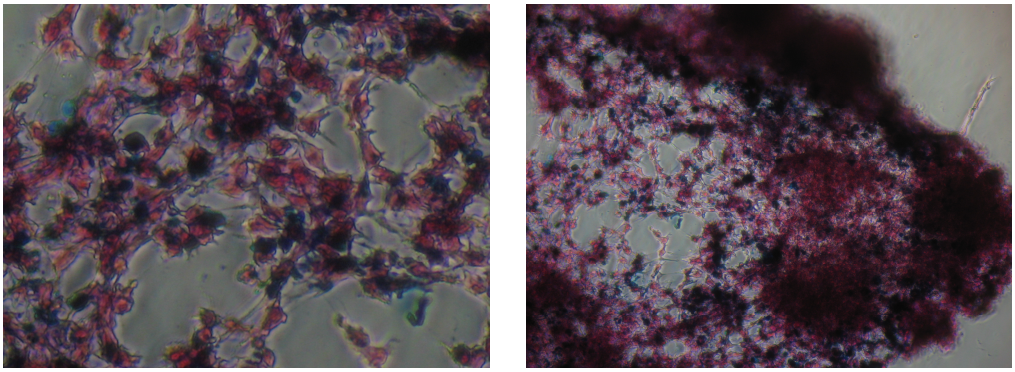

Figure 3.33. Prussian blue staining of the NIPA-AAm-AH coated MNPs. (a) Staining magnetic nanogels inside the prostate cancer cells. (b) Staining cell membrane and magnetic nanogels inside the prostate cancer cells.

3.2.8 Pharmacological activity of DOX loaded NIPA-AAm-AH coated magnetic nanoparticles

In order to investigate the pharmacological activity of the released drugs from NIPA-AAm-AH coated MNPs, the viability of prostate cancer cells exposed to DOX-loaded nanoparticles was assessed. As Figure 3.34a indicates, the free DOX decreased cell viability to 20% in comparison to the control. Moreover, DOX-loaded nanoparticles decreased cell viability to 70% at 37°C. However, when cells were exposed to DOX-loaded nanoparticles at temperature cycle (between 37°C and 41^0C: one hour each at each temperature for 24 hours) and 41°C, the cell viability decreased to 36% and 12%, respectively (Figure 3.34b and c). The decreases in cell viability are much more significant, especially at 41°C in comparison to 37°C, which is an indication that our drug delivery system is temperature sensitive and the released drugs are pharmacologically active.

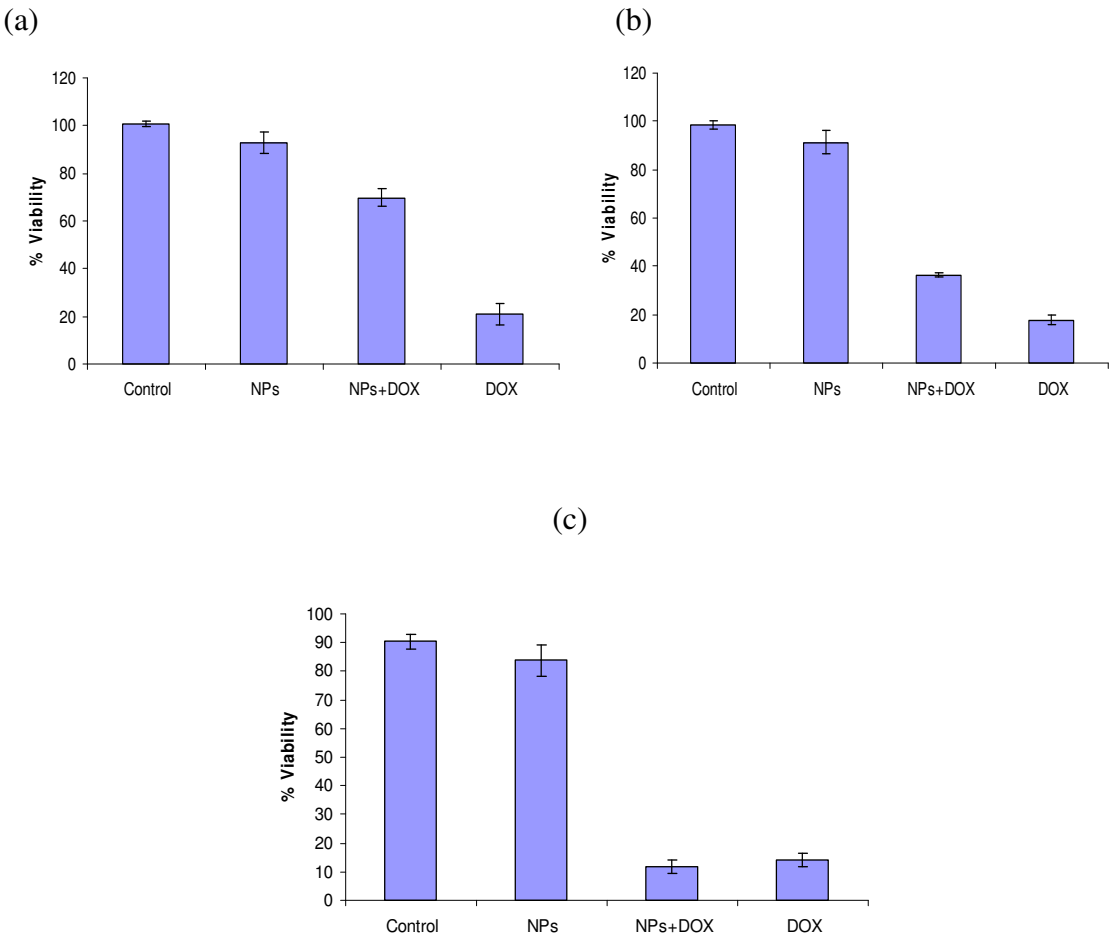

Figure 3.34. Pharmacological activity of DOX loaded NIPA-AAm-AH coated MNPs in comparison with empty nanoparticles and free DOX. The cell viability was investigated using MTS assays at (a) 37^0C, (b) temperature cycles between 37^0C and 41^0C (one hour each temperature for 24 hours) and (c) 41^0C.

3.2.9 In vitro localization of magnetic nanogels

To investigate the retention of NIPA-AAm-AH coated MNPs in the absence or presence of a magnetic field under physiological flow conditions, a parallel flow chamber was used. As shown in Figure 3.35 (a), less than 1% retention was observed when no external magnetic field was applied. Furthermore, the lowest percent retention

was observed when high shear stress (21 dyn/cm^2) was used. The retention of the nanoparticles in the absence of external magnetic field is due to the fact that the nanoparticles are positively charged, and it is possible that they were entrapped in the system due to the electrostatic attraction. However, the result is dramatically different in the presence of a magnetic field. As shown in Figure 3.35 (b), the lowest percent retention was 97.9%. The great difference between the absence (Figure 3.35 a) and the presence of a magnetic field (Figure 3.35 b) proves how effectively the magnetic system might be when used as a targeted drug delivery system, by virtue of their localization in the body at a disease sites using an external magnetic field. Furthermore, in each group the lowest percent retention was observed at the highest fluid shear stress (21 dyn/cm^2). This may be due to the effect of viscous drag on the attraction of nanoparticles to the external magnetic field.

In the presence of a magnetic field, different cell types had slightly different percent retention (Figure 3.35c). Endothelial cells, smooth muscle cells, and prostate cancer cells were chosen to study the percent retention of NIPA-AAm-AH coated MNPs. The overall conclusion from this study is that at the presence of an external magnetic field there is more than 93% retention of nanoparticles within these cell types.

a) Without magnetic field/cells

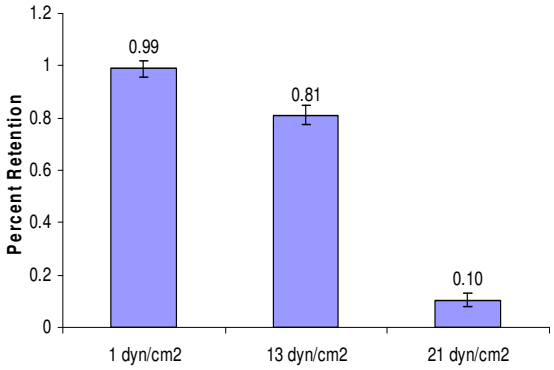

b) With magnetic field and without cells

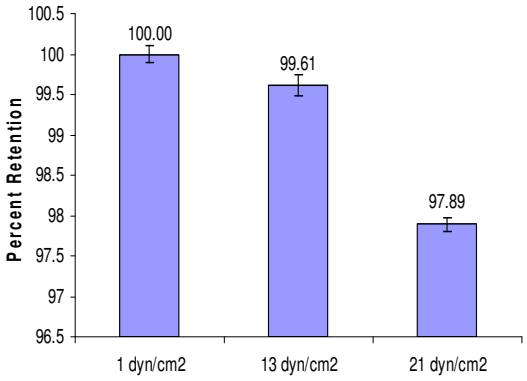

c) Smooth muscle cells (SMCs), Endothelial cells (ECs), and Cancer cells (CCs)

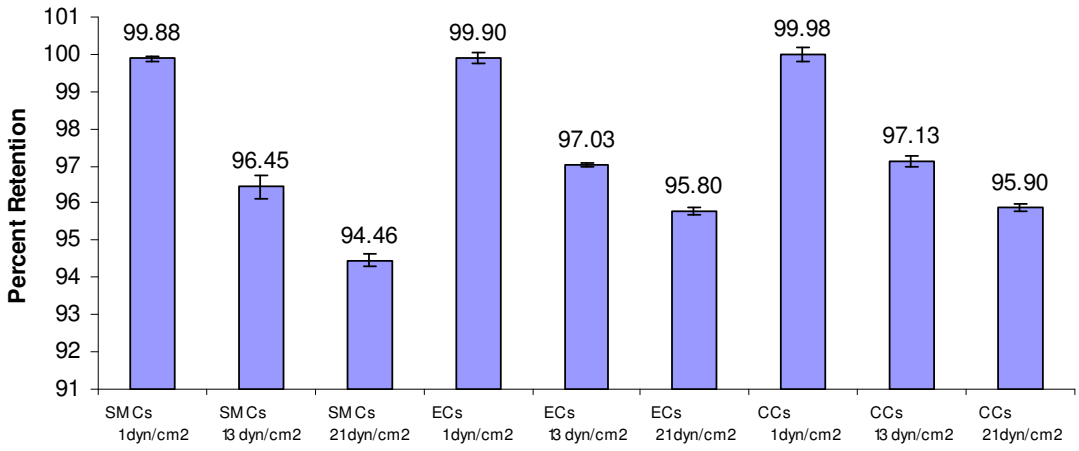

Figure 3.35. Flow studies of the NIPA-AAm-AH coated MNPs at different shear stresses. a) Flow studies at different flow rates without magnetic fields and cells. b) Flow studies at different shear stresses with magnetic fields and without cells. Flow studies at different shear stresses with magnetic fields using c) endothelial cells, smooth muscle cells, and cancer cells.

In order to study the in vitro localization of the NIPA-AAm-AH coated MNPs further, the cellular uptake of nanoparticles by prostate cancer cells seeded on the glass slides was investigated after running the flow system. The results indicated that the

maximum uptake is at zero and 1 dyn/cm^2 (Figure 3.36). The dynamic cellular uptake of nanoparticles was inversely correlated to the levels of shear stress with the most effective uptake occurred at the lowest shear stress.

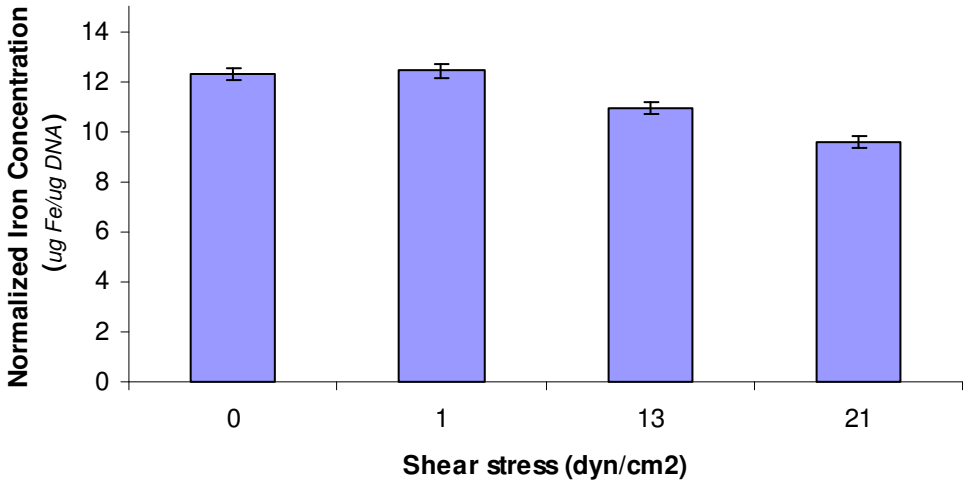

Figure 3.36. Cellular uptake studies of the NIPA-AAm-AH coated MNPs at different shear stresses.

CHPATER 4

DISCUSSIONS

In this research work we have synthesized polymer magnetic drug delivery system for treatment of prostate cancer. In order to characterize the synthesized nanoparticles, several techniques were used. One of the most powerful and widely used chemical characterization techniques is nuclear magnetic resonance (NMR). Due to the magnetic core of the system, it is not possible to fully characterize the nanoparticles using NMR. Therefore, the polymer coat of the system was first fully characterized, and then the optimized polymer coat was applied to magnetic core.

4.1 Nanogels

Temperature sensitive polymer coat was chosen in order to have a controlled drug delivery system. Therefore, NIPA was chosen as polymer coat since it is the most widely studied temperature sensitive polymer in bioengineering applications. However, the LCST of NIPA is below body temperature. Therefore, AAm was copolymerized with NIPA in order to increase the LCST above body temperature. In order to enhance the targeted capability of the drug delivery system, it is necessary to conjugate biomolecules such as antibodies onto the nanoparticle surface. However, due to the resonance in the amide group of the acrylamide, the addition of biomolecules onto the

surface of nanoparticles is prevented. It is possible to chemically modify the amide gourp of AAm, however this would change the LCST of the nanoparticles dramatically. It has been previously shown that AH copolymerization with NIPA does not change the LCST significantly.[128] Consequently, AH was also copolymerized with NIPA-AAm in order to be able to incorporate biomolecules onto the nanoparticle while not altering much the LCST of the materials.

4.1.1 Physical and chemical characterization of nanogels

The average size and size distribution of the synthesized nanoparticles were analyzed using TEM and dynamic light scattering (DLS). The results indicated that the nanoparticles are spherical in shape with uniform size distribution. Furthermore, the DLS results indicated that the nanoparticle size is inversely dependent to the surfactant concentration up to a certain point (below 0.5 M), plateau was formed at a higher concentrations. Results from other groups has also shown this kind of relationships between surfactant concentration and nanoparticles size.[48]

As it was mentioned above, NMR is the most powerful technique to characterize the chemical composition of a compound. This is clearly evident in the FTIR results. By comparing the peaks present in each nanoparticles (NIPA, NIPA-AAm, and NIPA-AAm-AH) spectrum, it is clear that there is no difference between them but only at 3423.6 cm^{-1} which corresponds to the stretching vibration of the primary amine group of AH in the NIPA-AAm-AH. The presence of the primary amine

group was further verified by proton NMR. The primary amine group peak was disappeared after treating the NIPA-AAm-AH with hydrochloric acid. The disappearance of peak is due to the formation of quaternary ammonium salt. Furthermore, carbon NMR and titration was used in order to quantify the experimental result of the formation of the nanogels. The results indicated that the composition of the nanogels approximately followed those compounds in the feed, implying that polymerization of the copolymers was occurring as expected.

The LCST of the synthesized nanogels were investigated via UV-Vis spectrophotometer. The results indicated that the final product, NIPA-AAm-AH, has the sharpest phase transition in comparison to NIPA and NIPA-AAm. The sharp phase transition of the NIPA-AAm-AH is a favorable characteristic, since it would cause the release of drug in response to small changes in temperature.

The conjugation capability of the NIPA-AAm-AH nanogels was investigate by using PEG, IgG, and QDs. The surface of the nanoparticles was conjugated to PEG in order to increase the circulation half life of the nanoparticles. Due to hydrophilic properties of PEG, the circulation time would increase by preventing attachment of platelets and other inflammatory signaling proteins.[6, 7, 9] Furthermore, a model protein, IgG, was used to investigate the bioconjugation. Assessment of protein conjugation is important since antibodies will be further attached onto our nanogels in order to increase their targeting capabilities. In addition, QDs was conjugated to our

nanoparticles for future *in vivo* imaging of the drug delivery system. All of the conjugations were assessed via cytoviva which indicated that coupling agent is necessary for conjugation. Furthermore, NIPA-AAm-AH was capable of bioconjugation whereas NIPA-AAm was not. In addition, the TEM image of QDs conjugation indicated the presence of the QDs on the NIPA-AAm-AH nanogels. However, the QDs conjugation needs further investigation, due to unexplainable color change seen after reaction of QDs with NIPA-AAm-AH nanogels.

4.1.2 *In vitro* studies of nanogels

The cytotoxicity of the NIPA-AAm-AH nanogels was investigated utilizing MTS assays. The result indicated that there is no significant cytotoxicity below 200 µg/ml of nanogel concentration. In addition, minor toxicity was observed at higher concentrations (less than 85%). Atlhough our overall result indicates that our nanoparticles are biocompatible *in vitro*, the biocompatibility investigation *in vivo* is necessary in order to fully assess its compatibility.

The drug release profile of the NIPA-AAm-AH nanogels indicated that our nanogels has a burst drug release profile in response to change in temperature. The burst drug release from our nanogels is a favorable characteristic since drug can be released in controlled and dose specific manner. This type of drug release profile is suitable for aggressive treatment of cancer cells.

4.2 Magnetic nanogels

4.2.1 Physical and chemical characteristics of magnetic nanogels

The size of NIPA and NIPA-AAm-AH coated MNPs were investigated using TEM. The result indicated that both magnetic nanogels were approximately 100 nm in diameter with spherical shape. Furthermore, the TEM result of the NIPA coated MNPs indicated higher number of magnetic nanoparticles in the core in comparison to NIPA-AAm-AH coated MNPs. It is possible that the use of mechanical stirrer instead of magnetic stirrer in synthesis of NIPA-AAm-AH coated MNPs caused less aggregation of MNPs before coating with NIPA-AAm-AH.

In order to characterize the chemical composition of the magnetic nanogels, FTIR and XPS was used. Both results indicated the presence of the functional groups of magnetic core and polymer coat. There was a slight difference in the XPS of NIPA-AAm-AH coated MNPs in comparison to NIPA coated MNPs whereby the Fe peak of magnetic core was not observed. The possible explanation is that the absence of the Fe peak is due to the thick coating of NIPA-AAm-AH. The thick coating prevents the penetration of X-ray into the NIPA-AAm-AH coat to reach the MNPs in the core. The absence of the Fe peak in coated MNPs has also been reported by Cao et al.[119]

The SQUID was used in order to investigate the magnetic properties of the synthesized magnetic nanogels. The results indicated that the saturation magnetization of the magnetic nanogels decrease after each layer of coating. The least saturation

magnetization was observed when the NIPA-AAm-AH was used as polymer coat. This is again might be due to the thicker polymer coat of NIPA-AAm-AH in comparison with NIPA coated MNPs. Similar results has been observed when different polymers such as polystyrene was used to coat MNPs.[129]

4.2.2 In vitro studies of magnetic nanogels

Drug release profile of magnetic nanogels was investigated using DOX as model drug. There was no significant difference observed in release profile of magnetic nanogels and nanogels. It is evident that from both types of nanoparticles there is a burst release of encapsulated drug in response to temperature. This fact is the superior advantage of using temperature sensitive coating for a drug delivery system. By having control over the release of drug, the dose and time of release can be predicted for maximum destruction of cancerous cells. Furthermore, controlled-release modalities reduce side effects, regulate dosing, localize the therapeutic actions, and increase patient compliance.[130] This type of burst release has been reported in NIPA coated MNPs micelles (without covalent bonding).[131] In comparison to our study, NIPA coated MNPs micelles have 30% lower loading efficiency which might be due to a thinner shell surrounding the MNPs.[131] The thicker shell in our nanoparticles not only induced burst release but it also has a prolong release over 70 hours.

The cytotoxicity of the MNPs and NIPA-AAm-AH coated MNPs was compared using LDH assays. The results indicated that the polymer coated MNPs had higher

compatibility in comparison to MNPs. In clinic, MNPs are used at 50 to 200 mg Fe as MRI diagnostic imaging which is much less in comparison to the body's normal iron storage (3000-4000 mg Fe).[2, 83, 98] Furthermore, the normal liver contains approximately 0.2 mg Fe/gram, and the chronic iron toxicity in liver occurs when this concentration exceeds 4mg Fe/mg.[91] In drug delivery applications for prostate cancer treatment concentrations less than 100 μg/ml of MNPs would be used which is according to our results is in a compatible range.[59] It is only when higher concentration of MNPs used for metastasized (late stage) cancer patients that the toxicity of the MNPs would become an issue due to the high dose requirements. However, it is important to realize that a definitive conclusion cannot be drawn until after *in vivo* investigation of these particles in body.

The static cellular uptake of the magnetic nanogels was investigated in respect to dose and incubation time. Results indicated that NIPA-AAm-AAm and NIPA-AAm coated MNPs had significantly higher cellular uptake in comparison to NIPA coated MNPs. The low uptake of NIPA coated MNPs might be due to the low LCST of NIPA coated MNPs (32°C), which results in aggregation of the nanoparticles due to hydrophobic attraction. This hypothesis was confirm via using laser scattering particle sizer which indicated aggregation of NIPA coated MNPs at 37°C, whereas NIPA-AAm and NIPA-AAm-AH coated MNPs remained their original nanosize range. NIPA coated MNPs were in micron size due to the aggregation whereby their uptake was reduced due to larger sizes. Other investigators have already shown that particles larger

than 500 nm are not uptaken by cells whereas nanoparticles within 100-200 nm range are mostly internalized by various cell types.[132] Cellular uptake studies also indicated that the uptake was dose and time dependent (the results are discussed in detail in chapter 3). The cellular uptake of the nanoparticles was confirmed with both iron staining and confocal microscopy, showing that the magnetic nanogels were internalized into the cytoplasm of prostate cancer cells.

The pharmacological activity of the released DOX from our nanoparticles were investigated at 37°C, 41°C and temperature cycle between 37°C and 41°C. The results indicated that the released drug is as effective as free drug in destroying prostate cancer. It has also been reported that DOX-loaded MNPs (PEG coated MNPs) release pharmacological active DOX that has a remarkable activity to kill cancer cells.[133] From the drug release results, it is evident that DOX release from our nanoparticles in response to temperature, and at the LCST of magnetic nanogel maximum DOX activity was observed in comparison to other temperatures.

The magnetic nanogel localization via external magnetic field was investigated utilizing a parallel flow chamber. The results indicated that most of the magnetic nanogels were retained and uptaked by prostate cancer cells in presence of an external magnetic field. However, in the absence of an external magnetic field little was retained and uptaked by prostate cancer. These results imply the effectiveness of the designed system for localized drug delivery applications.

CHAPTER 5

CONCLUSIONS

In this research project, temperature sensitive nanoparticles and temperature sensitive magnetic nanoparticles were successfully synthesized. The size and morphology of the nanoparticles were characterized using dynamic light scattering technology (Nanotrac) and transmission electron microscopy. The amine groups of the nanoparticles were successfully conjugated to various molecules such as PEG, antibodies and QDs as a model for future bioconjugation. These nanoparticles also demonstrated biocompatibility property as shown by the cytotoxicity study using fibroblast cells. Furthermore, the drug release studies indicated a release of encapsulated drugs from these nanoparticles in response to changes in temperature with the highest percentage of release occurring above the LCST. The polymer coated magnetic nanoparticles were further characterized in vitro by investigating their cellular uptake. The results showed that the nanoparticles were uptaken by cancer cells and were mostly accumulated in the cytoplasm. In addition, the MTS assays indicated that the drug released from our nanoparticles was pharmacologically active. Finally, dynamic flow studies indicated that at the presence of an external magnetic field, there was more than 93% increase in retention of nanoparticles under physiological flow conditions. This study demonstrated the potential use of our nanoparticles as a

localized drug delivery system. Furthermore, the dynamic cellular uptake studies of the nanoparticles were also indicated that our nanoparticles were effectively localized and uptaken by cancer cells.

CHAPTER 6

LIMITATIONS AND FUTURE WORK

The major limitation to this design is the aggregation of nanoparticles, especially magnetic nanoparticles. It is very well known that all types of nanoparticles aggregate. Sonication of nanoparticles before administration would positively reduce the aggregation. However, sonication would not fully compensate for the aggregation due to the applied external magnetic field. The preliminary data shows that a decrease in magnetic moment due to polymer encapsulation which also decreases their propensity for aggregation. Therefore, the encapsulation thickness must be balanced against the magnetic properties to get the appropriate product. This study did not investigate this aspect. The polymer shell thickness could be changed by varying various factors such as surfactant concentration and the water/oil ratio. The other limitation of this system is that the nanoparticles are not biodegradable, especially that the outer layer of nanoparticle is not degradable. In the future, the possibility of cross linking the polymer coat using a biodegradable cross linking agent should be investigated. In addition to the physical properties of the nanoparticles, the fate of them *in vitro* and *in vivo* should also be investigated. For instance, it is important to study the effect of core and shell on mitosis and cytotoxicity on various cells (e.g. endothelial, smooth muscle, and prostate cells) via utilizing DNA, NADH, and caspase assays. Furthermore, *in vivo* studies need

to be conducted to investigate the effect of core and shell on initiation of unwanted scaring, inflammation, and metastasis.

REFERENCES

1. Gould, P., Nanomagnetism shows in vivo potential. *Nanotoday* **2006,** 1, 34-39.
2. Bonnemain, B., Superparamagnetic agents in magnetic resonance imaging: physicochemical characteristics and clinical applications. A review. *J Drug Target* **1998,** 6, (3), 167-74.
3. Choi, H.; Choi, S. R.; Zhou, R.; Kung, H. F.; Chen, I. W., Iron oxide nanoparticles as magnetic resonance contrast agent for tumor imaging via folate receptor- targeted delivery. *Academic Radiology* **2004,** 11, (9), 996-1004.
4. Corot, C.; Robert, P.; Idâee, J. M.; Port, M., Recent advances in iron oxide nanocrystal technology for medical imaging. *Advanced drug delivery reviews* **2006,** 58, (14), 1471-504.
5. Dobson, J., Gene therapy progress and prospects: magnetic nanoparticle-based gene delivery. *Gene Ther* **2006,** 13, (4), 283-7.
6. Gupta, A. K.; Wells, S., Surface modified superparamagnetic nanoparticles for drug delivery: preparation, characterization, and cytotoxicity studies. *IEEE Trans Nanobiosci* **2003,** 3, (1), 66-73.
7. Gupta, A. K.; Wells, S., Surface modification superparamagnetic nanoparticles for drug delivery: preparation, characterization, and cytotoxicity studies. *IEEE Trans Nanobiosci* **2004,** 3, (1), 66-73.
8. Ma, M.; Zhang, Y.; Yu, W.; Shen, H.; Zhang, H.; Gu, N., Preparation and characterization of magnetic nanoparticles coated by amino silane. . *Colloids and surface A: Physicochem. Eng. Aspects.* **2003,** 212, 219-226.
9. Gupta, A. K.; Gupta, M., Synthesis and surface engineering of iron oxide nanoparticles for biomedical applicaitons. *Biomaterials* **2005,** 26, (18), 3995-4021.
10. Sugimoto, T.; Matijevic, E., *Journal of Colloid Interface Science* **1980,** 74, 227.
11. Jolivet, J. P., Metal oxide chemistry and synthesis: from solution to solid state. *New York: Wiley* **2000**.
12. Feltin, N.; Pileni, M. P., *Langmuir* **1997,** 13, 3927.
13. Fievet, F.; Lagier, J. P.; Figlarz, M., *Mater. Res. Bull.* **1989,** 29.
14. Feldmann, C.; Jungk, H. O., Polyol-mediated preparation of nanoscale oxide particles. *Angew. Chem. Int. Ed.* **2001,** 40, (2), 359-362.
15. Pedro, T.; Maria, P. M.; Sabino, V. V.; Teresita, G. C.; Carlos, J. S., The preparation of magnetic nanoparticles for applications in biomedicine. *Journal of Physical D.: Appl. Phys.* **2003,** 36, 182-197.
16. Liu, C.; Wu, X.; Klemmer, T. J.; Shukla, N.; Yang, X.; Weller, D.; Roy, A. G.; Tanase, M.; Laughlin, D., *J. Phys. Chem. B* **2004,** 108, 6121.
17. Rockenberger, J.; Scher, E. C.; Alivisatos, A. P., *J. Am. Chem. Soc.* **1999,** 121, 11595.

18. Hyeon, T.; Lee, S. S.; Park, J.; Chung, Y.; Na, H. B., *J. Am. Chem. Soc.* **2001,** 123, 12798.
19. Sun, S.; Zeng, H., Size-controlled synthesis of magnetic nanoparticles. *Journal of American Chemical Society* **2002,** 124, 8204-8205.
20. Allen, M.; Willits, D.; Mosolf, J.; Young, M.; Douglas, T., Protein cage constrained synthesis of ferromagnetic iron oxide nanoparticles. *Adv. Mater.* **2002,** 14, (21), 1562-1565.
21. Chasteen, N. D.; Harrison, P. M., *J. Struct. Biol.* **1999,** 126, 182.
22. Meldrum, F. C.; Heywood, B. R.; Mann, S., *Science* **1992,** 257, 522.
23. Pascal, C.; Pascal, J. L.; Favier, F.; Elidrissi-Moubtassim, M. L.; Payen, C., *Chem. Mater.* **1999,** 11, 141.
24. Messing, G. L.; Zhang, S.; Jayanthi, G. V., *J. Am. Ceram. Soc.* **1993,** 76, 2707.
25. Cauchetier, M.; Croix, O.; Herlin, N.; Luce, M., *J. Am. Ceram. Soc.* **1994,** 77, 93.
26. Veintemillas-Verdaguer, S.; Morales, M. P.; Serna, C. J., *Appl. Organomet. Chem.* **2001,** 15, 1.
27. Himpsel, F. J.; Ortega, J. E.; Mankey, G. J.; Willis, R. F., *Adv. Phys.* **1998,** 47, 511.
28. Tang, Z. X.; Sorensen, C. M.; Klabunde, K. J.; Hadjipanayis, G. C., *Phys. Rev. Lett.* **1991,** 67, 3602.
29. Lamba, S.; Annapoorni, S., Single domain magnetic arrays: role of disorder and ineractions. *The European Physical Journal B* **2004,** 39, 19-25.
30. Iglesias, O.; Laberta, A., *Phys. Rev. B* **2000,** 63, 184416.
31. Kodama, R. H.; Berkowitz, A. E., *Phys. Rev. B* **1999,** 59, 6321.
32. Grodzinski, P.; Silver, M.; Molnar, L. K., Nanotechnology for cancer diagnostics: promises and challenges. *Expert review of molecular diagnostics* **2006,** 6, (3), 307-318.
33. Osaka, T.; Matsunaga, T.; Nakanishi, T.; Arakaki, A.; Niwa, D.; Iida, H., Synthesis of magnetic nanoparticles and their applictions to bioassays. *Analytical and bioanalytical chemistry* **2006,** 384, (3), 593-600.
34. Zee-Cheng, R. K.; Cheng, C. C., Delivery of anticancer drugs. *Methods and findings in experimental and clinical pharmacology.* **1989,** 11, (7-8), 439-529.
35. Berry, C. C.; Wells, S.; Charles, S.; Aitchison, G.; Curtis, A. S., Cell response to dextran-derivatised iron oxide nanoparticles post internalization. *Biomaterials* **2004,** 25, (23), 5405-5413.
36. Berry, C. C.; Wells, S.; Charles, S.; Curtis, A. S., Dextran and albumin derivatized iron oxide nanoparticles: influence on fibroblasts in vitro. *Biomaterials* **2003,** 24, (25), 4551-4557.
37. Jordan, A.; Scholz, R.; Maier-Hauff, K.; Van Landeghem, F. K.; Waldoefner, N.; Teichgraeber, U.; Pinkernelle, J.; Bruhn, H.; Neumann, F.; Thiesen, B.; Von Deimling, A.; Felix, R., The effect of thermotherapy using magnetic nanoparticles on rat malignant glioma. *Journal of neuro-oncology.* **2006,** 78, (1), 7-14.
38. Cengelli, F.; Maysinger, D.; Tschudi-Monnet, F.; Montet, X.; Corot, C.; Petri-Fink, A.; Hofmann, H.; Juillerat-Jeanneret, L., Interaction of functionalized

superparamagnetic iron oxide nanoparticles with brain structures. *The Journal of pharmacology and experimental therapeutics.* **2006,** 318, (1), 108-116.
39. Plank, C.; Scherer, F.; Schillinger, U.; Brgemann, C.; Anton, M., Magnetofection: enhancing and targeting gene delivery with superparamagnetic nanoparticles and magnetic fields. *Journal of Liposome Research* **2003,** 13, (1), 29-32.
40. Duan, H. L.; Shen, Z. Q.; Wang, X. W.; Chao, F. H.; Li, J. W., Preparation of immunomagnetic iron-dextran nanoparticles and application in rapid isolation of E. coli O157:H7 from foods. *World Journal of Gastroenterology* **2005,** 11, (24), 3660-3664.
41. Pich, A.; Bhattacharya, S.; Lu, Y.; Boyko, V.; Adler, H. J., Temperature-sensitive hybrid microgels with magnetic properties. *Langmuir: the ACS Journal of surfaces and Colloids.* **2004,** 20, (24), 10706-10711.
42. Sun, H.; Hong, J.; Meng, F.; Gong, P.; Yu, J.; Xue, Y.; Zhao, S.; Xu, D.; Dong, L.; Yao, S., Novel core-shell structure polyacrylamide-coated magnetic nanoparticles synthesized via photochemical polymerization. *Surface and Coating Technology.* **2006,** 201, 250-254.
43. Kokufuta, E.; Ogawa, K.; Doi, R.; Kikuchi, R.; Farinato, R. S., Geometrical Characteristics of Polyelectrolyte Nanogel Particles and Their Polyelectrolyte Complexes Studied by Dynamic and Static Light Scattering. *The Journal of Physical Chemistry* **2007,** 111, 8634-8640.
44. Hoffman, A. S., Hydrogels for biomedical applications. *Annals of the New York Academy of Sciences.* **2001,** 944, 62-73.
45. Morimoto, N.; Endo, T.; Iwasaki, Y.; Akiyoshi, K., Design of hybrid hydrogels with self-assembled nanogels as cross-linkers: interaction with proteins and chaperone-like activity. *Biomacromolecules.* **2005,** 6, (4), 1829-34.
46. Morimoto, N.; Endo, T.; Ohtomi, M.; Iwasaki, Y.; Akiyoshi, K., Hybrid nanogels with physical and chemical cross-linking structures as nanocarriers. *Macromolecular bioscience.* **2005,** 5, (8), 710-6.
47. Vinogradov, S. V.; Bronich, T. K.; Kabanov, A. V., Nanosized cationic hydrogels for drug delivery: preparation, properties and interactions with cells. *Advanced drug delivery reviews.* **2002,** 54, (1), 135-47.
48. Ramanan, R. M.; Chellamuthu, P.; Tang, L.; Nguyen, K. T., Development of a temperature-sensitive composite hydrogel for drug delivery applications. *Biotechnology Progress* **2006,** 22, (1), 118-125.
49. Singh, B.; Chauhan, G. S.; Sharma, D. K.; Kant, A.; Gupta, I.; Chauhan, N., The release dynamics of model drugs from the psyllium and N-hydroxymethylacrylamide based hydrogels. *International journal of pharmaceutics* **2006,** 325, (1-2), 15-25.
50. Singh, J.; Agrawal, K.; Ray, A. R.; Singhal, J. P.; Singh, H.; Dada, V. K.; Mehta, M. R., Polymeric hydrogels for soft contact lenses. *Journal of biomedical materials research.* **1992,** 26, (9), 1253-7.
51. Miyata, T.; Asami, N.; Uragami, T., A reversibly antigen-responsive hydrogel. *Nature* **1999,** 399, (6738), 766-9.
52. Xiaoling, D.; David, F.; Bokkyoo, J., A study of hydrogel thermal-dynamics using Fourier transform infrared spectrometer. *Polymer* **2006,** 47, 4718-25.

53. Xu, Z. Z.; Wang, C. C.; Yang, W. L.; Deng, Y. H.; Fu, S. K., Encapsulation of nanosized magnetic iron oxide by polyacrylamide via inverse miniemulsion polymerization. *Journal of Magnetism and Magnetic Materials.* **2004,** 277, 136-143.
54. Wakamatsu, H.; Yamamoto, K.; Nakao, A.; Aoyagi, T., Preparation and characterization of temperature responsive magnetite nanoparticles conjugated with N-isopropylacrylamide-based functional copolymer. *Journal of Magnetization and Magnetization Materials.* **2006,** 302, (2), 327-333.
55. Beuermann, S.; Buback, M.; Hesse, P.; Hutchinson, R. A.; Kukučková, S.; Lacík, I., Termination Kinetics of the free-radical polymerization of nonionized methacrylic acid in aqueous solution *Macromolecules* **2008,** In press.
56. Wang, P. C.; Chiu, W. Y.; Lee, C. F.; Young, T. H., Synthesis of iron oxide/poly (methyl methacrylate) composite latex particles: nucleation mechanism and morphology. . *Journal of Polymer Science Part A: Polymer Chemistry* **2004,** 42, 5695-5705.
57. Brigger, I.; Dubernet, C.; Couvreur, P., Nanoparticles in cancer therapy and diagnosis. *Adv Drug Deliv Rev* **2002,** 54, (5), 631-51.
58. Widder, K. J.; Morris, R. M.; Poore, G. A.; Howard, D. P.; Senyei, A. E., Selective targeting of magnetic albumin microspheres containing low-dose doxorubicin: total remission in Yoshida sarcoma-bearing rats. *Eur J Cancer Clin Oncol* **1983,** 19, (1), 135-9.
59. Alexiou, C.; Arnold, W.; Klein, R. J.; Parak, F. G.; Hulin, P.; Bergemann, C.; Erhardt, W.; Wagenpfeil, S.; Lubbe, A. S., Locoregional cancer treatment with magnetic drug targeting. *Cancer Res* **2000,** 60, (23), 6641-8.
60. Goodwin, S.; Peterson, C.; Hob, C.; Bittner, C., Targeting and retention of magnetic targeted carriers (MTCs) enhancing intra-arterial chemotherapy. *J Magn Magn Mater* **1999,** 194, 132-9.
61. Goodwin, S. C.; Bittner, C. A.; Peterson, C. L.; Wong, G., Single-dose toxicity study of hepatic intra-arterial infusion of doxorubicin coupled to a novel magnetically targeted drug carrier. *Toxicol Sci* **2001,** 60, (1), 177-83.
62. Lubbe, A. S.; Bergemann, C.; Brock, J.; McClure, D. G., Physiological aspects in magnetic drug-targeting. *J Magn Magn Mater* **1999,** 194, 149-55.
63. Pulfer, S. K.; Ciccotto, S. L.; Gallo, J. M., Distribution of small magnetic particles in brain tumor-bearing rats. *J Neurooncol* **1999,** 41, (2), 99-105.
64. Pulfer, S. K.; Gallo, J. M., Enhanced brain tumor selectivity of cationic magnetic polysaccharide microspheres. *J Drug Target* **1998,** 6, (3), 215-27.
65. Lubbe, A. S.; Alexiou, C.; Bergemann, C., Clinical applications of magnetic drug targeting. *J Surg Res* **2001,** 95, (2), 200-6.
66. Pankhurst, Q. A.; Connolly, J.; Jones, S. K.; Dobson, J., Applications of magnetic nanoparticles in biomedicine. *J Phys D: Appl Phys* **2003,** 36, R167-81.
67. Hafeli, U. O.; Casillas, S.; Dietz, D. W.; Pauer, G. J.; Rybicki, L. A.; Conzone, S. D.; Day, D. E., Hepatic tumor radioembolization in a rat model using radioactive rhenium (186Re/188Re) glass microspheres. *Int J Radiat Oncol Biol Phys* **1999,** 44, (1), 189-99.

68. Hafeli, U. O.; Pauer, G. J.; Failing, S.; Tapolsky, G., Radiolabeling of magnetic particles with rhenium-188 for cancer therapy. *J Magn Magn Mater* **2001,** 225, 73-8.
69. Hafeli, U. O.; Pauer, G. J.; Roberts, W. K.; Humm, J. L., Magnetically targeted microspheres for intracavitary and intraspinal Y-90 radiotherapy. In *International Conf. on Scientific and Clinical Applications of Magnetic Carriers*, Rastock, Germany, 1996.
70. Hafeli, U. O.; Sweeney, S. M.; Beresford, B. A.; Humm, J. L.; Macklis, R. M., Effective targeting of magnetic radioactive 90Y-microspheres to tumor cells by an externally applied magnetic field. Preliminary in vitro and in vivo results. *Nucl Med Biol* **1995,** 22, (2), 147-55.
71. Grimm, P. D.; Blasko, J. C.; Sylvester, J. E.; Meier, R. M.; William, C., 10-year biochemical (prostate-specific antigen) control of prostate cancer with 125I brachytherapy. *International Journal of Radiation Oncology Biology Physics* **2001,** 51, (1), 31-40.
72. Teloken, C., Management of eractile dysfunction secondary to treatment for localized prostate cancer. *Cancer Control* **2001,** 8, 540-545.
73. Han, B. H.; Demel, K. C.; Wallner, K.; Ellis, W.; Young, L.; Russell, K., Patient reported complications after prostate brachytherapy. *J. Urol.* **2001,** 166, 953-957.
74. Shah, S. A.; Cima, R. R.; Benoit, E.; Breen, E. L.; R., B., Rectal complications after prostate brachytherapy. *Dis. Colon Rectum* **2004,** 47, 1487-1492.
75. Peschel, R. E.; Colberg, J. W., Surgery, brachytherapy, and external-beam radiotherapy for early prostate cancer. *Lancet oncol.* **2003,** 4, 233-241.
76. Plank, C.; Anton, M.; Rudolph, C.; Rosenecker, J.; Krotz, F., Enhancing and targeting nucleic acid delivery by magnetic force. *Expert Opin Biol Ther* **2003,** 3, (5), 745-58.
77. Plank, C.; Schillinger, U.; Scherer, F.; Bergemann, C.; Remy, J. S.; Krotz, F.; Anton, M.; Lausier, J.; Rosenecker, J., The magnetofection method: using magnetic force to enhance gene delivery. *Biol Chem* **2003,** 384, (5), 737-47.
78. Schillinger, U.; Brill, T.; Rudolph, C.; Huth, S.; Gersting, S.; Krotz, F.; Hirschberger, J.; Bergemann, C.; Plank, C., Advances in magnetofection- magnetically guided nucleic acid delivery. *J Magn Magn Mater* **2005,** 293, 501-08.
79. Krotz, F.; de Wit, C.; Sohn, H. Y.; Zahler, S.; Gloe, T.; Pohl, U.; Plank, C., Magnetofection--a highly efficient tool for antisense oligonucleotide delivery in vitro and in vivo. *Mol Ther* **2003,** 7, (5 Pt 1), 700-10.
80. Moore, A.; Basilion, J. P.; Chiocca, E. A.; Weissleder, R., Measuring transferrin receptor gene expression by NMR imaging. *Biochim Biophys Acta* **1998,** 1402, (3), 239-49.
81. Sonvico, F.; Dubernet, C.; Colombo, P.; Couvreur, P., Metallic colloid nanotechnology, applications in diagnosis and therapeutics. *Curr Pharm Des* **2005,** 11, (16), 2095-105.
82. Varallyay, P.; Nesbit, G.; Muldoon, L. L.; Nixon, R. R.; Delashaw, J.; Cohen, J. I.; Petrillo, A.; Rink, D.; Neuwelt, E. A., Comparison of two superparamagnetic viral-sized iron oxide particles ferumoxides and ferumoxtran-10 with a gadolinium chelate in imaging intracranial tumors. *AJNR Am J Neuroradiol* **2002,** 23, (4), 510-9.

83. Artemov, D.; Mori, N.; Okollie, B.; Bhujwalla, Z. M., MR molecular imaging of the Her-2/neu receptor in breast cancer cells using targeted iron oxide nanoparticles. *Magn Reson Med* **2003,** 49, (3), 403-8.
84. Remsen, L. G.; McCormick, C. I.; Roman-Goldstein, S.; Nilaver, G.; Weissleder, R.; Bogdanov, A.; Hellstrom, I.; Kroll, R. A.; Neuwelt, E. A., MR of carcinoma-specific monoclonal antibody conjugated to monocrystalline iron oxide nanoparticles: the potential for noninvasive diagnosis. *AJNR Am J Neuroradiol* **1996,** 17, (3), 411-8.
85. Chouly, C.; Pouliquen, D.; Lucet, I.; Jeune, J. J.; Jallet, P., Development of superparamagnetic nanoparticles for MRI: effect of particle size, charge and surface nature on biodistribution. *J Microencapsul* **1996,** 13, (3), 245-55.
86. van Vlerken, L. E.; Amiji, M. M., Multi-functional polymeric nanoparticles for tumour-targeted drug delivery. *Expert Opin Drug Deliv* **2006,** 3, (2), 205-16.
87. Neuberger, T.; Schopf, B.; Hofmann, H.; Hofmann, M.; von Rechenberg, B., Superparamagnetic nanoparticles for biomedical applications: Possibilities and limitations of a new drug delivery system. *J Magn Magn Mater* **2005,** 293, 483-496.
88. Seneterre, E.; Weissleder, R.; Jaramillo, D.; Reimer, P.; Lee, A. S.; Brady, T. J.; Wittenberg, J., Bone marrow: ultrasmall superparamagnetic iron oxide for MR imaging. *Radiology* **1991,** 179, (2), 529-33.
89. Hahn, P. F.; Stark, D. D.; Lewis, J. M.; Saini, S.; Elizondo, G.; Weissleder, R.; Fretz, C. J.; Ferrucci, J. T., First clinical trial of a new superparamagnetic iron oxide for use as an oral gastrointestinal contrast agent in MR imaging. *Radiology* **1990,** 175, (3), 695-700.
90. Rubin, D. L.; Muller, H. H.; Young, S. W.; Hunke, W. A.; Gorman, W. G., Optimization of an oral magnetic particle formulation as a gastrointestinal contrast agent for magnetic resonance imaging. *Invest Radiol* **1994,** 29, (1), 81-6.
91. Chachuat, A.; Bonnemain, B., European clinical experience with Endorem. A new contrast agent for liver MRI in 1000 patients. *Radiologe* **1995,** 35, (11 Suppl 2), S274-6.
92. Kubaska, S.; Sahani, D. V.; Saini, S.; Hahn, P. F.; Halpern, E., Dual contrast enhanced magnetic resonance imaging of the liver with superparamagnetic iron oxide followed by gadolinium for lesion detection and characterization. *Clin Radiol* **2001,** 56, (5), 410-5.
93. Weissleder, R.; Elizondo, G.; Stark, D. D.; Hahn, P. F.; Marfil, J.; Gonzalez, J. F.; Saini, S.; Todd, L. E.; Ferrucci, J. T., The diagnosis of splenic lymphoma by MR imaging: value of superparamagnetic iron oxide. *AJR Am J Roentgenol* **1989,** 152, (1), 175-80.
94. Turetschek, K.; Hubner, S.; Floyd, E.; Helbich, T.; Roberts, T.; Shames, D., MR imaging characterisation of microvessels in experimental breast tumors by using a particulate contrast agent with histopathologic correlation. *Radiology* **2001,** 218, 562-69.
95. Rozenman, Y.; Zou, X. M.; Kantor, H. L., Cardiovascular MR imaging with iron oxide particles: utility of a superparamagnetic contrast agent and the role of diffusion in signal loss. *Radiology* **1990,** 175, (3), 655-9.

96. Greiner, N.; Basseau, F.; Ries, M.; Tyndal, B.; Jones, R.; Moonen, C., Functional MRI of the kidney. *Adbdom Imaging* **2003,** 28, 164-75.
97. Weissleder, R.; Bogdanov, A.; Neuwelt, E. A.; Papisov, M., Long-circulating iron oxides for MR imaging. *Adv Drug Deliv Rev* **1995,** 16, 321-34.
98. Anzai, Y.; McLachlan, S.; Morris, M.; Saxton, R.; Lufkin, R. B., Dextran-coated superparamagnetic iron oxide, an MR contrast agent for assessing lymph nodes in the head and neck. *AJNR Am J Neuroradiol* **1994,** 15, (1), 87-94.
99. Lind, K.; Kresse, M.; Debus, N. P.; Muller, R. H., A novel formulation for superparamagnetic iron oxide (SPIO) particles enhancing MR lymphography: comparison of physicochemical properties and the in vivo behaviour. *J Drug Target* **2002,** 10, (3), 221-30.
100. Enochs, W. S.; Harsh, G.; Hochberg, F.; Weissleder, R., Improved delineation of human brain tumors on MR images using a long-circulating, superparamagnetic iron oxide agent. *J Magn Reson Imaging* **1999,** 9, (2), 228-32.
101. Bogdanov, A., Jr.; Weissleder, R., The development of in vivo imaging systems to study gene expression. *Trends Biotechnol* **1998,** 16, (1), 5-10.
102. Malich, G.; Markovic, B.; Winder, C., The sensitivity and specificity of the MTS tetrazolium assay for detecting the in vitro cytotoxicity of 20 chemicals using human cell lines. *Toxicology* **1997,** 124, 179.
103. Hussain, S. M.; Hess, K. L.; Gearhart, J. M.; Geiss, K. T.; Schlager, J. J., In vitro toxicity of nanoparticles in BRL 3A rat liver cells. *Toxicology in Vitro* **2005,** 19, (7), 975-983.
104. Carter, B. S.; Beaty, T. H.; Steinberg, G. D.; Childs, B.; Walsh, P. C., Mendelian Inheritance of Familial Prostate Cancer. *Proceedings of the National Academy of Sciences* **1992,** 89, 3367-3371.
105. Whittemore, A. S.; Kolonel, L. N.; Wu, A. H.; John, E. M.; Gallagher, R. P.; Howe, G. R.; Burch, J. D.; Hankin, J.; Dreon, D. M.; West, D. W.; Teh, C.-Z.; Ralph S. Paffenbarger, J., Prostate cancer in relation to diet, physical activity, and body size in blacks, whites, and Asians in the United States and Canada. *Journal of the National Cancer Institute* **1995** 87, (9), 652-661.
106. Wu, A. H.; Henderson, B. E., Alcohol and tobacco use: risk factors for colorectal adenoma and carcinoma? *Journal of the National Cancer Institute* **1995,** 87, 239-240.
107. Yallapu, M. M.; Vasir, J. K.; Jain, T. K.; Vijayaraghavalu, S.; Labhasetwar, V., Synthesis, characterization and antiproliferative activity of rapamycin-loaded poly(N-isopropylacrylamide)-based nanogels in vascular smooth muscle cells. *Journal of Biomedical Nanotechnology* **2008,** 4, 16.
108. Gupta, A. K.; Gupta, M., Cytotoxicity suppression and cellular uptake enhancement of surface modified magnetic nanoparticles. *Biomaterials* **2005,** 26, (13), 1565-1573.
109. Nguyen, K. T.; Eskin, S. G.; Patterson, C.; Runge, M. S.; McIntire, L. V., Shear stress reduces protease activated receptor-1 expression in human endothelial cells. *Annals of biomedical engineering* **2001,** 29, (2), 145-52.

110. Wu, J.-Y.; Liu, S.-Q.; Heng, P. W.-S.; Yanga, Y.-Y., Evaluating proteins release from, and their interactions with, thermosensitive poly (N-isopropylacrylamide) hydrogels. *Journal of Controlled Release* **2005,** 102, 361-372.
111. Cheng, Y. H.; Tay, B. K.; Lau, S. P.; Qiao, X. L.; Chen, J. G.; Sun, Z. H.; Xie, C. S., Micromechanical properties of carbon nitride films deposited by radio-frequency-assisted filtered cathodic vacuum arc. *Applied Physics A* **2002,** 75, 375-380.
112. Normand, F. L.; Hommet, J.; Szorenyi, T.; Fuchs, C.; Fogarassy, E., XPS study of pulsed laser deposited CN_x films. *Physical Reviw B* **2001,** 64, (23), 2354161-15.
113. Jernigan, G. G.; Stahlbush, R. E.; Saks, N. S., Effect of oxidation and reoxidation on the oxide-substrate interface of 4H- and 6H-SiC. *Applied Physics Letters* **2000,** 77, (10), 1437-1439.
114. Rjeb, M.; Labzour, A.; Rjeb, A.; Sayouri, S.; Idrissi, M. C. E.; Massey, S.; Adnot, A.; Roy, D., Contribution to the study by X-ray photoelectron spectroscopy of the natural aging of the polypropylene. *M.J. Condensed matter* **2004,** 5, (2), 168-172.
115. Beguin, F.; Rashkov, I.; Manolova, N.; Benoit, R.; Erre, R.; Delpeux, S., Fullerene core star-like polymers-1. Preparation from fullerenes and monoazidopolyehers. *Eur. Polym. J.* **1998,** 34, 905-915.
116. Bureau, C.; Valin, F.; Lecayon, G.; Charlier, J.; Detalle, V., Study of ultrathin polyamide-6,6 films on clean copper and platinum. *Journal Vac. Sci. Technol. A* **1997,** 15, 353-364.
117. Mink, G.; Varsanyi, G.; Bertoti, I.; Grabis, J.; Vaivads, J.; Millers, T.; Szekely, T., XPS Characterization of Ultrafine Si3N4 Powders. *Surface and Interface Analysis* **1988,** 12, 527-530.
118. Rahimi, M.; Yousef, M.; Cheng, Y.; Meletis, E. I.; Eberhart, R. C.; Nguyen, K., Formulation and Characterization of Covalently Coated Magnetic Nanogel. . *Journal of Nanoscience and Nanotechnology* **in press**.
119. Cao, J.; Wang, Y.; Yua, J.; Xiaa, J.; Zhanga, C.; Yina, D.; Häfeli, U. O. U. O., Preparation and radiolabeling of surface-modified magnetic nanoparticles with rhenium-188 for magnetic targeted radiotherapy. *Journal of Magnetism and Magnetic Materials* **2004,** 277, (1-2), 165-174.
120. Grimal, J. M.; Marcus, P., The anodic dissolution and passivation of Ni-Cr-Fe alloys studied by ESCA. *Corrosion Science* **1992,** 33, 805-814.
121. Martin, J. M.; Vovelle, L.; Bou, M.; Mogne, T. L., Chemistry of the interface between aluminium and polyethyleneterephtalate by XPS. *Applied Surface Science* **1991,** 47, 149-161.
122. Finster, J., SiO2 in 6:3 (stishovite) and 4:2 Co-ordination - Characterization by core level spectroscopy (XPS/XAES). *Surf. Interface Anal.* **1988,** 12, 309-314.
123. Bao, H.; Chen, Z.; Lin, K.; Wu, P.; Liu, J., Preparation of magnetic nanoparticles modified by amphiphilic copolymers. *Materials Letters* **2006,** 60, 2167-2170.
124. Batis-Landoulsi, H.; Vergnon, P., *J. Materials Sci.* **1983,** 18, 3399-3403.
125. Coey, J. M. D., *Physical Review Letters* **1971,** 27, (1140-1147).

126. Ramirez, L. P.; Landfester, K., Magnetic polystyrene nanoparticles with a high magnetite content obtained by miniemulsion processes. . *Macromolecular Chemistry and Physics* **2003,** 204, (1), 22-31.
127. Kim, D. K.; Zhang, Y.; Voit, W.; Rao, K. V.; Muhammed, M., *J Magnetism and Magnetic Materials* **2001,** 225, 30-36.
128. Hu, Z.; Huang, G., A new route to crystalline hydrogels, guided by a phase diagram. *Angewandte Chemie (International ed. in English)* **2003,** 42, (39), 4799-802.
129. Ramírez, L. P.; Landfester, K., Magnetic Polystyrene Nanoparticles with a High Magnetite Content Obtained by Miniemulsion Processes. *Macromolecular Chemistry and Physics* **2003,** 204, (1), 22-31.
130. Ferrari, M., Cancer nanotechnology: opportunities and challenges. *Nature Reviews* **2005,** 5, (161-171).
131. Liua, S. Q.; Tongb, Y. W.; Yang, Y.-Y., Incorporation and in vitro release of doxorubicin in thermally sensitive micelles made from poly(N-isopropylacrylamide-co-N,N-dimethylacrylamide)-b-poly(d,l-lactide-co-glycolide) with varying compositions *Biomaterials* **2005,** 26, (24), 5064-5074.
132. Win, K. Y.; Feng, S.-S., Effects of particle size and surface coating on cellular uptake of polymeric nanoparticles for oral delivery of anticancer drugs. *Biomaterials* **2004,** 26, (15), 2713-2722.
133. Park, S. I.; Lim, J. H.; Hwang, Y. H.; Kim, K. H.; Kim, S. M.; Kim, J. H.; Kim, C. G.; Kim, C. O., In vivo and in vitro antitumor activity of doxorubicin-loaded magnetic fluids. *Phys. Stat. Sol.* **2007,** 4, (12), 4345-4351.

BIOGRAPHICAL INFORMATION

Maham Rahimi was born in Tehran, Iran on September 1981, and moved to the United States on December of 1998 to pursue his dream of becoming a medical doctor. He found it fascinating and exciting how different disciplines in science could be brought together to find a better answers to problems in medicine. Eventually, this interest led him to pursue of becoming medical scientist. He completed his Bachelor of Science Degree in Biochemistry and Master of Science Degree in Medicinal Chemistry at Southern Methodist University on August 2004. His research in Medicinal Chemistry gave him a better understanding of the current inadequacy in drug delivery in medicine. With that understanding, he started his research in Drug Delivery and Tissue Engineering Laboratories at University of Texas at Arlington. He plans to complete his Doctor of Philosophy in Biomedical Engineering at joint program of University of Texas at Arlington/University of Texas Southwestern Medical Center on August 2008. He will start his medical school after August of 2008 in order to pursue his interested in oncology.